5-24-2012

Micro-imaging of the Mouse Lung via MRI

Wei Wang
Washington University in St. Louis

WASHINGTON UNIVERSITY IN ST. LOUIS

Department of Physics

Dissertation Examination Committee:
Jason Woods, Chair
Joseph Ackerman
Mark Conradi
David Gierada
Kenneth Kelton
Dmitriy Yablonskiy

Micro-imaging of the Mouse Lung via MRI

by

Wei Wang

A dissertation presented to the
Graduate School of Arts and Sciences
of Washington University in
partial fulfillment of the
requirements for the degree
of Doctor of Philosophy

May 2012

Saint Louis, Missouri

Abstract

Quantitative measurement of lung microstructure is of great significance in assessment of pulmonary disease, particularly in the earliest stages. Conventional stereological assessment of *ex-vivo* fixed tissue specimens under the microscope has a long and successful tradition and is regarded as a gold standard, but the invasive nature limits its applications and the practicality of use in longitudinal studies. The technique for diffusion MRI-based ^{3}He lung morphometry was previously developed and validated for human lungs, and was recently extended to *ex-vivo* mouse lungs. The technique yields accurate, quantitative information about the microstructure and geometry of acinar airways.

In this dissertation, the ^{3}He lung morphometry technique is for the first time successfully implemented for *in-vivo* studies of mice. It can generate spatially-resolved maps of parameters that reveal the microstructure of mouse lung. Results in healthy mice indicate excellent agreement between *in-vivo* morphometry via ^{3}He MRI and microscopic morphometry after sacrifice. The implementation and validation of ^{3}He morphometry in healthy mice open up new avenues for application of the technique as a precise, noninvasive, *in-vivo* biomarker of changes in lung microstructure, within various mouse models of lung disease.

We have applied ^{3}He morphometry to the Sendai mouse model of lung disease. Specifically, the Sendai-virus model of chronic obstructive lung disease has demonstrated an innate immune response in mouse airways that exhibits similarities to the chronic airway inflammation in human COPD and asthma, but the effect on distal lung

parenchyma had not been investigated. We imaged the time course and regional distribution of mouse lung microstructural changes *in vivo* after Sendai virus (SeV) infection with ^{1}H and ^{3}He diffusion MRI. ^{1}H MR images detected the SeV-induced pulmonary inflammation *in vivo* and ^{3}He lung morphometry showed modest increase in alveolar duct radius distal to airway inflammation, particularly in the lung periphery, indicating airspace enlargement after virus infection.

Another important application of the imaging technique is the study of lung regeneration in a pneumonectomy (PNX) model. Partial resection of the lung by unilateral PNX is a robust model of compensatory lung growth. It is typically studied by postmortem morphometry in which longitudinal assessment in the same animal cannot be achieved. Here we successfully assess the microstructural changes and quantify the compensatory lung growth *in vivo* in the PNX mouse model via ^{1}H and hyperpolarized ^{3}He diffusion MRI. Our results show complete restoration in lung volume and total alveolar number with enlargement of alveolar size, which is consistent with prior histological studies conducted in different animals at various time points.

This dissertation demonstrates that ^{3}He lung morphometry has good sensitivity in quantifying small microstructural changes in the mouse lung and can be applied to a variety of mouse pulmonary models. Particularly, it has great potential to become a valuable tool in understanding the time course and the mechanism of lung growth in individual animals and may provide insight into post-natal lung growth and lung regeneration.

Acknowledgements

First and foremost I offer my sincere gratitude to my advisor, Dr. Jason Woods. I attribute this thesis to his enormous encouragement and support. He taught me in various aspects -- physics, medical imaging, language, and more. I appreciate all his contributions of time, ideas, and funding to make my Ph.D. experience productive and stimulating. I'm also deeply thankful for his flexibility and openness to allow me to explore the outside by myself which broadened my horizon and prepared me for future challenges.

I am very much grateful to Dr. Mark Conradi for leading me into the world of MR. He is a born great teacher and I am fortunate to have many opportunities to hear him explain different things very clearly and vividly with his splendid language. I learned a lot from him about NMR physics and hardware. He is always available for help and suggestions. I would like to thank everything he has done for me.

Special thanks to Dr. Nguyet Nguyen: it is a great pleasure to work with her and her expertise in pulmonology was essential for the success of our study. I am always impressed by her capable hands in animal handling of this project.

I am appreciative of Dr. Ken Kelton for his guidance and inspiration as my academic advisor for the first two years in WashU. I will never forget his kind assistance in helping me find the lab that fits my interest.

Dozens of people have helped and taught me immensely at the BMRL. Special thanks to Dr. Joe Ackerman for his support of the project and especially the wise advice he gave me for future direction. I would like to thank Dr. Dmitriy Yablonskiy and Dr. Alex

Sukstanskii. This work would not have been possible without their great theoretical work and unique perspective in the field. I give my heartfelt thanks to Dr. Joel Garbow, Dr. Jim Quirk, Dr. Emir Osmanagic, Dr. Adil Bashir, Bill Spees, and Dr. Larry Bretthorst, who all provided me generous help and advice during the development of the technique.

Thanks you to Dr. David Gierada, for serving as a committee member in my three-person committee and always giving me valuable advice during the past years. I thank Dr. Richard Pierce for helpful discussion and Carla Hall for the help with experiments.

I would like to thank my fellow students and researchers in the lab: Dr. Michelle Milne, Adam Hajari, Dr. David Shane, Jinbang Guo, Dr. Tim Ivancic, Dr. Lasitha Senadheera, Dr. Yulin Chang, Robby Thomen, and Sam Sullivan for their kindness, friendship and help. The initial mouse work done by Dr. Joe Dugas is greatly appreciated, which set a good starting point for me.

Finally, and most importantly, I would like extend my great gratitude to my parents. They born me and raised me in a traditional way with unwavering love and encouragement. They are always the motivation for me to go on. To them I dedicate this thesis.

Table of Contents

List of Tables

List of Figures

Chapter 1
Introduction

1.1 Objective

^{3}He lung morphometry is the quantitative measurement of lung microstructure using ^{3}He diffusion MRI. The objective of this project is to implement ^{3}He lung morphometry to quantify lung microstructure in mouse *in vivo* and apply the technique to a variety of mouse pulmonary models. With the accomplishment of this project, the ^{3}He morphometry should become a precise, noninvasive, *in-vivo* biomarker of changes in lung microstructure and applicable to a wide range of mouse models for longitudinal studies.

Specifically, the objectives are:

1) To develop hardware suitable for mouse imaging on Varian 4.7 T scanner. This includes the hardware for ventilation of the animal and imaging hardware.
2) To develop hyperpolarized ^{3}He imaging protocols for 3He morphometry and ^{1}H imaging protocol for inflammation detection in mouse lung disease models.
3) To develop MATLAB programs for imaging analysis which can automatically or semi-automatically process the raw image data and interpret the Bayesian analysis (see Section 5.4) results.
4) To implement ^{3}He lung morphometry in healthy mice *in vivo* and validate against histology.
5) To apply ^{3}He lung morphometry on various mouse models of COPD.

6) To study the effect of Sendai virus infection on distal lung parenchyma by ^{1}H MRI and ^{3}He morphometry.
7) To characterize the longitudinal, compensatory lung growth in a pneumonectomy mouse model by ^{3}He morphometry and ^{1}H MRI.

1.2 Overview of Pulmonary Imaging

In the past 30 years, pulmonary imaging has been through a remarkable period of development. Multiple imaging modalities applicable to the lung have opened the door to noninvasively assess lung morphometry and function.

Compared to the current clinical standards (e.g. spirometry and body plethesmography, both of which quantify the lung functions by measuring the volume and flow of air that can be inhaled and exhaled), lung imaging has shown great promise in providing insight into the lung structure, function and the relationship between them. There are several imaging modalities which excel in different aspects of pulmonary research and clinical applications: x-ray computed tomography (CT) has advantages with high resolution in visualizing and displaying lung structure *in vivo* in 3D; magnetic resonance imaging (MRI), without radiation risks, can provide quantitative functional information based on the multiple mechanisms responsible for the behavior of the MRI signals; positron emission tomography (PET) and single photo emission tomography (SPECT) can generate the anatomical distribution of radiolabeled compounds which can reflects the presence of various biological processes; optical imaging and echocardiography are also used in some cases to provide useful information of lung. The work presented in this dissertation is mainly related to MRI and CT which will be discussed in details below.

1.2.1 Pulmonary Imaging with Computed Tomography

X-ray CT image is a densitometric map which uses the attenuation of x-ray as the signal to generate images. A series of projection of X-ray images are acquired to create a CT image by computer algorithms. The intensity of each pixel in the image can be mapped to the density of the volume element in the imaging object. The scale used for the imaging intensity is referred as CT numbers or Hounsfield units (HU), which is a linear transformation of the attenuation coefficient or the density. Hounsfield units are defined as 0 for water and -1000 HU for air. Since lung is a mixture of tissue and air, the average CT number of lung is ~ -700 HU for humans, including vessels and airways (14).

Emphysema is defined as "a condition of the lung characterized by abnormal permanent enlargement of the airspaces distal to the terminal bronchioles, accompanied by destruction of their walls, and without obvious fibrosis" (99). CT has been widely used to quantify emphysema by comparing the frequency distribution of the CT numbers to the extent of emphysema seen on gross pathology (28, 40). In CT scans emphysema is characterized by the areas of abnormally low attenuation which corresponds to the airspace enlargement and tissue destruction. There are two main approaches developed to assess emphysema via CT. One is called Density Mask Analysis: a density mask which is a threshold cut-off of x-ray attenuation values has been applied to quantify the extent of emphysema (76). The other approach is the percentile technique in which a histogram of the frequency distribution of pixel density values of lung region is generated and the areas that have densities within a preselected range may be defined as emphysematous (31, 67).

Although CT imaging has become an essential part in lung research and is often used in clinics, the radiation exposure still remains the main limitation of the development of this imaging modality, especially in longitudinal or pediatric studies. The radiation dose needs to be carefully considered for any imaging with CT, due to increased lifetime cancer risk (98). Other disadvantages includes: 1) although the spatial resolution of CT is high but it still cannot resolve the structure information at the alveolar level. 2) It is challenging to obtain functional information directly from CT despite that some functional information can be inferred from certain measurements on CT images.

1.2.2 Pulmonary Magnetic Resonance Imaging

Nearly all body MRI is performed at the ^{1}H frequency because of the high water content in biological tissue. However, in the context of proton MRI, the lung is a particularly challenging organ to image. The water content in the lung is low; 85%-90% of the volume of an inflated lung is air; the remaining 10 – 15% is tissue and blood (116). In addition, large susceptibility effects from air-tissue interfaces cause field inhomogeneities, resulting in a very short T_2^* relaxation time. This contributed significantly to the initial slow development of MRI sequences on lung compared to that on other parts of the body until the introduction of hyperpolarized (HP) gas MRI.

1.2.2.1 Hyperpolarized Gas MRI

The use of hyperpolarized noble gas isotopes ^{3}He and ^{129}Xe has brought a remarkable development of lung MRI from the early 1990s (2). Both ^{3}He and ^{129}Xe are spin one-half noble-gas nuclei and were also suitable for hyperpolarization and gas MRI because of their long T_1 relaxation time and intrinsic atomic properties (49, 78).

The intrinsic low sensitivity of MRI comes from the low thermal polarization formed in a typical external magnetic field (1-5 Tesla) (see Section 3.1.1). In conventional ^{1}H MRI, the low thermal polarization is counterbalanced by the high tissue density to achieve reasonable MR signal in most parts of the body except for the lung. Hyperpolarization is designed to create a nonequilibrium nuclear magnetization which will make magnetic resonance sensitivity increase 4 to 5 orders of magnitude which is independent of magnetic field strength. This process can be achieved in an external laser-based polarizer by optical pumping (see Section 3.1.2) and the polarization can be up to ~50%.

The HP gases act as contrast agents; thus tone can create images of lung ventilation and dynamics by imaging the inhaled gas distribution (spin density of 3He within the gas spaces of the lung). HP gas ventilation images can detect regional ventilation changes in the lung with much more information than either Spirometry or scintigraphy (22). This technique has been applied to a variety of pulmonary disease models like asthma (3, 93), COPD(55),and bronchiolitis obliterans in lung transplant(27). Production and imaging with HP gases will be discussed in more detail in Chapter 3.

Another direction of HP gas MRI is diffusion imaging. The diffusion coefficient of water is on the order of 2×10^{-5} cm^2/s, and in the presence of the imaging field gradient, self-diffusion leads to a loss of phase coherence in the transverse magnetization and a consequent broadening of the spectrum which ultimately affects the spatial resolution of MR images(16). In contrast, gases usually have a 10^3 -10^5 times greater diffusivity. The high free diffusivity of gas causes the diffusion in the lung airspace to be highly restricted by the alveolar wall. The quantification of the restricted diffusion can ultimately allow the determination of the structural information about the restricting medium—in this case

lung. This also allows precise measurement of alveolar size, microstructure, and regional lung function which will be the main topic of this dissertation.

^{129}Xe provides a unique advantage in measuring chemical diffusion from the lung airspace into the tissues and blood, due to non-zero solubility. The recent shortage of ^{3}He also directed more research effort to improved HP ^{129}Xe approaches. The advantages of ^{3}He, however, outweigh the disadvantages for the purposes of the experiments described here. Compared to ^{129}Xe, ^{3}He is easier to polarize and transport: ^{129}Xe has large spin-rotation relaxation which made the polarization efficiency much lower (108), and its solubility in cell surface coatings leads to a more rapid spin-lattice relaxation (23). More importantly, ^{3}He has larger magnetic moment (~ 3 times of ^{129}Xe) and in consequence larger SNR in the same magnetic field.

1.2.2.2 Conventional ^{1}H MRI

Recently there has been interest in revisiting conventional ^{1}H MRI of lung drove by the clinical potential and the newly emerging MR technique.

Due to the very short T2* in lung parenchyma, imaging techniques which can reduce the echo time (TE) must be used to get *any* signal from lung parenchyma. Different imaging sequences have been developed to reduce TE to be shorter or comparable to the T2* of the lung parenchyma.

One such protocol is called free induction decay (FID)-projection imaging (29, 62, 64). The data acquisition begins as soon as possible after the RF pulse in the presence of a frequency-encoding magnetic field gradient. A half line of the k space is collected by using the fast-decaying signal and the other half is collected during the opposite gradient.

The Fourier transform of a full line of k space is called a projection. TE is zero in this case since the gradient is already on during radiofrequency (RF) excitation.

SWIFT, sweep imaging with Fourier transformation, is another novel 3D radial imaging sequence utilizing gapped frequency swept pulse excitation and nearly simultaneous signal acquisition in the time between the gaps (51, 52). SWIFT has an intrinsically short dead-time (time delay between RF pulse and the data acquisition caused by RF transmission, Transmitter/Receiver switching and signal build-up in the filter), which provides similar sensitivity to very fast relaxing spins similar to other ultra-short TE sequence. A unique advantage of SWIFT is the ability to a wide range of flip angles that can be used at limited B_1, which is essential for optimum SNR and, in steady-state sequences, creating T_1 contrast (117).

1.2.2.3 Pulmonary Imaging of Small Animals

Small-animal models have been widely used in pulmonary research. By using animal models, conditions can be exactly regulated, time course of disease can be carefully tracked and the physiological, biochemical, and pathological alteration induced by lung diseases can be well assessed and quantified. Animal studies of lung have contributed to our understanding of lung structure and function as well as the cellular and molecular mechanism of various lung diseases.

The motivation of small animal imaging comes from the non-invasive nature of imaging itself: the sacrifice of animal at each time point in a longitudinal study is not necessary, in contrast to traditional assays. Imaging also often bears the advantage of high accuracy and precision, obviating the need to survey large animal populations in screening studies.

The big challenge of small animal lung imaging first comes from the size of the animals and breathing volumes. For example, the 1 mm^3 volume element in human lung would be approximately equivalent to 50 μm^3 voxel in mice (42). The development of small-animal imaging instruments now makes it possible to image both structure and function of the lung in small animals.

The interest in micro-CT is rapidly growing with the increasing demand for small-animal imaging. The spatial resolution of micro-CT can approach 5 μm (with significant x-ray radiation dose), yet 50 - 100 μm resolution is feasible for *in vivo* imaging. Thus, a major limitation of micro-CT resolution is the ionizing effect of the x-ray. Chemical and biological changes in tissue exposed to ionizing radiation depend upon the energy absorbed in the tissue which can be measured as radiation dose. A total body radiation dose of 6 Gy (1 Gy represents absorption of one joule of energy per kilogram of absorbing material) is generally considered lethal for small rodents (90). The radiation levels in micro-CT are usually not lethal (a dose of 0.5-1.0 Gy is generally required (90)); however, they are sufficient to intrinsically alter the experimental outcomes especially in longitudinal studies (119).

For small animal MR imaging, a dedicated animal scanner with a high performance gradient system (stronger gradients and faster ramp-up time) is a necessity to achieve a comparable resolution with human imaging.

Another challenge for small animal imaging is that the respiratory and cardiac rates of small animals are up to an order of magnitude faster than in human subjects. The image quality can be significantly degraded by motion artifacts. However, a ventilator can be

used to control the breathing cycle and a trigger signal can be sent to the imager to synchronize imaging acquisition with the specific phase during the breathing cycle. For hyperpolarized gas imaging, a MR and HP gas compatible ventilator needs to be used (41) to administer the HP gas. ECG gating can also be provided to reduce the effect of heart motion by synchronizing the imaging with the cardiac cycle (5, 9).

1.3 Lung Disease Models

1.3.1 Small Animal Models of COPD

Chronic obstructive pulmonary disease (COPD) is a major cause of mortality and disability worldwide and is one of the only major diseases that is increasing (77). It is characterized by distal airspace enlargement (emphysema) and/or small-airway limitation which is not fully reversible, and is associated with an abnormal inflammatory response of the lungs to noxious particles or gases (87). Murine models of COPD have been used effectively and are of critical importance to the study of the pathogenesis of this disease and potential therapeutic interventions (97).

The mouse has become a popular choice for mammalian research because its genomes are very similar to human and the genotype can be manipulated fairly easily. Moreover, there are hundreds of inbred strains and specialized stocks available (13).

There are several experimental models of COPD that exist in mice. These models usually represent only one or few aspects of the disease with the advantage of determine the effects of single or combination insults. There have historically been three types of murine COPD models: 1) Elastase instillation models in which tracheal instillation of a variety of proteinases into the lung; 2) The inhalation of noxious stimuli models among

which the cigarette smoking is most studied; 3) Gene targeting or knockout models. Here only first two models are introduced because they are closely related to our study.

1.3.1.1 Elastase instillation models

Since the initial study by Gross et al. more than forty years ago, the tracheal instillation of tissue-degrading enzymes (proteinases) has been used to create emphysema and become the most commonly used COPD model (32). This model can produce a consistent and impressive airspace enlargement with slow subsequent progression. It is relatively simple to perform and reproduce.

The limitation of the elastase instillation model is that it doesn't show significant inflammation and the airspace enlargement and tends to be more panacinar, rather than the centriacinar disease seen most often in humans without alpha-1 antitrypsin deficiency (19, 70)(Panacinar emphysema is characterized by relatively uniform enlargement of air spaces throughout the terminal bronchioles and alveoli; centriacinar emphysema is characterized by enlargement of air spaces in the proximal part of the acinus, primarily at the level of the respiratory bronchioles). Moreover, it is difficult to extrapolate the findings on the acute response to instillation to the progressive chronic disease in humans (13). However, with replicating many aspects of COPD, this model will continue to be a very important tool to assess the efficacy of therapeutic intervention.

1.3.1.2 Cigarette Smoking Model

COPD is caused by an interaction between genetic host factors and environmental exposure. The major environmental factor is undoubtedly long-term cigarette smoking.

Inhalation of tobacco smoke and other noxious stimuli in mice can induce inflammatory cell recruitment and air-space enlargement (97). Another advantage of this model is that the time course of the induction resembles that of development of the disease in people, and its pathologic and physiologic features are close to that of human.

Even though murine cigarette-smoke-induced COPD has a significant inflammatory reaction and has linked the animal models to humans, the enlargement of airspace appears to be strain-dependent (33), and the exposures to smoke and the morphometric analyses are not well standardized (13, 70). This model is not characterized as well as elastase instillation model and not easy to reproduce as well.

1.3.2 Sendai Virus Infected Mouse Model

Sendai virus (SeV) is a parainfluenza virus first discovered in 1952 Kuroya et al. in Japan during an epidemic of fatal pneumonitis among newborn babies. Since then, Sendai virus has been shown to cause enzootic or epizootic infections in rodents. As Sendai virus causes a respiratory infection in mice, this virus-animal system has been widely investigated in pathogenesis and immunology as a suitable model of respiratory viral infections (44).

Sendai virus mouse model serves as an experimental model of chronic lung disease with pathology that resembles asthma and some elements of COPD in humans (43). In contrast to human pathogens (e.g. RSV, hMPV) to which mice are resistant, SeV relicates at high efficiency and causes injury and inflammation of small airway which resemble the human conditions. In the C57BL/6 mice, a permanent switch to chronic airway disease which is

characterized by mucous production and airway hyperreactivity is triggered after the acute response to SeV infection (84, 104, 109).

Recently, a new type of innate immune response has been identified in this model that drives the translation from respiratory viral infection into chronic inflammatory airway disease (57). The effect of SeV on distal lung airspaces, however, has not been investigated until our study which is detailed in Section 7.2. Our study revealed a link between a small amount of acinar-airway dilatation and earlier virus infection. This result makes us to infer that sendai-virus infection may indeed have the potential to become a valid murine model of COPD.

1.4 Lung Regeneration Model—Pneumonectomy Model

Pneumonectomy (PNX), the surgical removal of major parts of a lung, is an established model of compensatory lung growth (12, 15, 45).

PNX model is a robust model of lung regeneration because that not like other destructive lung disease, the loss of tissue in PNX model is reproducible and well defined, which provides advantage to quantify the compensatory lung growth within the normal remaining lung (47).

Compensatory lung growth following unilateral PNX has been well documented in a number of species (6, 46, 63, 73, 88, 103). The morphometric and biochemical studies have been carried out in dogs, rabbits, ferrets, rats and mice to characterize the response to PNX in order to understand the underlying mechanism and regulation.

Since rodents have more rapid response to PNX and the time course of the normalization is much shorter, they are of particular interest to the pulmonary community. While

intensive research has been performed on rats (11, 61, 89, 96, 111), the detailed characterization of post-PNX lung growth by histology was not reported in mice until recently. Fehrenbach *et al* have demonstrated that mice undergoing the unilateral PNX have a capacity for a rapid and complete compensatory lung growth which includes cellular proliferation and full normalization of lung volume, alveolar surface area and respiratory function parameters (106). It was also reported that the post-PNX lung growth in mice involves neoalveolarization as well as the enlargement of the alveolar size (25).

1.5 Dissertation Overview

A brief overview of the contents of this dissertation is as follows:

Chapter 2, Chapter 3 and Chapter 4 cover the main methods used in this study. It started with hardware: the mechanism of RF coils is introduced with the stress on the double resonance RF coil which was used in this study; the design and working principle as well as operation details of the small animal ventilator is described in the second section. The first section of Chapter 3 is about the hyperpolarization technique including the basic physical principles of hyperpolarization and the optical pumping technique we used for hyperpolarized ^{3}He imaging. The second section is for imaging; basic gradient echo sequence with applications in ventilation and diffusion imaging in our study are discussed. Chapter 4 presents the theory of ^{3}He morphometry technique which is the theoretic basis for all the experimental studies in this dissertation.

Chapter 5 details all the experimental procedures involved in the ^{3}He morphometry technique. The first section describes the animal anesthesia, intubation and ventilation on the ventilator. Hyperpolarization of ^{3}He gas and proper gas delivery to the animal is

discussed. The whole imaging process with detailed imaging parameters is documented in this chapter followed by some special considerations during real imaging. Imaging analysis including Bayesian analysis and the interpretation of Bayesian results completes this chapter.

Chapter 6, Chapter 7 and Chapter 8 presents the results for the implementation of ^{3}He morphometry in healthy mice *in vivo* and the application of the technique on lung disease models (mainly on COPD models) and regeneration model respectively. The results are discussed in each chapter. The comparisons to micro-CT studies are also included in the studies of Sendai virus mouse model and pneumonectomy mouse model.

Chapter 9 closes out the dissertation by summarizing the specific accomplishments of this study. Final conclusions are drawn from studies of different mouse models. The limitations of our technique are included and future directions are discussed

Chapter 2

Methods: Hardware and Equipment

2.1 RF Coils

The radiofrequency (RF) coil, also known as an RF resonator, is an essential part of an MRI system. The coil is electrically resonant at the nuclear resonance frequency in an external magnetic field B_o, and it often has two functions – transmission and reception of radio-frequency energy resonant with nuclear spins. One generates RF pulses to flip the nuclear spins in the object to be imaged ("transmit"); for "receive", the transmitter is silenced and the coil is sensitive to RF energy from the nuclei as they precess around the field B_0 after the RF transmit pulse. Over the past years, many different types of RF coils have been developed, but they can largely be divided into two types: 1) Volume coils: Helmholtz coils, saddle coils, and birdcage coils (53) belong to this category. They are often used both for transmission and reception. 2) Surface coils: They are mainly used as receive coils because the B_1 field generated has poor homogeneity, but coil-signals can be combined post-imaging to create high-quality images.

A common RF coil scheme in NMR is a RLC resonant circuit. Consider a RLC resonant circuit illustrated in **Figure 2.1**. Based on Kirchhoff's law, we have

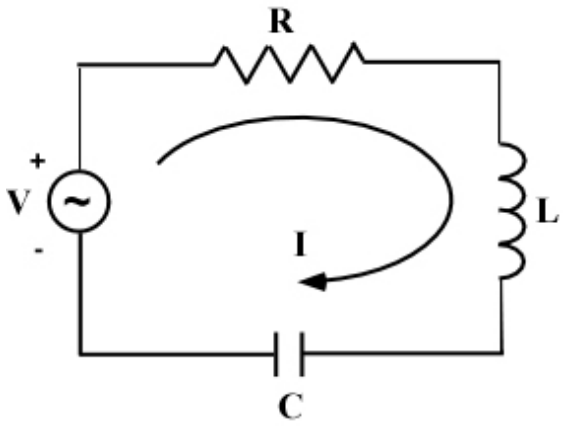

Figure 2.1: RLC circuit

$$RI - \frac{i}{\omega C} I + i\omega L I = V \tag{2.1}$$

where ω is the resonance frequency of the nucleus of interest.

$$I = V\left[R + i\omega L - \frac{i}{\omega C}\right]^{-1}$$

$$= V\left[R + i\frac{L}{\omega}\left(\omega^2 - \frac{1}{LC}\right)\right] \tag{2.2}$$

Then the resonance condition (defined to be the condition required to make the impedance real in which case the current flow in the coil is maximized) is

$$\omega = \frac{1}{\sqrt{LC}} \tag{2.3}$$

A doubly tuned RF coil has two resonance frequencies. It is critical for ^{3}He lung MRI because ^{1}H MRI is usually taken prior to ^{3}He MRI for anatomic orientation; the double-resonance coil allows imaging on both resonance frequencies without moving the animals between different coils. This kind of coil is often designed as a cylindrical birdcage coil

or as two birdcage coils arranged in a coaxial manner (26). The major problem with this approach is the relatively complicated structure to build.

Below is a simple design scheme to realize a double-tuned coil by using fewer reactive elements. In practice, resonance can be realized by adding a tuning circuit to cancel out the complex part of the impedance of the coil. For a single-resonance MR coil, a capacitor can be used in series with the coil and tuned for electrical resonance. For a double-resonant coil, a tuning network consisting of a parallel LC trap in series with a capacitor can be used to tune to resonance (**Figure 2.2**).

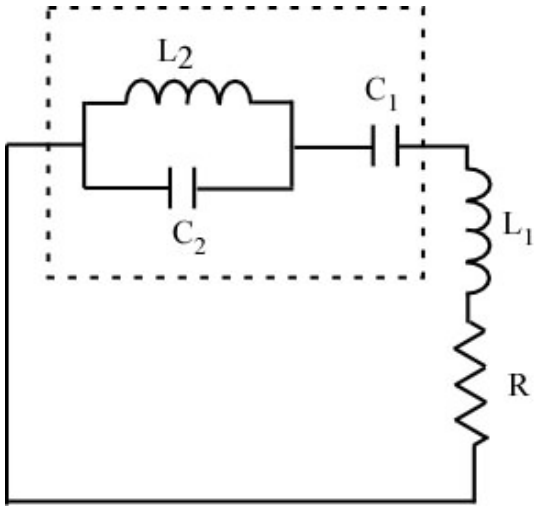

Figure 2.2: Schematic of a double resonance tuned circuit; R is the RF resistance of the coil. The part in the dashed box is the tuning network consisting of a parallel LC trap in series with a capacitor.

The reactance for the tuning network is

$$X = -\frac{1}{\omega C_1} + \frac{1}{\frac{1}{\omega L_2} - \frac{1}{\frac{1}{\omega C_2}}} \tag{2.4}$$

$$= -\frac{1}{\omega C_1} + \frac{\omega L_2}{1 - \omega^2 L_2 C_2}$$

The reactance of this network (as a function of frequency) will begin capacitive, then pass through a pole at the frequency corresponding to the resonance of the LC trap, and then become capacitive again (95).

The condition of resonance can be found by setting the total reactance equal to zero. We will have two different resonant frequencies by solving this condition. When frequency is high, the parallel LC trap is equivalent to the capacitor C_2 alone, and the resonant frequency is

$$\omega_{High} \sim \sqrt{L_1 (\frac{1}{C_1} + \frac{1}{C_2})} \tag{2.5}$$

When frequency is low, the LC trap is equivalent to the inductance L_1 alone, and the resonant frequency is

$$\omega_{low} \sim \sqrt{\frac{1}{(L_1 + L_2) C_1}} \tag{2.6}$$

This method of doubly-tuned MR coils can be extended very simply to more than two frequencies by adding more traps in series to the tuning next work.

Typically the RF coil is physically attached to the cable connecting the transmitter or receiver. Instead of a physical connection (e.g., capacitive coupling), we use the inductive coupling loop to inductively couple to the resonator (**Figure 2.3**). The benefit of inductive coupling is that there is no electrical connection between the coaxial line to the transmitter/receiver and the resonator which is exceptionally useful with animal or human MRI. The resonance circuit can be physically removed, attached to the animal or positioned, without disturbing electrical connections to the MRI system.

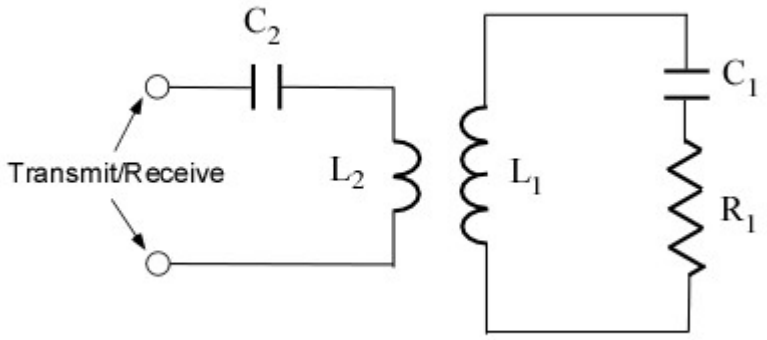

Figure 2.3: Schematic of an inductively coupled NMR resonator

2.2 Small Animal Ventilator

For pulmonary imaging of small animals, a ventilator is usually used to precisely control the pressure and the volume of delivered gas, in addition to supplying anesthesia. The full control of gas delivery is especially important in HP gas imaging, because using all-plastic parts is crucial for maintaining a high polarization during imaging.

For humans, imaging is accomplished by having the subject breathe in HP ^{3}He and hold the breath during imaging. For small animals, a ventilator is needed to administer the respiration with the animal anesthetized.

There are commercially available MR-compatible small animal ventilators, most of which also offer external triggering for synchronizing ventilation with imaging. Those systems usually do not offer flexibility of breathing cycle control required for many types of lung MRI, and the wetted parts are often made of depolarizing materials like metals. So we used a home-built small animal ventilator which is compatible with both the MR system and HP gas. This ventilator was originally built by Dugas J. P. et al. (24) in our lab and optimized recently for the work described here.

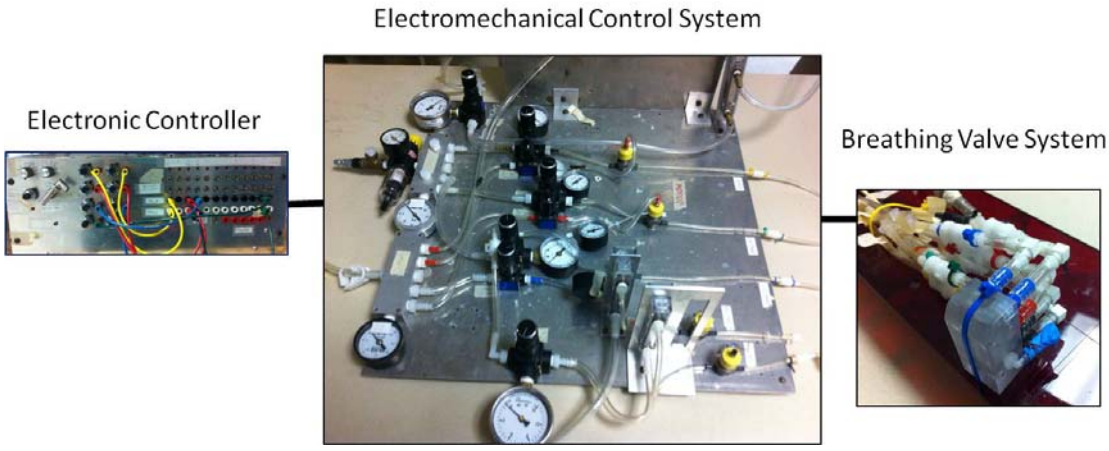

Figure 2.4: Small animal ventilator. The electronic controller governs the timing of the solenoid valves on the electromechanical control system which controls the breathing valves located on the animal/RF coil tray.

The ventilator mainly consists of three parts: electronic controller, electromechanical control system and breathing valve system (**Figure 2.4**). During imaging, the first two

parts are put on a rolling cart and located in the fringe field approximately 1.5 meters from the magnet. Note that the gas supply lines are mounted on the electromechanical control system. The small block containing the breathing valves is mounted on the animal/RF coil tray which is in the magnet when imaging (the tray was pulled out shown in the figure).

2.2.1 Breathing Valve System

The breathing Valves are made by a latex sheet sandwiched between two LEXAN® (GE polycarbonate) halves. All materials were carefully chosen to be compatible with the magnet and HP ^{3}He gas.

In one LEXAN® half, there are gas passageways connecting the four holes on one side to the outlet leading to the animal's mouth on another side (Figure 2.5). We used two of the holes to supply O_2 and ^{3}He gas, respectively. The third hole is used to output the exhaled gas from the animal. A pressure transducer (Honeywell, Model No. 24PCAFA6D) is connected to the fourth hole which measures the exact same pressure at the animal's trachea.

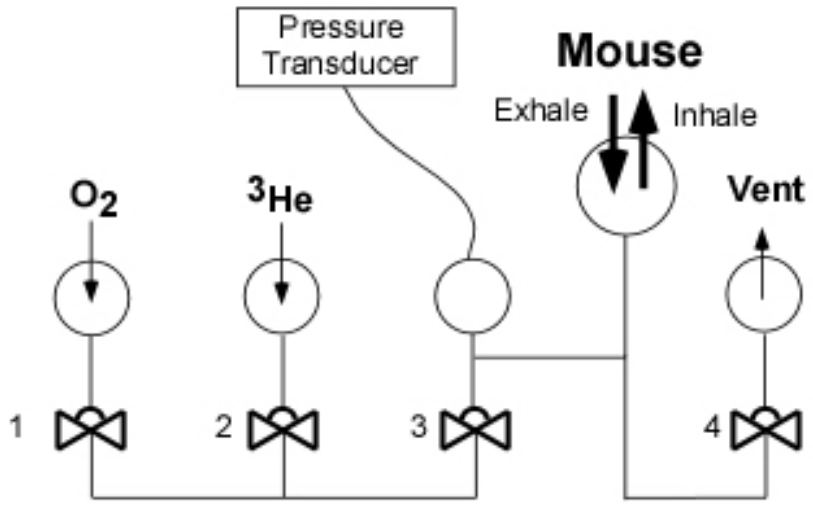

Figure 2.5: Schematic of gas passageways in the breathing valve system. Four pneumatically controlled valves 1,2,3,4 are controlled by electromechanical control system.

In **Figure 2.5**, The open and close of the passageways for O_2 supply, ^3He supply and vent (exhale) in one LEXAN® half are controlled respectively by diaphragm valves 1,2 and 4. Valve 3 is set just before these three passageways getting into the animal mouth in order to provide a extra shut-off. The working principle of the diaphragm valves is shown in **Figure 2.6**. Every passageway discuss above has two openings adjacent to the latex diaphram. On the other side of the diaphram in the other LEXAN® half, there is a hemisphere hollow connected to the gas line which comes out from one specific solenoid. When there is compressed air supplied in the gas line leading to the hollow, the diaphram will be pushed against the other half containing the two openings of one passageway, which will close the passageway. If it is vacuum supplied at left, the diaphram will be

pulled away from the other half which will allow the passage of gas through the two openings.

One important issue that needs to be addressed when designing a mouse ventilator is to make the dead volume as small as possible. Dead volume is the volume of space between the fresh gas supply and the gas exchange spaces. When a mouse is attached to a ventilator, the dead volume includes the anatomical dead volume of mouse itself and the dead volume of the ventilator. The maximum tidal volume of a mouse is ~ 0.18 cc (92) which the total dead volume should be compared to. Our breathing valve system is small, with a size ~ 2 cm × 2 cm × 3.5 cm. The passageways inside are 0.762 mm in diameter. The dead volume of the breathing valve system is the space between the gas supply hole next to the latex sheet and the attachment point to the mouse. This dead volume was calculated to be less than 50 μL, which is considerably smaller than the 250 μL tidal volume we supply.

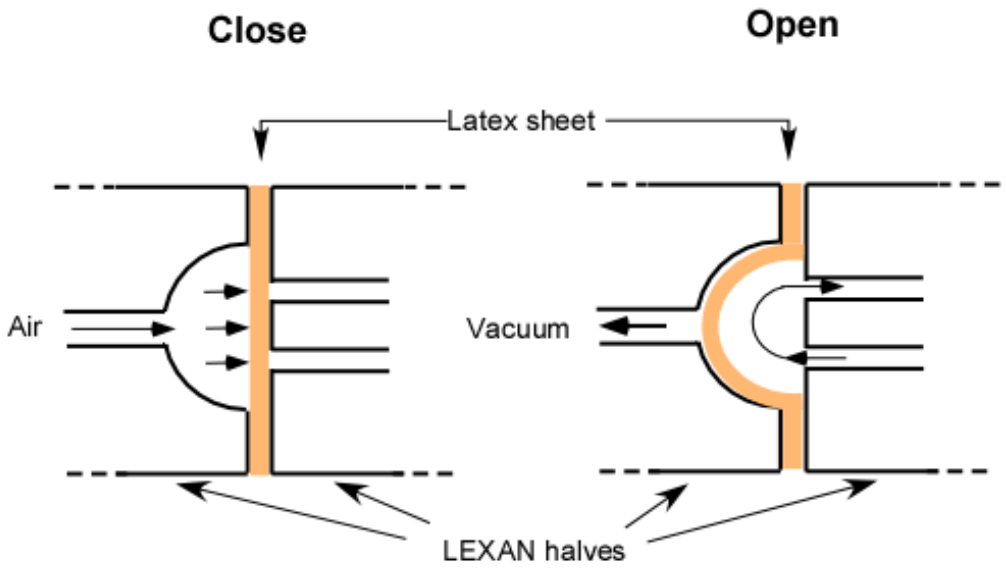

Figure 2.6: The diaphragm valve in the breathing valve system. The close and open of the valve is controlled by air and vacuum pulses coming from electromechanical control system.

2.2.2 Electromechanical Control System

The electromechanical control system supplies the air and vacuum pulses to drive the breathing valve.

The main part of this system is four solenoid valves. The solenoid valves we used are single-pole, double-throw (SPDT) switches driven by 24 VDC. Each valve can switch between its two inputs -- air or vacuum in order to close or open the diaphragm valves in the breathing valve system. Note that the de-energized state of the solenoids corresponds to the vacuum pulse. This guarantees that in the case of power failure, all the valves in the breathing valve system will remain open, which will prevent the mouse to be caught in a breath hold period and will allow it breathe on its own normally.

Air and vacuum are supplied by sources in the buiding. The high-pressure compressed air coming out the outlet on the wall is connected to our system by a heavy-duty air hose. A regulator is used to drop the air pressure to ~20 psi before the line is split into four small lines directing to four smaller-range pressure regulators (0-10 psi). Each regulator can finely regulate the air pressure supplied to the corresponding diaphragm valve. The output from each regulator is one input of each solenoid valve. The vacuum branches into separate lines and is regulated by the vacuum regultors in a similar fashion as the air lines.

2.2.3 Gas Supply

For convenience, the O_2 and ^3He gas supply lines are also mounted on the electromecnanical control system. Each line has a pressure regulator (0-10 psig), a pressure gauge and a flow meter.

O_2 is supplied by the oxygen line in the building. It is mixed with anesthetic by an isoflurane vaporizer as is routine for animal imaging.

For ^3He supply we must consider that the metal parts in the pressure regulator, pressure gauge and flow meter will depolarize the spins of hyperpolarized ^3He; we thus use a gas reservoir (Figure 2.7) to prevent the exposure of the ^3He gas to paramaganetic, ferromagnetic, or other depolarizing materials. The regulator, pressure gauges and flow meters are mounted along the N_2 line (supplying driving pressure to the ^3He tedlar bag) instead of ^3He line. The end of the N_2 line goes into the leak-free reservoir made by ~ 2L plastic bottle. ^3He gas is stored in a Tedlar bag inside the reservoir. N_2 gas flowing into the bottle at above-atmospheric pressure can squeeez the ^3He gas out of the Tedlar bag,

which isconnected to the plastic hose directly to the breathing valve. By regulating the pressure and flow of N_2 gas, the pressure and flow of ^3He in the bag can be controlled providing that the reservoir is leak-free.

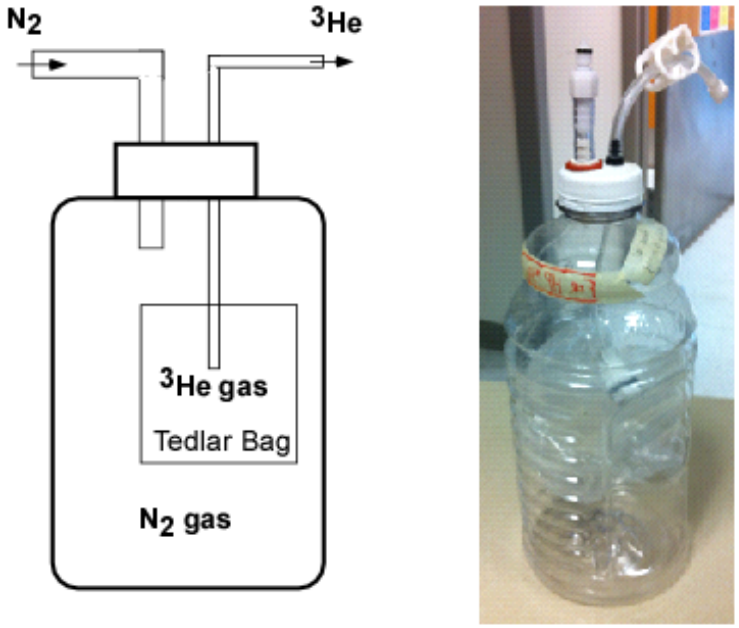

Figure 2.7: Gas reservoir used for ^3He supply

Since the reservoir needs to be taken out of the ventilator to refill with ^3He gas, we made a replacement bottle with the exactly same setup. Instead of ^3He, we fill N_2 gas into the Tedlar bag. This replacement bottle is used during all the other time during imaging except for HP gas imaging.

2.2.4 Electronic Controller

The electronic controller (**Figure 2.8**) governs the timings of the switching of the solenoid valves in the electromechanical system. A timing scheme of a breathing cycle

can be uniquely defined by specifying the total time period, the starting (valve open) and stopping (valve close) time points in one breathing cycle for each solenoid valves.

It has 12 channels which can control up to eight 24 VDC, solenoid valves and two 120 VAC, solenoids.

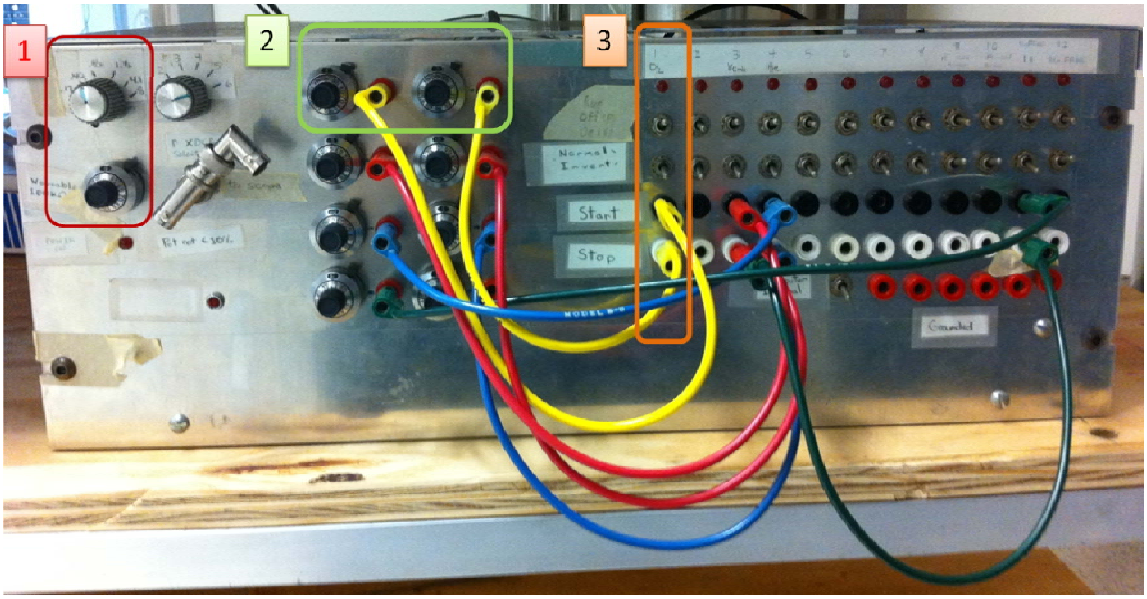

Figure 2.8: The front panel of electronic controller.

The total time period for one respiration cycle can be controlled by the two knobs on the front panels (Box 1 in Figure 2.8). One knob (upper one in the box) provides coarse tuning (0.17s, 0.40s, 0.85s, 1.7s, 4.1s, 8s) and the other one attached to a potentiometer is fine tuning (0-100% of the reading from coarse tuning).

During one respiratory cycle, the timing of each solenoid can be controlled by a set of knobs and toggle switches shown in **Figure 2.8**. Timing controls for one solenoid valve are circled by boxes 2 and 3. The schematic of these controls are depicted in **Figure 2.9**.

The two potentiometers on the left are connected to the "start" and "stop" port on the right which assign a specific time period in one breathing cycle for the breathing valve to open. This time period assigned by the two potentiometers is only effective when the upper toggle switch is in "Run" position. The breathing valve will keep completely open or closed for the whole breathing cycle if the switch is in "On" or "Off" position respectively. The lower toggle switch gives flexibility to invert the start and stop points.

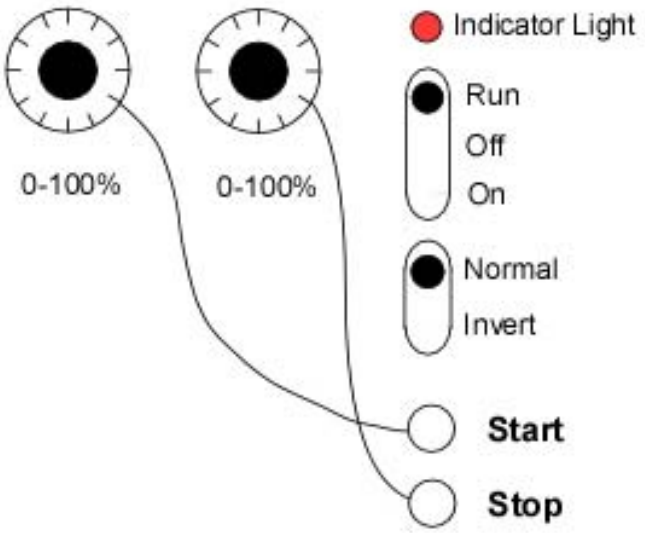

Figure 2.9: Schematic of the knobs and toggle switches on the electronic controller that can control timing of one solenoid valves on the electromechanical control system.

Another function of electronic controller is to trigger image acquisition for respiratory gating in MRI. A trigger signal from the ventilator was used to control the image data acquisition beginning at an exact time point during one respiration cycle. The electronic controller sends out TTL pulses from a BNC jack directly connected to the "external trigger" port on the Varian system. By using one pair of potentiometers as mentioned above (for the "start" and "stop" ports), the time period for triggering can be specified.

The triggering can also be synchronized with any solenoid control by directly connecting to the pair of potentiometers controlling that solenoid. Note that in real experiments the timing of the triggering is a bit after the solenoid fires, which is likely due to the time lag of the pressure wave travelling through the 1.5-m narrow line. As a result, the beginning of the trigger needs to be manually adjusted accordingly.

Chapter 3

Methods: Hyperpolarized ^{3}He MRI

3.1 Hyperpolarization of ^{3}He Gas

3.1.1 The Physics Background of Hyperpolarization

For decades, MRI has been developed as a noninvasive technique which shows great diagnostic value with superior soft-tissue contrast. However, MRI is limited by an intrinsically low sensitivity, compared with other imaging modalities (computed tomography, positron emission tomography, single-photon emission computed tomography, etc.). This originates from the small population difference between nuclear energy states in thermal equilibrium. For a spin-1/2 system, there are two possible energy states, parallel ("spin up") and anti-parallel ("spin down") to the external field. The "nuclear-spin polarization" P_N is defined as:

$$\mathbf{P_N} = \frac{|\mathbf{N_+} - \mathbf{N_-}|}{\mathbf{N_+} + \mathbf{N_-}} = \frac{|\mathbf{N_+} - \mathbf{N_-}|}{\mathbf{N}} \tag{3.1}$$

where N_+ and N_- denote populations in the "up" and "down" positions, respectively.

In thermal equilibrium, the relative distribution of the spins is given by the Boltzmann factor. If the external magnetic field is $\mathbf{B_0}$, the energy E_+ of the "spin up" state is μB_0 and E_- of the "spin down" state is $-\mu B_0$.

$$P_N = \frac{\left|\exp\left(-\frac{E_+}{k_B T}\right) - \exp\left(-\frac{E_-}{k_B T}\right)\right|}{\exp\left(-\frac{E_+}{k_B T}\right) + \exp\left(-\frac{E_-}{k_B T}\right)}$$

$$= \tanh\left(\frac{\mu B_0}{k_B T}\right) \tag{3.2}$$

Typically, the thermal energy of the sample at temperature T exceeds the energy difference between the nuclear spin states in a magnetic field B_0 by several orders of magnitude. So in "high-temperature approximation" ($\mu B_0 \ll k_B T$), the equilibrium polarization can be written as:

$$P_N \approx \frac{|\mu B_0|}{k_B T} = \frac{\frac{1}{2}|\hbar\omega|}{k_B T} = \frac{|\gamma|\hbar B_0}{2k_B T} \tag{3.3}$$

where γ is the gyromagnetic ratio, $\hbar$ is Planck's constant divided by 2π, and k_B is Boltzmann's constant. The thermal equilibrium polarization is very low: at a magnetic field of 1.5 T it is only 5×10^{-6} for ^1H at body temperature. In other words, only about one out of a million nuclei contributes to the signal in a typical clinical MRI scanner.

Besides polarization, the signal-to-noise ratio (SNR) is also proportional to the concentration of the nuclear spins. Generally, the weak nuclear polarization is compensated by a high concentration (i.e. the high concentration of protons in biological tissue).

According to (3.3), the polarization can be increased by increasing the magnetic field or decreasing the temperature. The former has been the motivation for developing MR

systems with higher magnetic field as signal increases with field, but costs and RF-energy deposition also increase, along with the change of relaxation time (shortening of T_2 and lengthening of T_1) and susceptibility and chemical shift artifacts (71). Decreasing temperature to near absolute zero for increased signal is obviously unsafe for most biological samples to be studied.

A different path to increase the polarization is to create a non-equilibrium distribution of the nuclei: the so-called "hyperpolarized" state where the population difference of different states is enhanced by several orders of magnitude compared with the thermal equilibrium and is independent of the magnetic field for a period of time equivalent to at least T_1. A number of methods have been proposed to hyperpolarize the nuclear spins: spin-exchange or metastability-exchange optical pumping (SEOP or MEOP, respectively) (54), para-hydrogen-induced polarization (PHIP)(30, 35), and dynamic nuclear polarization (DNP)(1). The optical pumping method has been successfully investigated to polarize some of the noble gas isotopes for lung MRI. The PHIP and DNP methods have been used for hyperpolarization of a wide range of organic molecules containing ^{13}C.

Here we will limit our discussion only to the spin-exchange optical pumping method.

3.1.2 Optical Pumping

The application of hyperpolarized ^{3}He and ^{129}Xe to pulmonary MRI has seen remarkable development in the past 20 years. The hyperpolarization of these noble-gas isotopes is made possible through laser-optical pumping. Angular momentum from circularly polarized laser light is transferred to outer electron spins and ultimately transferred to the nuclear spin of interest. There are two basic schemes that have usually been employed:

metastability-exchange optical pumping (MEOP) (20) and spin-exchange optical pumping (SEOP) (107). In both schemes, the transfer of angular momentum is achieved by two stages: from light to electron spins and then from electron spins to the noble gas nuclear spins. Another common feature of both methods is that a glass cell is used to hold the noble gas; the laser light is directed through the cell during polarization process.

In MEOP, a RF discharge is ignited in the cell at $p \approx 1 - 10$ Torr to populate the metastable $^3S_1$ state of ^{3}He atom. Optical pumping with right-handed circularly polarized 1083 nm laser light, corresponding to transitions from the $^3S_1$ state to the $^3P_0$ state, leads to a large electron polarization in the metastable state, which is immediately transferred to the ^{3}He nucleus via intraatomic hyperfine coupling. Rapid collisions enables electron states exchange between polarized metastables and unpolarized atoms in the ground state without affecting the nucleus of either atom, which eventually produce nuclear polarized ^{3}He atoms in the ground states.

The advantage of MEOP is the intrinsically faster production rate and largest maximum ^{3}He polarization (~ 1STP-liter/hour at > 60% polarization) (7). However, the low pressure means that the ^{3}He in MEOP is optically thin, so long and narrow OP cells are required in order to make the best use of the laser light (75). The polarized gas also needs to be compressed to atmospheric pressures without significant polarization loss, which requires significant engineering in all-plastic or alternative-material compressors (8). In addition, it has higher requirement for laser compared with SEOP.

In SEOP, alkali metal (e.g. Rubidium) serves as an intermediary in the transfer of angular momentum. First, the cell is heated to 160 - 200 °C in order to vaporize Rb to a density

appropriate to the amount of available laser light (56). Circularly polarized laser light is absorbed by the Rb vapor at a wavelength of 795 nm, which corresponds to the principal electric dipole (D_1) transition ($5S_{1/2} \rightarrow 5P_{1/2}$). This will cause nearly 100% polarization of the Rb valence electron by depopulation optical pumping (37) (see **Figure 3.**1). The second stage of transferring the angular momentum occurs in collisions between the polarized Rb atoms and the ^{3}He atoms via hyperfine interaction. After the collision, the angular momentum is stored in the form of polarized ^{3}He nuclei and Rb is restored to its pervious spin orientation by continued OP, ready for collision with ^{3}He atom again.

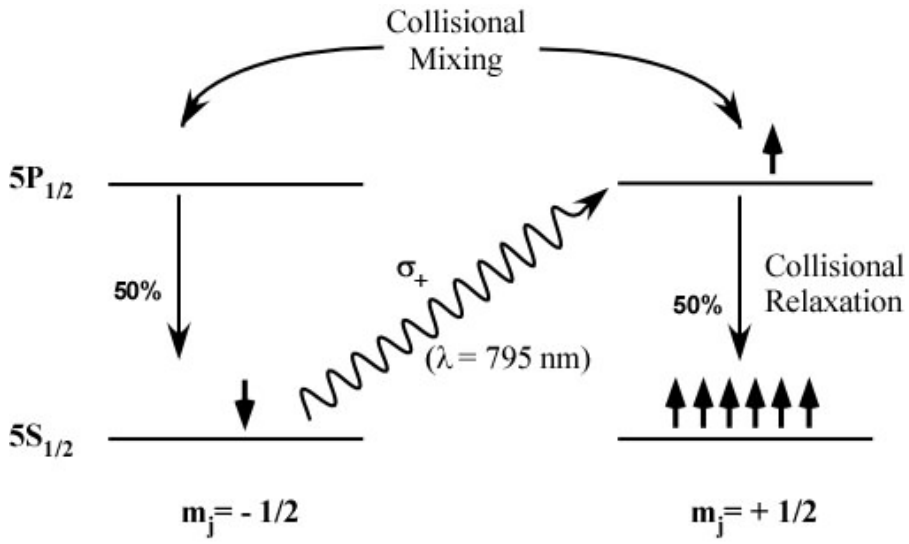

Figure 3.1: Schematic representation of the polarization of Rubidium (Rb) in the vapor phase. Using a high power laser light (λ=795 nm), angular momentum from right circularly polarized light σ_+ is passed from photons to Rb valence electrons. Under conservation of angular momentum, excited electrons follow the selection rule $\Delta m_j = +1$, which only allows transition from $m_j = -1/2$ state ($5S_{1/2}$) to the $m_j = +1/2$ state ($5P_{1/2}$). Then through collisional mixing the excited electrons are evenly distributed between the spin +1/2 and -1/2 states of the 5p orbital. From the excited state, electrons decay back to

the $5S_{1/2}$ orbital, through a process known as collisional relaxation, with half decaying to the $m_j = +1/2$ state and half decaying to the $m_j = -1/2$ state. The small amount of N_2 gas prohibits radiative photon emissions which may cause radiation trapping. The laser light re-excites electrons which decay to the $m_j = -1/2$ ground state. This process, known as depopulation optical pumping, removes electrons from the $m_j = -1/2$ state in order to fill the $m_j = +1/2$ state on which the atoms cannot absorb the laser light.

SEOP system has the advantage of cheap powerful portable lasers and operating at helium pressures between 1 and 10 atm but production rate is relatively slow. This can be and has been improved by using more powerful lasers with narrower frequency which better match the alkali-metal absorption profile.

In our lab, two home-built polarizers and a General Electric polarizer were used, producing 0.5-1.0 L ^{3}He gas at 30% - 50% polarization.

3.2 Gradient Echo MRI

The peculiarity of the hyperpolarized gas imaging compared to the conventional MRI is that the large nonequilibrium polarization of the nuclei is nonrenewable. In addition, the noble gases have large diffusion constants. In results, fast pulse sequences need to be used and special considerations must be taken to get high quality images by making a good use of the non-renewable hyperpolarization.

The pulse sequence we used most in our study is based on gradient echo pulse sequence.

3.2.1 Gradient Echo Pulse Sequence

Figure 3.2 is the diagram for a conventional 2D gradient echo sequence. First, the slice selective gradient is applied along z axis. The slice selective lobe is during the RF pulse and followed by a rephrase lobe. The area under the rephrase lobe is equal to half of the area under the slice select lobe. After the rephrase lobe, all the transverse magnetization within the selected slice is in phase, with a common accumulated phase value $\phi = 0$. After the slice selective gradient, a phase encoding gradient is applied on y axis. The magnetization accumulates a y-dependent phase $\phi = -\gamma G_y y \tau_y$ when a gradient G_y is kept on in the y direction for a time $\tau_{PE} = \tau_y$. The gradient G_y will be varied in step-like fashion (step size ΔG_{PE}) in order to gather information about the y-dependence of the spin density. The third gradient is applied along x direction to read gradient echo structure. The gradient G_x has a negative dephasing lobe followed by the read lobe, during which the signal is measured. After the dephasing lobe, the phase accumulated is

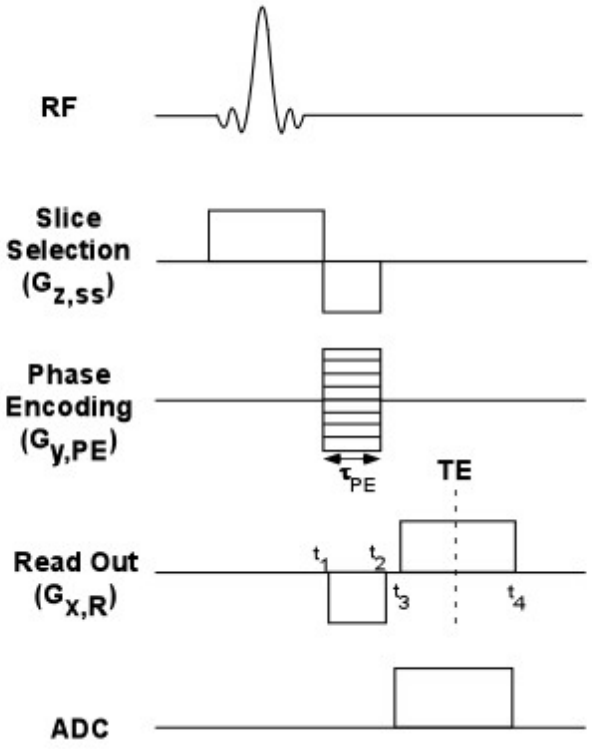

Figure 3.2: A typical 2D gradient echo sequence

$$\phi = +\gamma G_x x(t - t_1) \quad t_1 < t < t_2 \tag{3.4}$$

The phase when the read lobe is applied is

$$\phi = +\gamma G_x x(t_2 - t_1) - \gamma G_x x(t_3 - t) \qquad t_3 < t < t_4 \tag{3.5}$$

The gradient echo occurs when the phase return to zero, that is

$$t = t_3 + t_2 - t_1 \equiv T_E \tag{3.6}$$

This time is during the second gradient (read) lobe when the evolved area under read lobe just cancels the area of the first (dephasing) lobe, which can be expressed as

$$\int G(t)dt = 0 \tag{3.7}$$

The signal is obtained during the entire read lobe by measuring the received emf in the presence of a gradient echo structure in the read out direction. This gives out a line with a fixed G_y value in the k-space set of 2D Fourier transform values of the effective 2D spin density for the selective slice.

Spoiler gradients sometimes are applied along different axes to dephase the residue transverse magnetization based on the T_2^* of the nucleus.

In our studies, gradient echo sequence was used both for ^{1}H MRI and ^{3}He MRI.
For ^{1}H MRI, a gradient echo sequence (scout protocol in Vnmrj) was generally used for locating animals in the magnet and anatomical orientation. The scout protocol acquires imaging slices in each of the three cardinal planes in order: axial, coronal, and sagittal. The scan takes a few seconds. A very short TE (~0.99 ms) is also achieved by gradient echo sequence to reveal inflammation in lung parenchyma in certain pulmonary models of mice.

Gradient echo sequence has been intensively used in hyperpolarized gas lung MRI since the very early studies in this field. Usually a small flip angle was used because that the repetitive sampling of the residual longitudinal magnetization causes nonrenewable depletion. A variable-flip-angle approach was generally used to ensure a relatively constant magnetization during the acquisition of a given image (123).

However, mouse lung imaging with HP ^{3}He using small tip angle still suffered from poor S/N. So we scan k-space with the delivery of many breaths of HP gas to the animal, which means that each RF pulse is applied to a fresh bolus of HP ^{3}He gas every respiratory cycle. So we are able to use a constant large flip angle to utilize the polarization to the greatest extent.

To get images of a 3-D volume, one can use 3D methods with short TR or the multi-slice 2D method where the 2D imaging techniques are generalized to a series of selected slices to cover a 3D volume. We took the latter approach.

3.2.2 ^{3}He Ventilation Imaging with Gradient Echo Sequence

After inhalation of a bolus of HP ^{3}He, the ^{3}He gas diffuses rapidly to fill the airspaces of the lungs. Ventilation image refers to the spin-density image of ^{3}He during the breath-hold which allows visualization and measurement of the ventilated airways and alveolar spaces. Homogenous distribution of ^{3}He signal within the lung region represents normal ventilation. HP ^{3}He ventilation imaging demonstrated a heterogeneous distribution in a variety of diseases, indicating impaired regional ventilation (55).

Fast Low Angle Shot (FLASH) sequence is a gradient echo sequence with low flip angles. In human, a 2D FLASH sequence (Siemens) was typically used during a single breath-hold (10-15s) after inhalation of a discrete volume of HP gas. Because the mouse lung is about ~ 10^{3}-10^{4} smaller than human's, multiple breaths were usually used in ^{3}He ventilation imaging to achieve high spatial resolution.

3.2.3 Multi-b Diffusion-weighted ^{3}He MRI

Diffusion-weighted imaging (DWI) has been applied to the evaluation of intracranial diseases, such as cerebrovascular accidents, trauma, epilepsy, depression, dementia, and neurotoxicity for more than two decades.

The ^{3}He diffusion MRI used a gradient-echo version of DWI. For hyperpolarized gas imaging, gradient echo sequence is preferred to spin echo because the hyperpolarized spins are not renewable, the π pulse should be avoided. The pulse sequence is shown in **Figure 3.3**. The bipolar diffusion sensitizing gradient is sandwiched between the RF excitation pulse and readout gradients in a regular gradient echo sequence.

The purpose of this bipolar diffusion gradient is to magnetically label spins carried by the molecules. For a bipolar gradient shown in **Figure 3.3** of duration$(\Delta + \delta)$, the phase shift ϕ_1 induced by the first gradient lobe is

$$\phi_1 = \gamma \int_{t_1}^{t_1+\delta} \mathbf{G}(t') \cdot \mathbf{x}(t')dt \tag{3.8}$$

where γ is the gyromagnetic ratio, **G** is the diffusion gradient and $\mathbf{x_1}$ is the displacement function of the molecule during the time of the first diffusion lobe (supposed to be

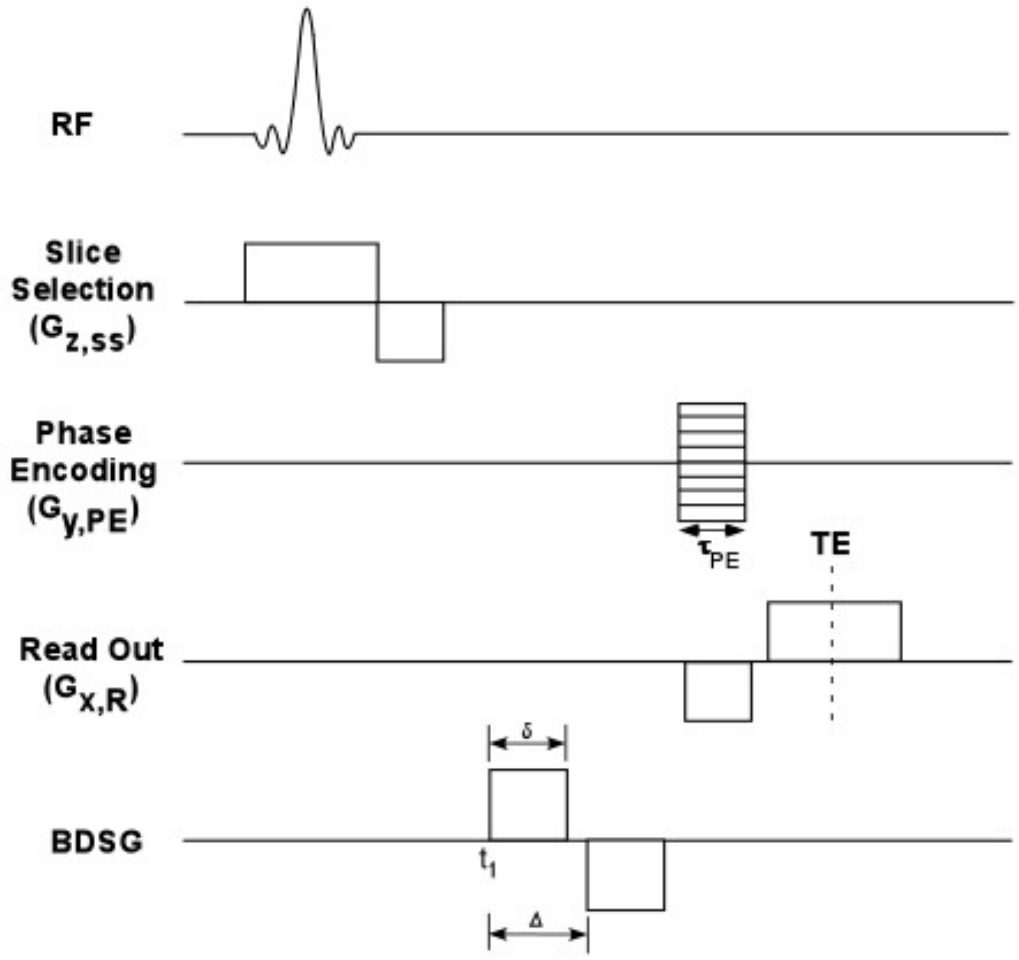

Figure 3.3: Diffusion weighted gradient echo sequence. For the bipolar diffusion sensitizing gradient pulse (BDSG), δ is the pulse duration and Δ is the time between the onset of the first and second gradient pluses.

constant during the δ). Similarly, the phase shift ϕ_2 induced by the second gradient lobe is

$$\phi_2 = \gamma \int_{t_1+\Delta}^{t_1+\Delta+\delta} \mathbf{G}(t') \cdot \mathbf{x}(t') dt \tag{3.9}$$

The net dephasing is therefore

$$\delta(\phi) = \phi_2 - \phi_1$$

$$= \gamma\left(\int_{t_1+\Delta}^{t_1+\Delta+\delta} \mathbf{G}(t') \cdot \mathbf{x}(t')dt - \int_{t_1}^{t_1+\delta} \mathbf{G}(t') \cdot \mathbf{x}(t')dt\right) \tag{3.10}$$

If the spin stays still at one position during the whole process, the net dephasing is zero. In the case of diffusion with random Brownian motion of molecules, the displacement function **x** (t) is random and the total magnetization is the vector sum of the magnetic moments of the individual nuclei which accumulate different phase shifts. The will ultimately lead to a signal attenuation but no net phase shift. The total magnetization can be expressed as the vector sum of the magnetic moments of the individual nuclei, which may have different trajectories:

$$M = M_0 \sum_{j=1}^{N} \exp\left(i\delta\left(\phi_j\right)\right) \tag{3.11}$$

The Bloch equations with diffusion relate the time evolution of the net magnetization to the applied magnetic field:

$$\frac{d\vec{M}}{dt} = \gamma\vec{M} \times \vec{B} - \frac{M_x\hat{x} + M_y\hat{y}}{T_2} + \frac{(M_0 - M_z)\hat{z}}{T_1} + D\nabla^2\vec{M} \tag{3.12}$$

where D is the molecular self-diffusion coefficient.

The solution to (1.15) contains a real, time-dependent part that represents the attenuation due to diffusion:

$$\Psi(\mathbf{r}, t) = M(t)\exp\left(-i\mathbf{r} \cdot \mathbf{k}(\boldsymbol{t})\right) \tag{3.13}$$

Where

$$\mathbf{k}(t) = \gamma \int_0^t \mathbf{G}(t')dt' \tag{3.14}$$

The solution of M(t) for an isotropic medium at echo time M(TE) is then given by

$$\frac{M(TE)}{M_0} = \exp\left(-D \int_0^{TE} \mathbf{k}(t') \cdot \mathbf{k}(t')dt'\right) \tag{3.15}$$

If we define the "gradient factor" b as

$$b = \int_0^{TE} \mathbf{k}(t') \cdot \mathbf{k}(t')dt' \tag{3.16}$$

The signal attenuation is

$$\frac{M(TE)}{M_0} = \exp(-bD) \tag{3.17}$$

The details for this derivation are given in (65).

The b-value depends on the waveform of the gradients in the pulse sequence. For a rectangular bipolar gradient in **Figure 3.3**:

$$b = \gamma^2 G^2 \delta^2 \left(\Delta - \frac{\delta}{3}\right) \tag{3.18}$$

Chapter 4

Method: Theoretical Background of ^{3}He Morphometry

The theory for MRI-based ^{3}He lung morphometry was first developed and validated for human lungs (102, 120, 121), and was recently extended to *ex-vivo* mouse lungs (81). The technique yields accurate, quantitative information about the microstructure and geometry of acinar airways.

Diffusion of ^{3}He gas in lungs at the acinar level (over 90% of gas volume is within acini) is highly restricted by the alveolar and airway walls, which enables measurements of lung microstructure with established relationships between diffusion-attenuated MR signal and parameters characterizing the lung microstructure (81, 102, 121).

4.1 Lung Model

To extract the relationship between lung structure and gas diffusion, it is essential to apply a simplified lung model containing some basic geometric parameter to describe the real lung structure.

The airway system inside the lung is a dichotomous branching airway tree. For a human lung, there are 23 generations of dichotomous branching, with first 15 generations as conducting airways lined by a bronchial epithelium. Form the 15th generation, alveoli with gas exchange surface begin to be involved in the airway wall. After about three generations the airway wall is fully decorated with alveoli, which forms the so-called

alveolar duct. In the last generation, the alveolar sac is blind-ending. The anatomical unit distal to a terminal bronchiole is called the acinus (115). The structure of the acini is the microstructure we are interested in this study, which occupies about 95% of the total lung volume (118). The mouse lung structure is very similar to the human lung except that the mouse lung contains no respiratory bronchioles.

Since the fundamental organizational unit of the acinus is the alveolar duct or sac, the lung model we used also consists of a network of cylindrical airways covered with alveoli around as suggested in (91) and (36). This is schematically represented in **Figure 4.1**. The structure of an acinus in our lung model can be characterized by three geometrical parameters – outer radius *R*, inner radius *r*, and the effective alveolar diameter *L*. The alveolar depth *h* is defined to be the difference of *R* and *r*.

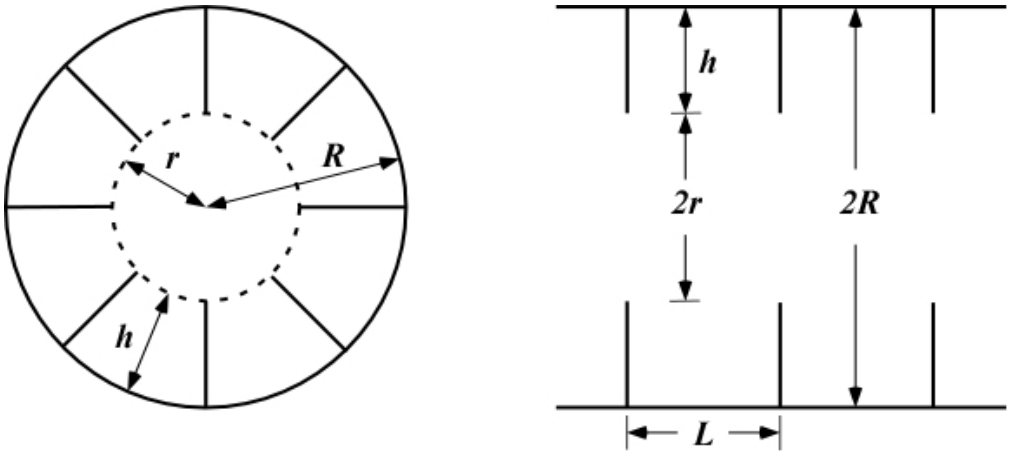

Figure 4.1: Schematic structure of the model of an acinar airway used for MRI, shown in 2-D perpendicular and parallel to the long axis of the airway.

4.2 MR Diffusion Imaging

As described in 3.2.3, a bipolar gradient is usually used in MRI to measure diffusion which is was initially devised for NMR by Stejskal and Tanner (101). In the case of free diffusion, the MR signal decay can be described by

$$S = S_0 \exp(-bD_0) \tag{4.1}$$

Here S_0 is the MR signal intensity in the absence of diffusion sensitizing gradients, b value is determined by the gradient waveform, and D_0 is the free diffusion confident. If the diffusion is restricted by barriers (e.g. lung airway wall), the MR signal can be described in terms of ADC:

$$S = S_0 \exp(-b\ ADC) \tag{4.2}$$

For the mouse experiments, we used the diffusion waveform as shown in **Figure 4.2**. This waveform is more realistic than the one shown in **Figure 3.3** because it is impossible for the hardware to ramp up or ramp down gradient with an infinite rate. For this diffusion gradient waveform,

$$b = (\gamma G_m)^2 \left[\delta^2 \left(\Delta - \frac{\delta}{3}\right) + \tau \left(\delta^2 - 2\Delta\delta + \Delta\tau - \frac{7}{6}\delta\tau + \frac{8}{15}\tau^2\right)\right] \tag{4.3}$$

where G_m is the gradient amplitude, Δ is the diffusion time (time between centers of positive and negative gradient pulses), δ is the total width of each pulse, and τ is the ramp time (120).

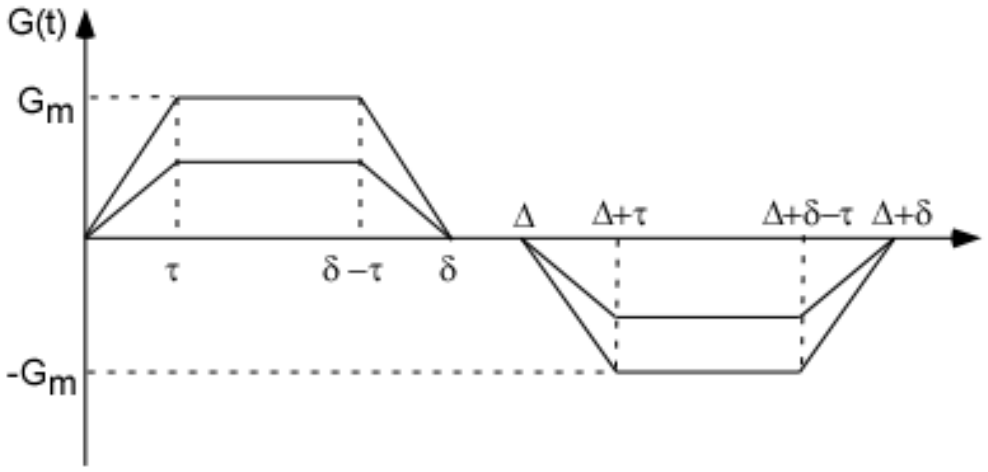

Figure 4.2: Diffusion sensitizing gradient waveform used in the mouse experiments. G_m is the maximum gradient amplitude, Δ is the diffusion time, δ is the pulse width, and τ is the ramp time.

For infinitely diluted ^{3}He in N_2 or air, D_0 = 0.88 cm^2/sec, which makes the characteristic free displacement $l_0 = \sqrt{2D_0\Delta} = 278$ μm for a diffusion time of 440 μs used in our pulse sequence. This length is much larger than the average alveolar diameter of ~ 60 μm (83), which means that during the diffusion time, the gas molecules can move out of alveoli and along the acinar airways. The mouse acinus size is about 670 μm compared to ~ 6 mm in human lung (94). One hypothesis of our theoretical model is that the ^{3}He molecules diffuse in one acinus during the time scale. This made us to choose the shortest possible diffusion time which is limited by the hardware to decrease the fraction of ^{3}He molecules of moving into adjoining airways. The diffusion time of 440 μs allowed most of the ^{3}He molecules move around in the same acinus.

Thinking of diffusion in our lung geometric model described in last section, the ^{3}He molecules will receive less restriction along the airway direction than the direction perpendicular to the airway. This diffusion anisotropy can be characterized by independent diffusion coefficients D_L and D_T, representing diffusion longitudinal and transverse to the airways respectively. If the angle between the principal axis of the airway and the magnetic field is α, the ADC can be presented as(17)

$$\mathrm{ADC}(\alpha) = \mathrm{D_L}\cos^2\alpha + \mathrm{D_T}\sin^2\alpha \tag{4.4}$$

Assume that there are a large number of airways in each imaging voxel, the orientation distribution of all the airways can be taken as uniform with distribution function $\mathrm{g}(\alpha) = \sin\alpha/2$. The MR signal of one imaging voxel is the sum of the signals over all the airways:

$$\begin{aligned} \mathrm{S} &= \mathrm{S_0}\int_0^{\pi} \mathrm{d}\alpha \frac{\sin\alpha}{2} \exp\left[-\mathrm{b}(\mathrm{D_L}\cos^2\alpha + \mathrm{D_T}\sin^2\alpha)\right] \\ &= S_0 \exp(-bD_T)\left(\frac{\pi}{4bD_{AN}}\right)^{1/2} \cdot \Phi\left[(bD_{AN})^{1/2}\right] \end{aligned} \tag{4.5}$$

where $D_{AN} = D_L - D_T$ is the diffusion anisotropy, and $\Phi(x)$ is the error function. Note that this is assumed that in one imaging voxel all the airways are with the same geometrical parameters. It is obvious that this decay is non-monoexponentia in b-value.

4.3 Relationship between Diffusion and Lung Microstructure

To extract the relationship between diffusion coefficients (D_L and D_T) and geometric parameters, Monte Carlo simulation with certain range of the geometric parameters and the timing of the diffusion gradients needs to be done. For mouse lung, the relationships

were obtained to be applicable for R = 60 - 140 μm and diffusion parameters Δ = δ = 0.3-0.6 ms (81);

$$D_L = D_{L0} \cdot (1 - \beta_L \cdot bD_{L0})$$

$$D_T = D_{T0} \cdot (1 + \beta_T \cdot bD_{T0}),$$

$$D_{L0} = D_0 \cdot exp[-2.99 \cdot v^{1.88}], \qquad v = 1 - \frac{r}{R}$$

$$\beta_L = 113.5 \cdot \left(\frac{R}{L_1}\right)^{1.5} \cdot exp\left[-\frac{5.11}{\sqrt{v}}\right]$$

$$D_{T0} = D_0 \cdot F(R) \cdot [1 + u(R,r)], \qquad F(R) = \frac{7}{16} \cdot x^{\left(4-3.63 \cdot x^{0.6}\right)},$$

$$x = \frac{R}{L_2}$$

$$u(R,r) = v^{1.75} \cdot exp(A \cdot v),$$

$$A = 1.1 + 3.14 \cdot x - 18.39 \cdot x^2,\ \beta_T = 0 \qquad (4.6)$$

where D_0 is the free diffusion coefficient of ^{3}He gas in lung air spaces, and

$$L_1 = (2 \cdot D_0 \cdot \Delta)^{1/2},\ L_2 = (4 \cdot D_0 \cdot \Delta)^{1/2} \qquad (4.7)$$

are the characteristic free-diffusion lengths for one- and two-dimensional diffusion, respectively.

The relationships in (4.6) are phenomenological and somewhat different from analogous relationships in human lungs to reflect the smaller size of mice airways; specific

mathematical functions are chosen purely to fit Monte-Carlo simulations, which were performed on diffusion attenuated MR signal for mouse lung (81 , 102).

Fitting the equations to multi-b measurements of the ^{3}He diffusion attenuated MRI signal in lung airways enables the extraction of geometrical parameter R and h via a straightforward fit using Bayesian probability theory (10, 86). Knowing these parameters and assuming eight alveoli per annular ring, we can estimate the alveolar surface area S_a, lung volume per alveolus V_a, and alveolar number density N_a (121). Then using the well-known relationship between mean linear intercept and surface-to-volume ratio (114), we can estimate the mean linear intercept, Lm:

$$S/V = S_a/V_a = 4/Lm \tag{4.8}$$

Chapter 5

Experimental Techniques

5.1 Animal Preparation

All experiments were approved by the Washington University Animal Studies Committee.

5.1.1 Anesthesia before Imaging

Before imaging, the mice were briefly anesthetized with a ketamine/xylazine mixture appropriate for mice (ketamine 87mg/kg and xylazine 13mg/kg intraperitoneally). The dose given each time allows sufficient time to intubate and attaching the animal on the ventilator in the MR scanner room.

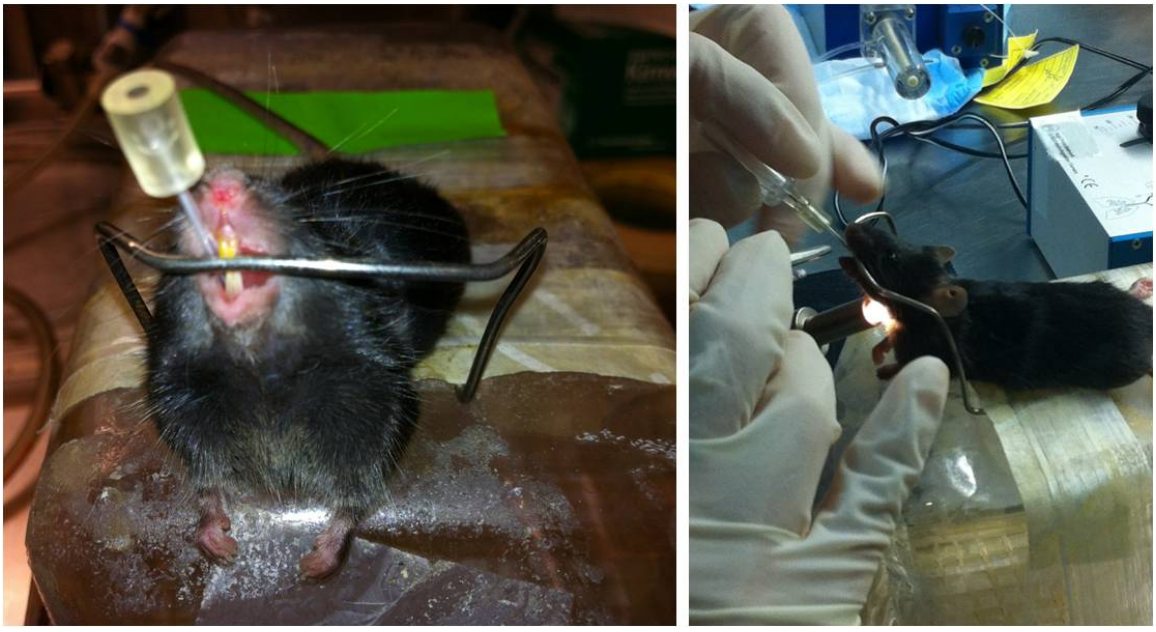

Figure 5.1: A mouse in the intubation process on our home-made intubation set-up

5.1.2 Intubation

During anesthesia, the mice undergo an intubation process for attaching to the ventilator. Intubation in this study refers to the process of inserting an intratracheal (I.V.) tube into the trachea (**Figure 5.1**). This is a non-surgical procedure which allows a full recovery of the animals after every imaging session. The tube can be easily pulled out from the animal after it is disconnected from the ventilator.

The I.V. tube used in this study was home-made by connecting the tubing part of a 20-gauge I.V. catheter (Kendall Monoject Veterinary, Tyco Healthcare, Mansfield, MA 02048) and a piece of 5mm long 1/16" ID Tygon hose (Figure 5.2).

Figure 5.2: Home-made Intubation tube

The success of intubation is critical for our study. This requires skilled assessment and performance. The I.V. tube we used is 20-gauge which is determined based on our experiences, for ease of intubation and a relatively snug fit for pressure control.

Petroleum jelly is not used in our study to coat the outside of the tube; it is often used as a lubricant during intubation which may provide a better seal between the trachea and the tube. Our concern here is that the petroleum jelly may easily come off the tube and stay in the trachea; since mice have very poor or no cough reflex they may have trouble coughing the material out, which may lead to breathing problems later on. Moreover, the breathing pattern we observed during each imaging session indicated a good seal between the tube and the trachea without using petroleum jelly.

After intubation, the mouse is connected first to a commercial ventilator (HSE-HA MiniVent Mouse Ventilator, Harvard Apparatus) (**Figure 5.3**). This ventilator is not MR and HP gas compatible so it is situated outside the scanner room. The success of the intubation can be verified by seeing the mouse chest (not the stomach) moving at the exact respiration rate of the value set on the ventilator. Then the animal is ready to be disconnected and moved to the home-built ventilator in the scanner room.

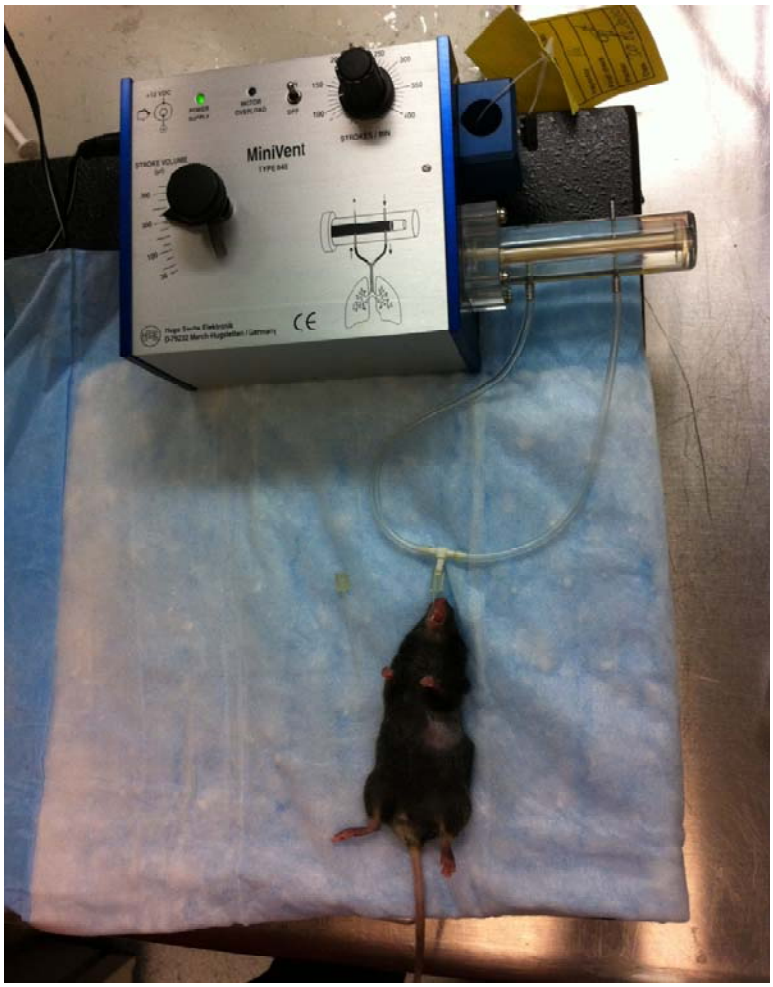

Figure 5.3: Verification of a successful intubation by observing the ventilation performance of a mouse after connected to a commercial ventilator which is not MR compatible.

5.1.3 Attaching Animal to Ventilator

After intubation, the mouse is placed on the commercial ventilator MiniVent to make sure that the intubation tube is in the right position and the mouse can breathe smoothly on the ventilator. Then with the mouse still attached to the MiniVent, the RF coil is slid

onto the animal from the tail and centered on the moving chest area. The animal with the intubation tube in the trachea was disconnected from the MiniVent and moved directly onto the custom-built ventilator in the scanner room.

The outlet of the breathing valve system on our ventilator is a barb fitting which can be fitted into the 1/16" ID Tygon hose on our intubation tube. The animal was attached supine to the custom-built ventilator. The isoflurane vaporizer needs to be turned to ~2% to keep the mouse anesthetized during the entire imaging process.

5.1.4 Breathing Pattern

In our study, the mouse is usually ventilated at 120 breaths per minute with 0.25-mL tidal volume.

This respiration curve is measured by a pressure transducer (Honeywell, Model No. 24PCAFA6D) connected to the breathing valve system and used to monitor pressure of the gas supplied during ventilation. The peak airway pressure of our standard is 15 cm H_2O which corresponds to 1000mV shown on the oscilloscope connected to the pressure transducer.

Figure 5.4 shows a representation of a typical respiration curve (pressure waveform) of one breath used in our imaging. Each breathing cycle consisted of pure O_2 delivered in the first half and $^3He/N_2$ gas mixture in the second half of inspiration separated by a 22.5-ms breath hold, followed by a brief breath hold (~35 ms) for image acquisition and then passive exhalation. Note that the pure oxygen constituted around 1/3 of the total gas of each breath, which is slightly higher than the oxygen content of air (21%).

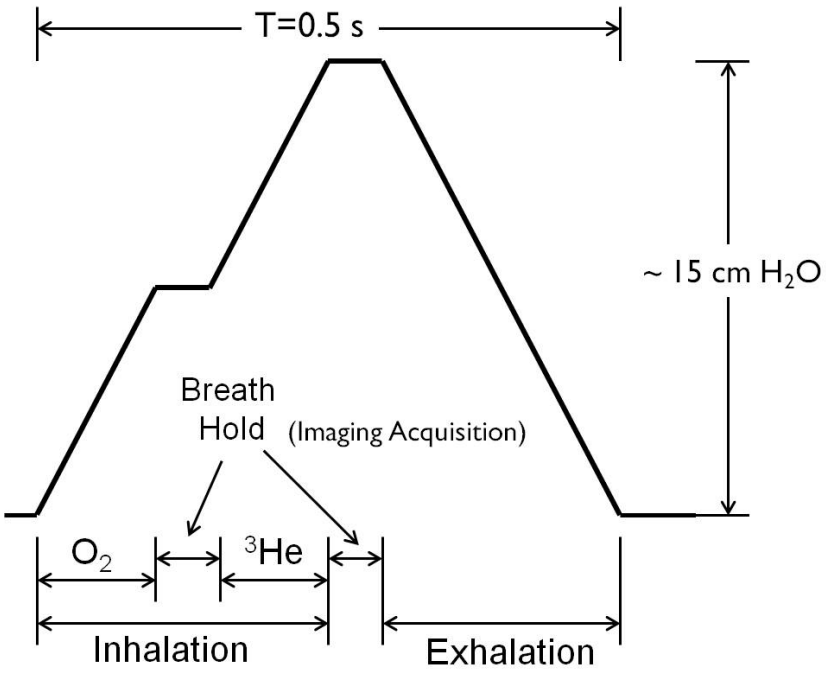

Figure 5.4: Schematic of the typical mouse breathing pattern measured from a pressure transducer at the mouse trachea. In each breathing cycle of 0.5 s, O_2 is delivered in the first half of inspiration and 3He delivered in the second half followed by data acquisition during a breath hold; after breath hold, the vent valve opens to allow passive exhalation of the animal.

5.1.5 Ventilator Parameters

On the electronic controller of the ventilator, three pairs of potentiometers (each pair is corresponded to "start" and "stop") were used to control the time of delivering O_2, ^3He and venting during one breathing cycle. Another pair of potentiometers was used for specify the "start" and the "stop" of the triggering. In our typical setting, the "stop" for trigger was connected to the "stop" for the vent which is the end of one respiratory cycle.

Note that since the hose to transfer air and vacuum pulse from electromechanical control system to the breathing valve is about 1 meter long, there is a delay for the real pressure change compared to the nominal value on the potentiometer.

To achieve the breathing patter in **Figure 5.4**, the timing parameters we used were listed in **Table 5-1**.

Solenoids	Start (%)	Stop (%)
O_2 control	0	22
^{3}He control	26.5	50
Vent control	57	100

Table 5-1: The timing parameters used on the electronic controller in a typical mouse imaging experiment

On the electromechanical system, the air pressure used for the three solenoid controls (O_2, ^{3}He, Vent) is 6~8 psig, and the vacuum is 5~6 in Hg. The pressure for O_2 supply is 2~3 psig. The pressure for N_2 line (^{3}He supply) is 2.5~3 psig. The average gas flow we used was around 30 cc/min, calculated by using the tidal volume (0.25 cc) and the respiratory rate (2 breaths/s). This corresponds to the addition of O_2 and ^{3}He gas flow. In real experiments, the flow restrictor needs to be changed sometimes with the pressure regulator to achieve the desired pressure waveform.

5.1.6 Considerations for the Animal Ventilator in Experiment

A well functioned animal ventilator is essential to acquire high quality MR images for morphometry and decrease the mouse mortality rate.

The electromechanical control system needs to be located more than 1.5 meter away from the magnet. Otherwise, the solenoid valves on it may not function normally. The control

pressure of the air pulse from the solenoid valves needs to be greater than the pressure for O_2 and ^3He supply in order to fully close the diaphragms in the breathing valves during the time designed to be closed. Conversely, the vacuum needs not to be that strong to open the diaphragm valve because the gas supply can push its way through even if there is no pressure applied on the other side. The vacuum control makes the valves function more precisely in the sense of timing.

For designing the breathing pattern, the O_2 supply and ^3He supply need to be separated by a brief breath hold. As is known, the ^3He polarization will be destroyed in seconds in the presence of O_2. Separating the two gas delivery can avoid O_2 flowing back into the ^3He supply line which will cause the depolarization of the whole bag of ^3He gas in a very short period of time. In our setup, the mixing of ^3He and O_2 is only possible in the dead volume within the breathing valve system and the animal's lung. There will not be significant loss of magnetization in ~250 ms with low oxygen concentration.

The permeability of the whole system can be verified by checking the pressure curve shape during the breath-hold period. A small plateau should be observed during that period of breath hold in the pressure waveform, which indicates a good seal between the intratracheal tube and trachea as well as the gas delivery system.

For ^3He gas supply reservoir, when filling ^3He gas into the Tedlar bag, the lid of the big bottle (the reservoir) needs to be open. This will prevent the pressure in the Tedlar bag getting too high to release to the animal through breathing valves. However, this may cause the gas supply pressure to be very low at the very beginning and the imaging needs to wait for the pressure to build up and stabilized at a normal level to start. In a HP gas

experiment, this wait time will lead to the polarization loss. A solution to this problem is to temporarily increase the supply pressure and flow of ^{3}He gas after the filling of the HP gas to let the pressure rise to the normal level as quickly as possible. As long as the normal level is achieved, the pressure and flow for ^{3}He can be adjusted again to maintain the normal pressure waveform.

Another important issue is the position of the intubation tube in the trachea. When attaching mice onto the ventilator careful precautions needs to be taken to ensure that the intubation tube does not stick too far or too shallow in the trachea. If it is too far, the tube may push directly toward some tissue wall, the pressure shown on the oscilloscope may appear to be very high or normal but the lung will not get well ventilated in this case. If it is too shallow, the tube will fall out very easily.

It is also important to keep the mouse warm during the imaging. We have a hot-water circulating system in the scanner room which can provide hot water flowing though a long tube. The tube is wrapped around to form a pad and directly attached to the animal's holder. Warm air was also available for use to circulate inside the magnet bore to maintain body temperature of mice.

5.2 ^{3}He Polarization and Gas Preparation

^{3}He gas used in our experiment was hyperpolarized with two home-built polarizers or a commercial polarizer (General Electric/Amersham Health) using spin-exchange optical pumping (Section 3.1.2).

The 400 cc of HP gas with a polarization level ~40% was released to a 1-L Tedlar bag and then diluted with the same amount of N_2. One bag of this mixture could continuously supply hyperpolarized ^{3}He gas to a mouse for approximately 30 min.

For the GE polarizer, the HP gas can be directly released to the Tedlar bag in the gas reservoir. Note that before the release of the HP gas, the Tedlar bag needs to be purged several times using N_2 and vacuum lines on the machine. The reservoir bottle will be transferred to the scanner room and connected to the ventilator as soon as possible. The time from the gas release from the GE polarizer to the supply on the ventilator is less than 3 minute, which does not cause significant magnetization loss.

For the gas polarized by the home-built polarizer, it needs to be transported about 3 miles from the polarizer in a physics lab to the medical school. We used a specially built case to store the glass cell of HP gas. In the case, there is a solenoid powered by a rechargeable battery which can generate a magnetic field of 25 Gauss (a shield to the earth's 0.5 gauss field). There is not significant magnetization loss observed by this transport process(66). There is a gas fill system mounted on the side of electromechanical control system. The system utilizes the same N_2 and vacuum lines as in the electromechanical control system to purge the Tedlar bag. There is another line connecting the Tedlar bag and the glass cell of HP gas. Because the HP gas pressure in the cell is as high as 10 atm, we put a restrictor along this line to get more control of the gas release. With this setup, one full cell (~50 mm^3) of HP gas can be used for 2~4 consecutive mouse experiments.

5.3 Image Acquisition

The MR imaging of the validation study with healthy mice was performed on an Oxford Instruments (Oxford, UK) 4.7 T horizontal-bore magnet (Howard, 33-cm magnet bore

and 15-cm gradient bore) equipped with actively shielded, high-performance Varian/Magnex gradient coils. All the other MR imaging was performed on a Varian 4.7 T horizontal-bore magnet (SIS 330, 40-cm magnet bore and 12-cm gradient bore).

A custom-built doubly resonant solenoid coil tuned to both ^{3}He and ^{1}H frequencies (151.1MHz and 198.3 MHz, respectively) was used. The coil was placed perpendicular to the magnet field direction. As a result, the bore size is a limitation for the placement of the animal. In most cases, the tail of the mouse needed to be fixed sideways by tape in order to fit the animal length into the bore.

5.3.1 ^{1}H MRI of the Lung

A standard 2D multi-slice gradient-echo sequence was used for ^{1}H MR imaging. One of the main purposes of ^{1}H MRI is anatomical orientation. In a Varian system, a quick ^{1}H scout image is taken at the very beginning of every study. The scout protocol acquires imaging slices in each of the three cardinal planes in order: axial, coronal, and sagittal (these plane directions are defined as fixed relative to the magnet, See **Figure 5.5** and **Table 5-2**). These nine images provide the information about the approximate location of the imaging object, which will serve as reference images for planning the imaging slices we really need. In our study, we use scout images to interactively plan for the following imaging with 5~9 slices in the sagittal plane. Because of the RF coil we use, the mouse (and the coil) is placed along x direction (x: left-right direction). This means that the "sagittal" plane of the Varian system is actually the axial plane of the mouse in our experiments. The scout scan takes only a few seconds.

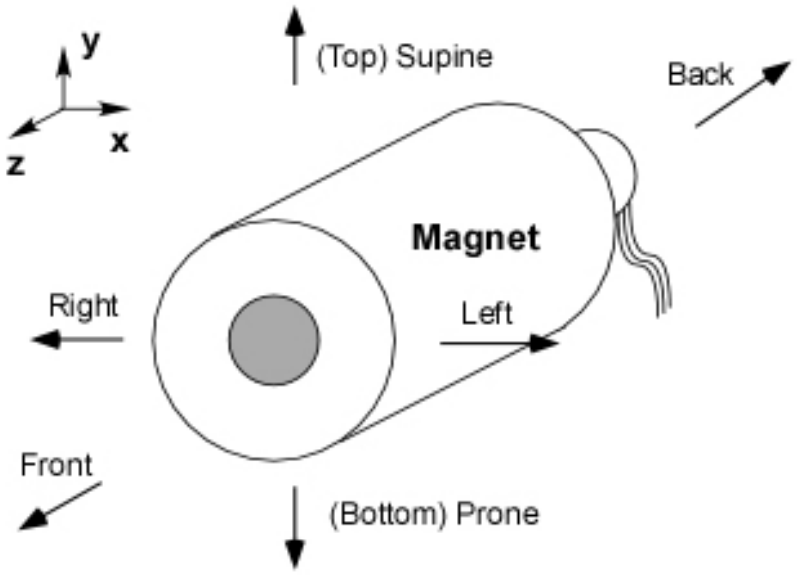

Figure 5.5: Laboratory coordinates of a horizontal-bore magnet in a Varian system

Orientation	Read Out	Phase Encode	Slice Select
Axial	y	x	z
Coronal	z	x	y
Sagittal	z	y	x

Table 5-2: Definition of read-out, phase-encode, slice-select direction in a Varian system

Besides quick low-quality ^{1}H MR scans for anatomical orientation, high-resolution gated ^{1}H MRI was also routinely conducted. The imaging parameters are: during breath-hold time, one line of k space for all the imaging slices were acquired during 17.95 ms, echo time TE = 0.99 ms, flip angle = 50°, pixel size = 312.5 μm × 312.5 μm, slice thickness = 2mm.

Since the T_2^* in C57BL/6 mouse lung is ~0.46 ms(80), with TE= 0.99 ms, we still cannot get enough SNR to image the lung parenchyma. But this sequence is good to detect the inflammation in lungs. The inflammation areas are shown as bright signals compared to the normal lung parenchyma area. Moreover, it allows a precise volume measurement because of the good contrast between thorax cavity and tissue around it. These two points will be discussed in details in the next chapter.

5.3.2 ^{3}He Diffusion MRI

To collect ^{3}He diffusion MRI data we used a 2D multi-slice gradient-echo sequence with embedded bipolar diffusion-sensitizing gradients (see details in (120)) .

Six b values of 0, 1, 2, 4, 6, 9 s/cm^2 are generally used in our study. In the initial test, we compared 10-b value diffusion measurement (b=0, 1, 2, 3, 4, 5, 6, 7, 8, 9, 10 s/cm^2) with the 6-b value ones on the same mice to test the reliability and robustness of theoretical fitting. No differences were seen between results of 6- and 10-b-value experiments, which make 6-b measurement our standard.

The imaging parameters were: at peak inspiration of each breath one line of k space at one b value for all 5 slices were acquired during 21.6 ms, TE = 2.44 ms; pixel size = 625 μm × 625 μm, matrix size = 64×64 for FOV = 40 mm×40 mm or matrix size = 48×48 for FOV = 30 mm×30 mm, slice thickness = 2 mm and five axial slice nearly covering the entire lung from the apex to the basal.

Since each new breath supplied fresh HP ^{3}He gas, we used large flip-angle RF pulses (70°). Theoretically, our method of scanning k-space should allow using 90° pulse, which

would leave no residual magnetization at all. However, previous test acquisitions using different flip angles (50°, 70°, 80°, 90° etc.) showed that the S/N in images acquired with a 70° pulse was better than the corresponding images acquired with a 90° pulse. This may due to effects from the shape of the RF pulses. The RF pulses we applied are Gaussian in shape and, therefore, have a Gaussian slice selection frequency profile. This implies that there is some "bleeding" of magnetization between adjacent slices when imaging since an RF pulse delivered to one slice will partially affect spins in the adjacent slices. Obtaining an approximately square frequency excitation so that slices are completely independent would require a sinc pulse. However, a sinc pulse needs to be much longer than the corresponding Gaussian pulse to cause the same flip angle excitation when keeping the RF power constant. Considering the short T_2^* of HP ^{3}He in the mouse lungs, there will be more signal attenuation from the longer slice-select gradient. It is advantageous to keep the RF pulses as short as possible.

For the diffusion sensitizing gradients, we use length of each lobe δ = 440 μsec, rise time τ = 150 μsec, and no gap between the two lobes [$\Delta = \delta$], gradients along read out direction. These timing parameters of the diffusion sensitizing gradients were consistent with the parameters used in the theoretical simulation (82), which were selected to minimize effects of ^{3}He gas diffusing into neighboring acinar airways during diffusion measurements. The diffusion gradient strength G can be calculated by

$$G = b^{\frac{1}{2}}\gamma^{-1}\left[\delta^2\left(\Delta - \frac{\delta}{3}\right) + \tau\left(\delta^2 - 2\Delta\delta + \Delta\tau - \frac{7\delta\tau}{6} + \frac{8\tau^2}{15}\right)\right]^{-\frac{1}{2}} \qquad (5.1)$$

With the timing parameter above,

$$G \approx 9.29\, b^{\frac{1}{2}} \text{ (gauss/cm)} \tag{5.2}$$

The maximum gradient is 60 gauss/cm for SIS 330 and 45 gauss/cm for Howard (located in Compton Lab). By using the maximum b value of 9, the maximum diffusion gradient we require is 27.87 gauss/cm. For a ramp time $\tau = 0.15$ ms , the maximum gradient can be achieved is 33.33 gauss/cm and 33.75 gauss/cm for Howard, which are both well beyond what we asked for.

5.3.3 Scanning k Space

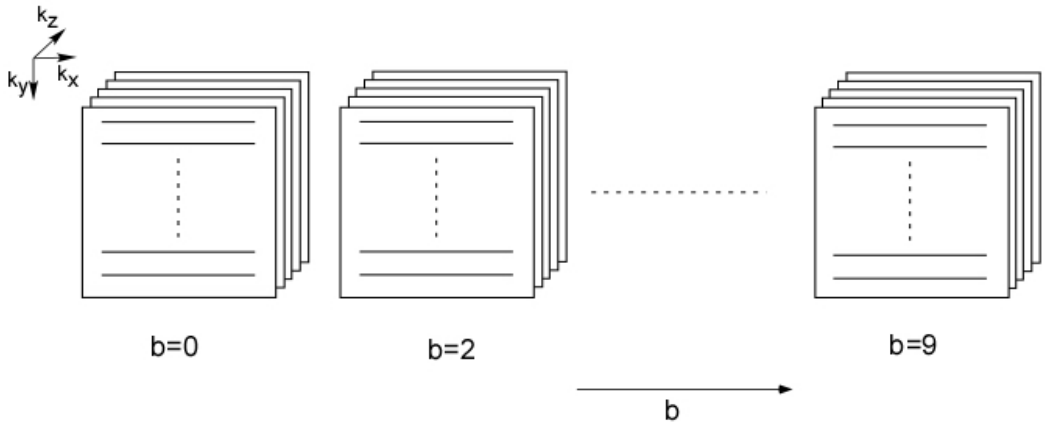

Figure 5.6: Interleaved Scheme of k space coverage. b value is incremented before moving along on the phase encode direction.

For diffusion weighted imaging, one line of k space (along k_x direction) at one *b*-value was scanned for all five slices on each breath; the 5 subsequent b-values were scanned in the next 5 breaths, then k_y was incremented (**Figure 5.6**). This interleaved scheme eliminates nearly all T_1 effects on signal attenuation in the diffusion measurements. We

acquired images such that k = 0 was in the middle of the acquisition, so any residual k-space filtering from our long but finite T_1 effect was minimized.

5.3.4 The Direction of Diffusion Gradients

To test the macroscopic isotropy of the typical voxel, we also acquired images with diffusion sensitizing gradients in three spatially orthogonal directions separately, and also at lower resolution (1.25 x 1.25 x 4 mm). If the voxel is isotropic, there should be little difference between the parameters extracted from different sets of images.

The results showed that the differences between parameters *R*, *h* and *Lm* from the 3 different axis measurements were all less than 5%, as was the difference between resolutions. So for all our studies, diffusion gradients were applied along readout direction.

5.4 Data Analysis

5.4.1 Volume Measurement

The lung volumes were estimated both from the ^{1}H images and the ^{3}He ventilation images.

For ^{3}He images, the MRI signal voxels above the threshold which were set to ten times the value of noise were counted to segment the lung from background.

For ^{1}H images, lung parenchyma was segmented by counting all connected voxels in the thoracic cavity, minus the heart and large vessels. The trachea and major bronchi were manually removed in both methods.

One limitation of this volume measurement was the fact that in a few cases the most cranial or caudal parts of the lung were not included in the image and this will cause an underestimation of the total lung volume.

5.4.2 Bayesian Analysis

6-b diffusion weighted MR data from the Varian scanner were saved in two different formats: one is FID format which stores the raw FID data, and the other is flexible data format (FDF) which is the image data with an ASCII header (txt). Both of these files can be converted to a single column txt files by a MATLAB program, which can be imported into the Bayesian analysis interface. Note this step may be skipped because in the newer version of the Bayesian interface, there is an option to import the original data formats coming from Varian systems. The other file that needs to be import is a single column txt file containing the 6-b values, which is called "Abscissa" in the Bayesian analysis. Note that the first number in our "Abscissa" should not be zero but a very small positive number, e.g. 0.00001.

The theoretical equations also contain the ^{3}He free diffusion coefficient D_0 which depends on the gas concentration; we note, however, that the fitting results are not very sensitive to the value of D_0. To measure D_0, we ventilated a balloon using the same ventilation setup and imaging sequence, and compared this value to a calculated value. For the gas mixture supply of ^{4}He and ^{3}He, D_0 used is 1.3 cm^2/s and for the gas mixture supply of N_2 and ^{3}He, D_0 is 1 cm^2/s.

The package we used on the Bayesian analysis interface is "Analyze image pixel". After the package is selected, the theoretical model that the data is going to fit for can be loaded. The prior ranges of various parameters, R and v (=h/R) in our case, can be edited. Then

the model is ready to build (compile to verify that the subroutine in the theoretical model is written correctly.).

The fitting of imaging pixels to the theoretical equations was performed on a voxel-by-voxel basis. In the upper panel, the noise threshold can be assigned manually in order to exclude the pixels that are noise and not worth fitting for. In our analysis, the pixels outside the lung area in ^{3}He MR images need to be excluded by using this threshold value as many as possible. This will expedite the fitting process by fitting only the pixel having lung microstructure information. It is noteworthy that the threshold should not be set too high to eliminate the ventilated pixels in the lung.

Bayesian analysis interface will generates parametric maps including alveolar depth h, airway radii R and the mean linear intercept (Lm). Maps of the root mean square residue were also generated as one indicator of fitting quality.

5.4.3 Data Processing with Bayesian Analysis Results

All the maps generated by Bayesian analysis are 4dfp format. One 4dfp image consists of multiple binary images that are stacked by slice and element number. A MATLAB GUI interface was developed that allows reading of the 4dfp maps generated by Bayesian Analysis interface, displaying the individual map files and saving them in a variety of formats. At the same time, the mean, standard deviation, and histogram of various parameters can be output in a spreadsheet. Another feature of this MATLAB program is data analysis with interactive ROI selection.

Total alveolar number is the product of N_a and the lung volume measured by ^{1}H images. Total alveolar surface area was calculated by multiplying surface-to-volume ratio by the lung volume.

Standard one-way analysis of variance tests were used to compare results among groups. A *p*-value of less than 0.05 was considered significant for the comparison.

5.5 Quantitative Histology

All the histology work in this study was done by Dr. Nguyet Nguyen from Pulmonary in School of Medicine, Washington University. After imaging was completed, mice were sacrificed by asphyxiation with CO_2 and were exsanguinated by transection of the abdominal aorta. The thorax was entered via the diaphragm and the anterior chest wall removed. The trachea was cannulated with an 18-gauge I.V. catheter and 4% paraformaldehyde was instilled into the lungs at 15 cm water pressure. This pressure was chosen to approximate the pressure administered by the custom ventilator during imaging. Lungs were inflation-fixed for a minimum of 15 minutes, subsequently removed en bloc from the thorax, and immersed in 40-50 mL of fixative overnight. Following fixation, lungs underwent two sequential 15-minute rinses in PBS. Tissues were then embedded in 4% agarose (BP1423, Fisher Scientific, Houston, TX) in distilled water. The agar block was placed into a custom cutting device with an integrated micrometer that allows precise movement of the stage; 2-3 mm agar sub-blocks were cut from the agar block with a fresh microtome blade. Sub-blocks were placed with cut surface next to a ruler, and photographs were taken with the ruler in the field, pre- and post-processing, to determine the amount of tissue shrinkage due to processing.

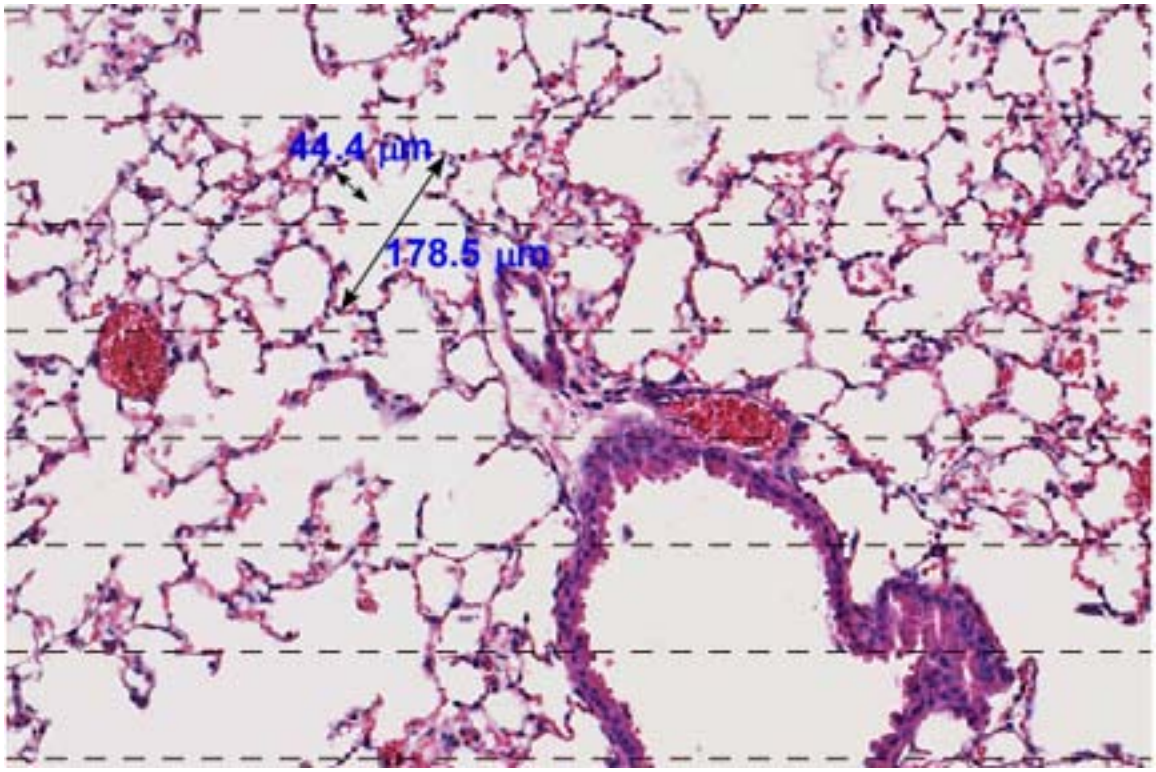

Figure 5.7: Example of a histological slide overlaid by a sampling grid, for microscopic measurement of chord length. In this case the morphometric parameters *R* and *h* are depicted (see arrows and marked dimensions) in one alveolar duct, which is approximately perpendicular to the slide.

Tissue sections 5 µm thick were cut and stained with hematoxylin and eosin, and images of each entire slide were captured on a Nanozoomer virtual microscope (Hamamatsu Corporation, Bridgewater, NJ). Chord length was determined using the public domain NIH Image 1.63 program (4). Fields with large airways and blood vessels were excluded. The chord length subroutine draws separate horizontal and vertical reference grids and then calculates the length of line segments created by the intersection of these grids with the tissue walls (Figure 5.7). For each set of lungs, at least 10 images per sub-block were analyzed; this represents > 30-50 images acquired from sections that were at least 2 mm

apart for each mouse and spanned 10-12 mm. Each sub-block was at approximately the same slice position and orientation as ^{3}He MR images.

Chapter 6

Results from Healthy Mice

In-vivo ^{3}He morphometric study of mouse lung was initiated by the validation of the technique in healthy mice. We implemented ^{3}He lung morphometry to quantify regional lung microstructure in seven 12-week-old healthy female C57 mice *in vivo*, with subsequent validation against direct quantitative histology.

6.1 Image Quality

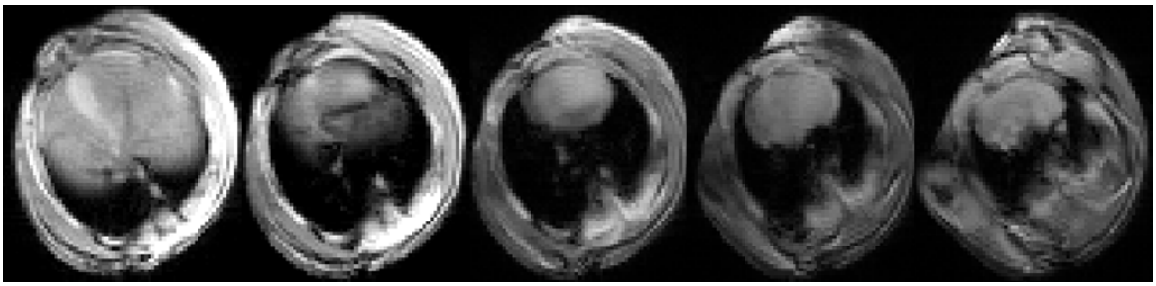

Figure 6-1: ^{1}He MR images of a healthy mouse. Due to the very short T_2^* in lung parenchyma, there is nearly no signal in the lung region. These images are used for anatomical orientation.

^{1}H images were acquired first to provide anatomical orientation (**Figure 6-1**). The ^{3}He diffusion MR images were generated at the exact same slice positions as those of ^{1}H images. A representative set of ^{3}He diffusion images was shown in **Figure 6-2**. The signal-to-noise ratio (SNR) for ^{3}He MR images ranged from 60 (for b = 9, standard deviation ~ 12) to 170 (for b = 0, standard deviation ~ 24). Breath-to-breath stability was

high, judging both from the consistent pressure waveform and the lack of effective motion artifacts in the phase encoding direction.

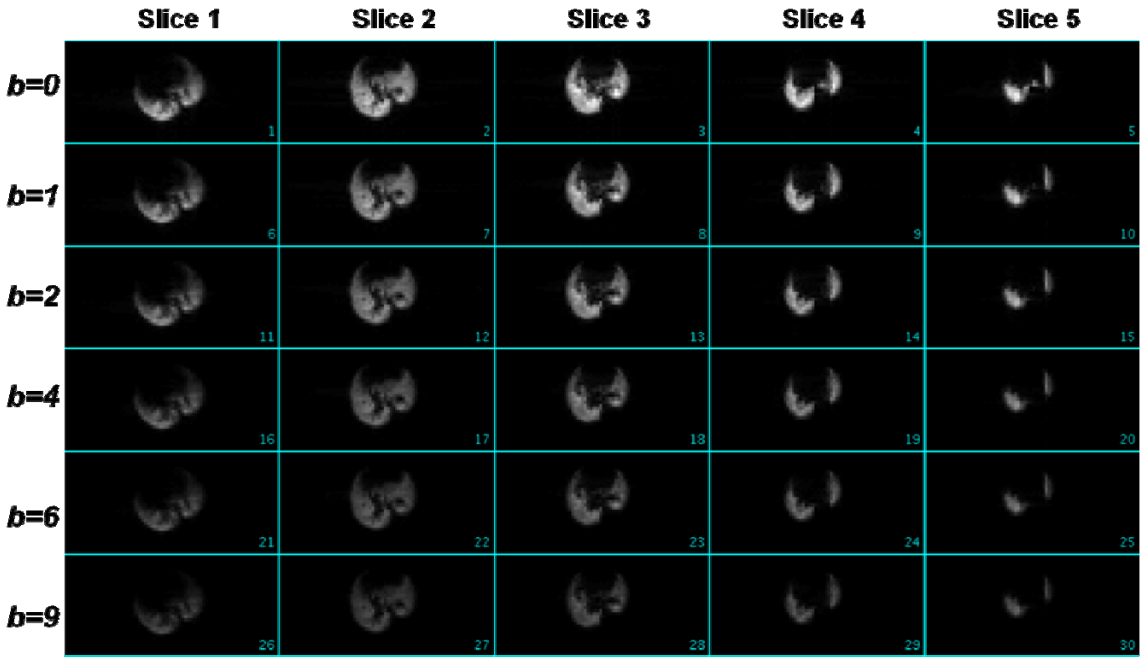

Figure 6-2: 6-b diffusion weighed 3He MR images of a healthy mouse lung. Five axial slices covers from base to apex of the lung

6.2 Fitting Quality

The fitting by Bayesian analysis was excellent in each case and the root mean squares (RMS) of the residues were all below 3% of the RMS of the original signals. A typical fitting of a single pixel is shown in **Figure 6-3**.

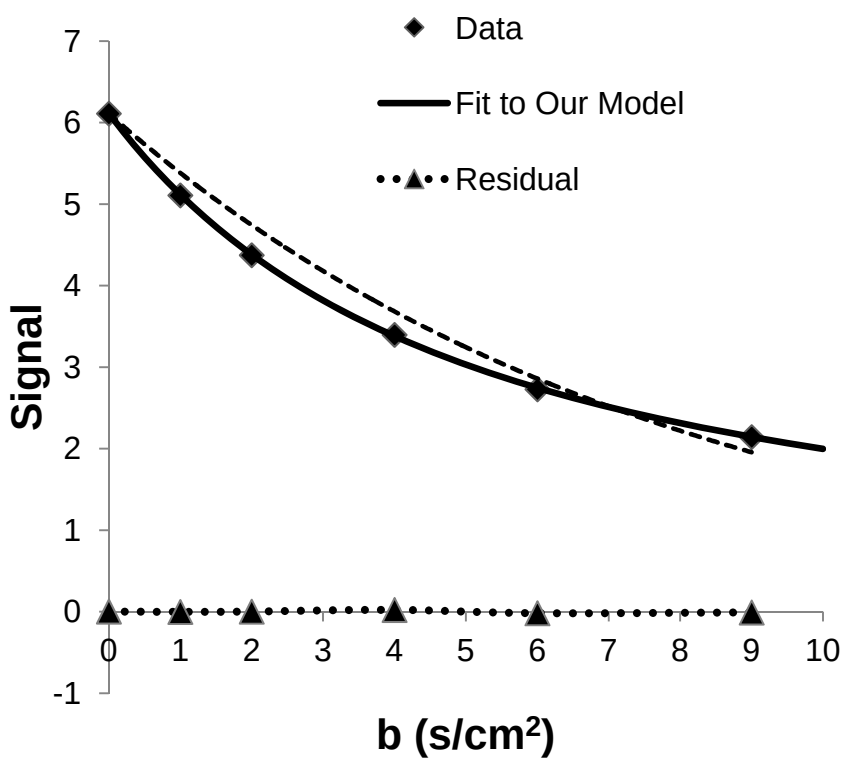

Figure 6-3: A typical fit of one pixel's MR signal (data are diamonds) to the mouse lung model described in the Theory section. The data show an excellent fit with the mouse model developed here (solid line) with significant deviation from mono-exponential behavior (dotted line). The triangles are the residuals between the mouse model and the data.

6.3 Morphometric Parameters

Figure 6-4 shows some representative parameter maps obtained from one mouse. We note that the parameters *R, h, Lm,* N_a, and *S/V* (Na and S/V are only listed in **Table 6-1**) characterizing mouse lung microstructure are all fairly homogeneous throughout the entire lung, though some regional variation is seen, with slightly increased *R* and *Lm* in the lung periphery. There is minimal variation in average values from slice to slice in the same mouse, implying little to no apical to basal dependence.

Individual morphometric data from imaging are summarized in Table 1. For the seven normal mice we studied, the mean acinar airway outer radius R was 97.2 ± 3.7 μm; the mean alveolar sleeve depth h was 51.7 ± 3.2 μm. The mean value of the mean linear intercept, Lm, calculated from R and h, was 60.5 ± 3.5 μm. The mean alveolar number density N_a was 3841.3 ± 316.5 mm^{-3}, and the mean surface-to-volume ratio was 698.1 ± 37.0 cm^{-1}. Slightly higher standard deviations per slice per animal (~10% for R, ~7% for h, ~18% for Lm) likely reflect true spatial variation in these volumes; in particular, there were slightly elevated values in the lung periphery (**Figure 6-4**), as validated by histological comparison.

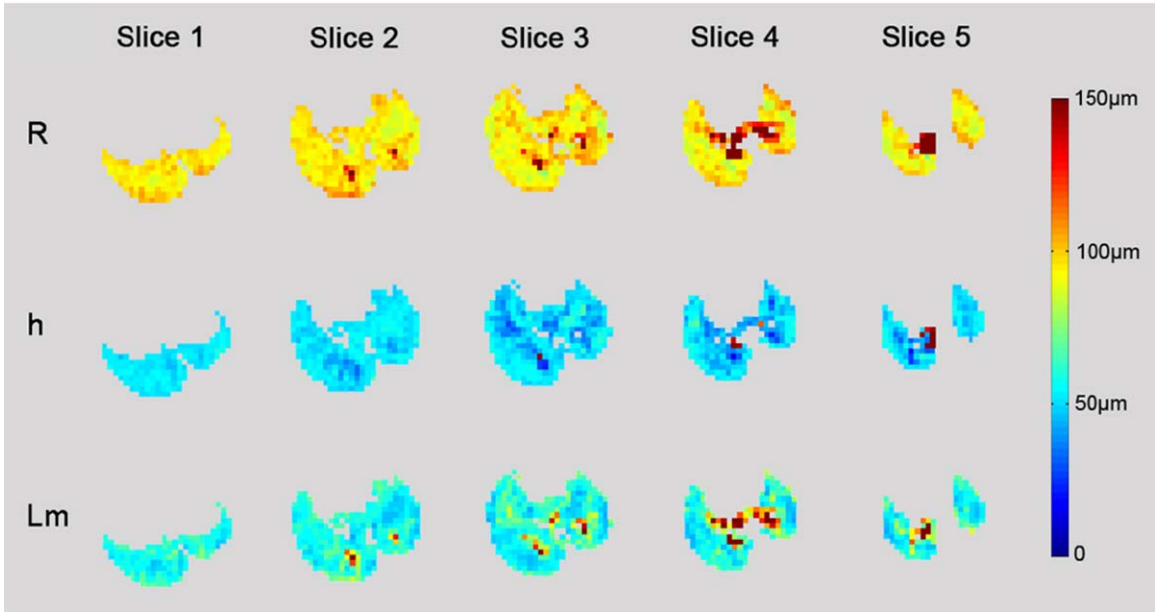

Figure 6-4: Representative geometric parameter (R, h, Lm) maps obtained from one normal mouse lung. Major airways are red in the maps of R. The pixel size is 0.63 mm × 0.63 mm and slice thickness is 2 mm.

Mouse No.	*R* (μm)	*h* (μm)	*Lm* (μm)	N_a (mm^{-3})	*S/V* (cm^{-1})	Lm(Histology)
1	95.6±7.0	49.8±6.7	61.0±12.5	3920±829	702±88.6	54.5±5.0
2	100.4±6.4	49.2±4.4	66.0±10.2	3360±632	642±69.1	52.8±5.6
3	97.4±7.9	49.3±6.3	62.4±13.1	3760±854	689±86.7	49.6±5.6
4	94.7±6.7	51.3±5.9	58.7±11.6	4020±784	722±87.9	52.7±4.5
5	92.0±6.4	52.9±3.6	54.6±10.1	4390±871	762±105.0	50.6±3.4
6	103.3±5.8	58.3±3.9	60.1±8.8	3680±536	682±70.2	-
7	96.7±5.9	51.4±4.2	60.1±8.4	3760±670	688±82.4	-
Mean	97.2	51.7	60.5	3840	698	52.0
Std Dev	3.7	3.2	3.5	320	37	1.9

Table 6-1: Summary of morphometric parameters obtained via ^{3}He MRI from 7 normal mice with histological comparison (not available for mice 6 and 7). The table gives values of key parameters in our model: acinar airway radius *R*, alveolar depth h, mean linear intercept *Lm*, alveolar density Na and alveolar surface-to-volume ratio *S/V*. Since there is not much variation from slice to slice in the same mouse, only mean values of the parameters for each mouse are shown here.

6.4 Validation against Histology

Table 6-1 also shows the data of mean chord length measured by histology and ^{3}He-based measurements of *Lm*. The average *Lm* measured by histology is 52.4 μm, compared to 60 μm, the average of *Lm* measured by ^{3}He MRI; small standard deviations are seen in each data set.

Comparison between histological measurements of chord length and ^{3}He-based measurements of *Lm* demonstrates a reasonable agreement between the two methods. There is a systematic difference (small but statistically significant), with the ^{3}He MRI method consistently yielding greater values of *Lm* compared to histology. Our MRI-based measurement is based on the model that assumes a specific, geometric airway structure while the histology is not. Slightly folded or undulating alveolar walls, for example, would contribute to a lower histologically-determined *Lm*. Another potential systematic difference is the level of lung inflation. While we attempted to fix the lung for morphometry at very similar pressures as used for MR imaging, inflation with liquid after removal from the thoracic cavity is simply different from *in-vivo* gas inflation and can lead to systematic differences in the level of apparent lung inflation.

6.5 Comparison to Other Literatures

Our morphometric data of healthy mouse lung are in good agreement with previously reported data in mouse lungs *ex vivo* (81).

Lm of healthy mice reported in other studies ranged from 44 μm to 63 μm (100). Parameswaran et al. measured the alveolar airspace volumes in *ex-vivo* mouse lungs fixed at 30 cm H_2O using micro-CT (83). The mean alveolar airspace diameter they reported for 10-week-old normal C57 mice is 59 μm; their diameter, defined by a sphere, should be approximately the same or slightly larger than our parameter of the alveolar sleeve depth, *h*.

Our results for N_a can be compared with estimation of alveolar number by Fehrenbach et al. (25) with a stereologic approach in 6 healthy C57BL mice. Their average N_a was

2643/mm^3, the same order of magnitude as our MR-based measurements, which ranged from 3364 to 3963/mm^3. Recent measurements of *S/V* by different groups (58-60, 72, 74, 106) varied between 500 and 1000 cm^{-1}. Our measurements (*S/V* ~ 642.0-761.9 cm^{-1}) are in good agreement with these results.

Chapter 7
Results from Mouse Models of COPD

The fact that we can accurately measure lung morphometric parameters *in vivo* demonstrates the potential for implementation of this technique in a variety of mouse models of disease. The ability to spatially localize disease via an imaging method and follow individual animals longitudinally is an advantage in time, accuracy, and reduced number of animals involved in a study. Our technique is particularly useful for early or mild disease, when diffusion anisotropy is still high. With severe tissue destruction associated with more severe emphysema, cylindrical geometry will be less accurate, and this will be reflected in lower diffusion anisotropy. In those severe cases, the simple ADC may prove to be just as sensitive. Here we presented ^{3}He morphometry application in several mouse models of COPD in which this technique was proven to be a precise, noninvasive, in vivo biomarker of changes in lung microstructure of lung diseases.

7.1 Elastase Mouse Model

Emphysema was induced by intratracheal administration of elastase (1-10 units) in 12-week-old C57BL/6 mice (n = 4) and lungs were imaged 14 days after instillation.

The ^{3}He morphometric parameters for the elastase-treated mice are summarized in **Table 7-1**. Compared the healthy mice in Chapter 6, the results from elastase-treated mice demonstrated clear, statistically-significant increases in *Lm* and *R* (averages of 78 μm and 107 μm, respectively, with significant regional variation); *h* was reduced to an average of 47 μm; all were corroborated by conventional tissue histology. Alveolar density and

surface-to-volume ratio were also significantly reduced in the elastase group compared to healthy mice (N_a = 2887 vs 3842 mm^{-3} in healthy mice and S/V = 537 vs 698 cm^{-1} in healthy mice).

Mouse No.	R (μm)	h (μm)	Lm (μm)	N_a (mm-3)	S/V (cm-1)
E1	113.7 ± 12.1	44.6 ± 5.1	89.8 ± 20.1	2410 ± 724	467 ± 102
E2	101.4 ± 7.9	49.7 ± 5.8	69.7 ± 13.4	3280.1 ± 617	592 ± 94.8
E3	109.9 ± 8.5	46.0 ± 4.1	83.0 ± 14.6	2587 ± 537	496 ± 79.8
E4	101.7 ± 8.5	50.0 ± 6.1	69.9 ± 14.9	3270 ± 691	594 ± 106
Mean	106.7	47.6	78.1	2890	537
Std Dev	6.1	2.7	10	455	65.3

Table 7-1: Summary of morphometric parameters obtained via ^{3}He MRI from 4 elastase-treated mice

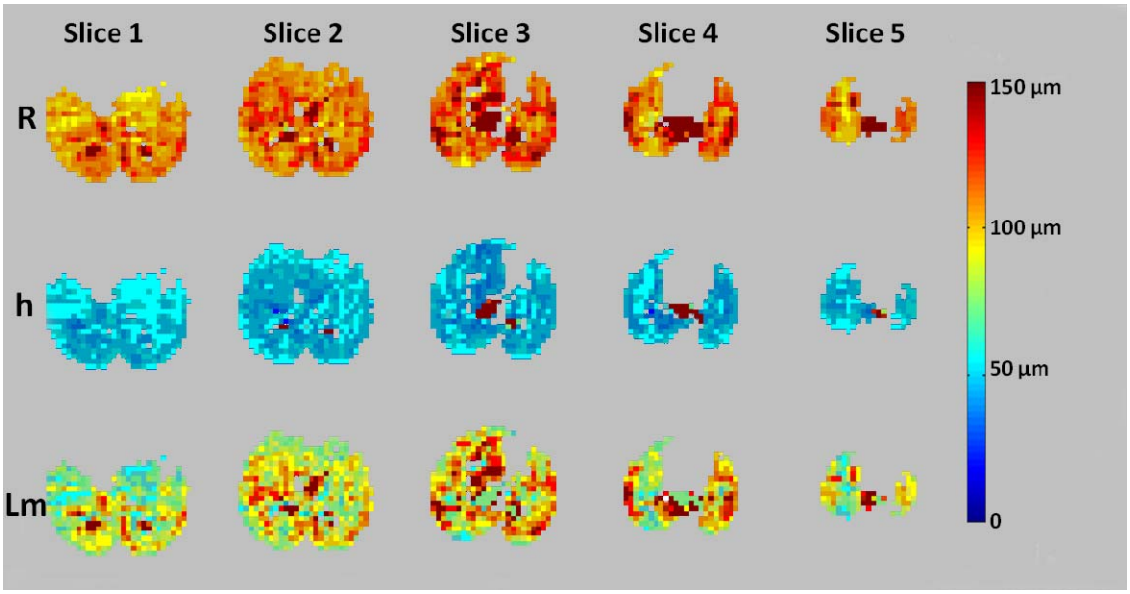

Figure 7-1: Representative geometric parameter (*R*, *h*, *Lm*) maps obtained from one elastase mouse lung.

7.2 Sendai Virus Infected Mouse Model

Sendai-virus (SeV) infection in mice is an experimental model of chronic lung disease with pathology that resembles asthma and COPD in humans (43, 57). It has been widely investigated as a suitable model of respiratory viral infections (44). The effect of SeV on distal lung airspaces, however, has not been investigated before.

Here we quantify mouse lung microstructure with ^{3}He diffusion MRI at different time points after SeV infection *in vivo*. The main issue we attempted to address was whether SeV infection causes enlargement of distal lung airspaces. To our knowledge, this is the first investigation into the microstructure changes in this mouse model of chronic inflammatory lung disease and first *in-vivo* study of this model via imaging.

7.2.1 Sendai Mouse Model Induction

Six groups of five C57BL/6J 5-6 week-old mice were used for SeV and phosphate-buffered saline (PBS) treatment: three groups of mice were infected by SeV and studied at 21 days, 49 days and 77 days after infection; two groups of mice were treated with PBS and studied at 49 days and 84 days after treatment; one group of untreated healthy mice were studied at 12 weeks.

Sendai virus was obtained from ATCC (VR-105) (113). The virus was twice plaque purified, propagated in 10-day-old embryonated chicken eggs and stored at -70C. Infectivity of SeV was assayed in VeroE6 cell line. Mice 5-6 weeks old were infected

intranasally with 2×10^5 pfu/mouse of SeV in 30µL and kept in a barrier facility until time of experiment.

7.2.2 MR Images

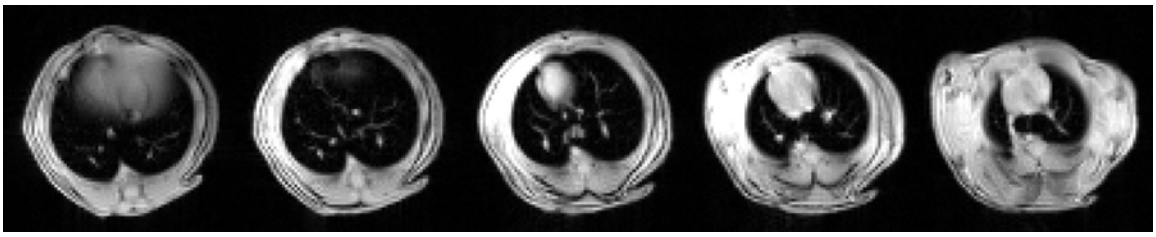

Figure 7-2: Representative set of ^{1}H MR images of PBS 49 day mouse

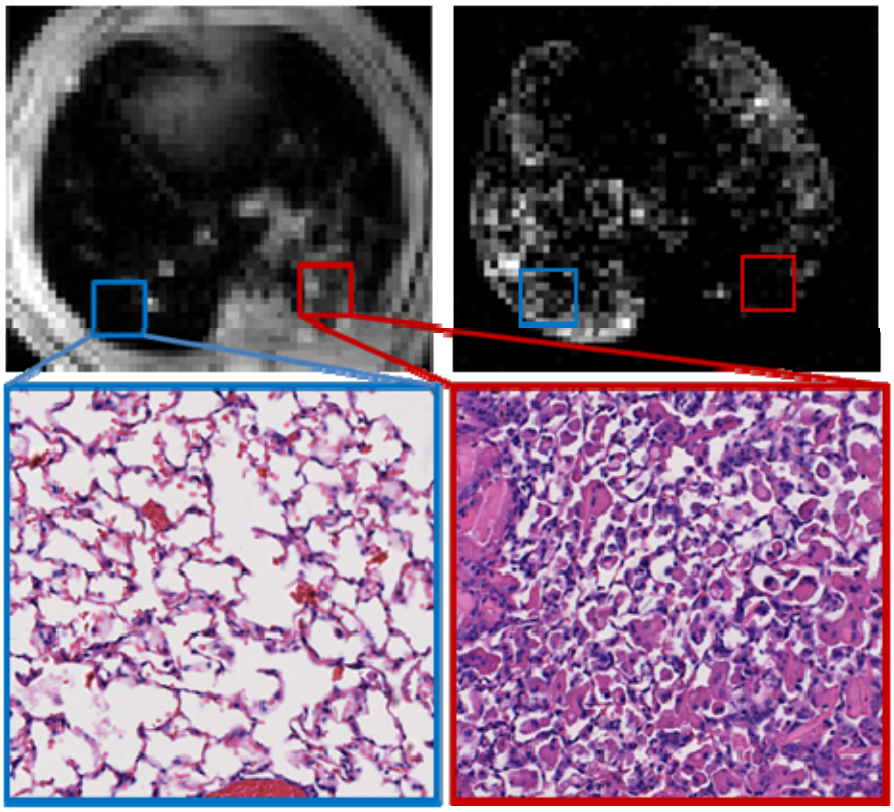

Figure 7-3: One representative ^{1}H MR image (upper left) and corresponding ^{3}He ventilation image (upper right) of a Sendai 77 day mouse. Microscope images correspond to the regions outlined in MR images. The lung parenchyma in the blue square is

relatively normal, while the red square shows significant inflammation induced by SeV. This is clearly shown by the higher ^{1}H signal and lower ^{3}He signal in the red square compared to the blue one.

^{1}H MR images were acquired for anatomical orientation and to detect inflammation. A representative set of ^{1}H MR images of one control mice is shown in **Figure 7-2**. In the groups of SeV infected mice, the ^{1}H images clearly revealed inflammation, as expected, as areas of increased intensity (spin density), which corresponded to ventilation defects (dark areas) in ^{3}He images at b = 0. This was further confirmed by histology (**Figure 7-3**). Areas of inflammation increased with time after infection through 77 days. Since there was nearly no signal from those regions in ^{3}He images, corresponding pixels were automatically eliminated from the parametric maps and subsequent analysis.

7.2.3 Morphometric Parameters

The fitting by Bayesian analysis on a pixel-by-pixel basis was excellent for every mouse in this study, and the RMS residues were all below 3% of the RMS signals.
Figure 7-4 shows a representative set of parameter maps for a SeV 21 day mouse. Parameter maps of R, h, Lm, N_a, S/V were generated for each mouse studied and the individual data are summarized in **Table 7-2**. There is no statistically significant difference between parameters of PBS 49 day mice and PBS 84 day mice. R and Lm in the infected group were indistinguishable from PBS 49 day mice at day 21 (R=102.9 and Lm=71.4 μm), increased slightly at day 49 (R=103.5 and Lm=71.2 μm, respectively), and were increased with statistical significance at day 77 (R=105.7 and Lm=75.4 μm,

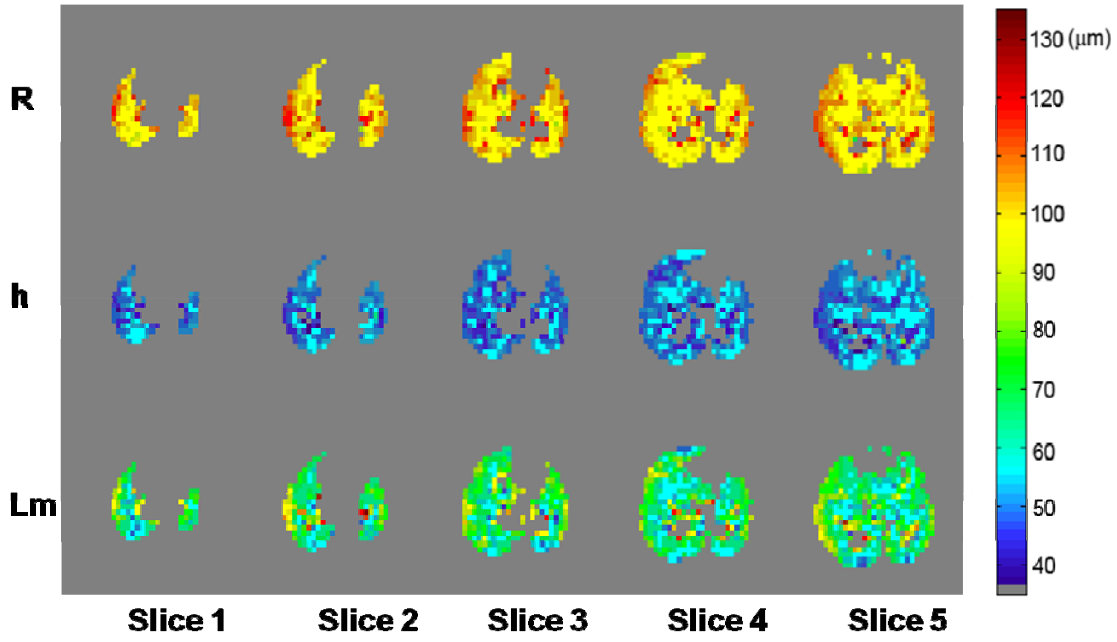

Figure 7-4: Representative parametric (*R*, *h*, and *Lm*) maps obtained from a Sendai 21 day mouse. Major airways are excluded. The colorbar shows the range of the parameters (*R*, *h*, and *Lm)* from 35 µm to 135 µm.

respectively; $p = 0.02$). Spatial variation of the morphometric parameters was apparent at each time point, with *R* and *Lm* more elevated at the lung periphery; these parameters increased as a function of time after infection (**Figure 7-5**, **Table 7-2**& **Table 7-3**). The mean value of *Lm* measured by histology for each group, after shrinkage correction, is also shown in **Table 7-2**. We note that individual slices shrinkage differed substantially (as much as a factor of 2), but the effect of differential shrinkage is minimized upon averaging over all slices.

Mouse	*R* (μm)	*h* (μm)	S/V (cm^{-1})	N_a (mm^{-3})	*Lm* (μm)	Lm by histology (μm)
PBS 49 day	102.8 ± 1.3 †	48.8 ± 0.7	587 ± 15†	3204 ± 102†	70.1 ± 1.8 †	53.7±5.3
PBS 84 day	102.1 ± 0.8 †	46.0 ± 0.5	562 ± 9†	3181 ± 69†	72.3 ± 1.4 †	-
SeV 21 day	102.9 ± 1.1†	49.9 ± 0.2	587 ± 9†	3219 ± 71†	71.4 ± 2 †	65.1±5.6 *†
SeV 49 day	103.5 ± 0.9 †	48.4 ± 0.7	585 ± 15†	3216 ± 105†	71.2 ± 1.7 †	59.7±8.5 †
SeV 77 day	105.7 ± 2.4 *§†	48.1 ± 1	559 ± 27*§†	3020 ± 174*§†	75.4 ± 4.4 *§†	66.9±3.7 *†
Control	97.2 ± 3.7*§	51.7 ± 3.2	698 ± 37*§	3841 ± 317*§	60.5 ± 3.5*§	52.0 ± 1.9

Table 7-2: Summary of morphometric parameters obtained via 3He MRI from PBS 49 day, PBS 84 day, SeV 21 day, SeV 49 day, SeV 77 day and untreated control mice with histological comparison. Values are means ± SD. Within each group all values were not significantly different between PBS mice and SeV infected mice except *$p < 0.05$ compared with the group of PBS 49 day mice, $^{\S}p<0.05$ compared with the group of PBS 84 day mice and $^{\dagger}p < 0.05$ compared with the untreated control group.

Mouse	*R* > 105 μm	*Lm* > 80 μm
PBS 49 day	17.8%†	10.3%†
PBS 84 day	13.9%	8.4%
Sendai 21 day	21.9%†	14.1%†
Sendai 49 day	24.1%*§†	15.8%*§†
Sendai 77 day	31.8%*§†	19.1%*§†
Control	6.9%*	3.4%*

Table 7-3: The percentages of voxels with R > 105 μm and the percentages of voxels with *Lm* > 80 μm for different groups of mice. *$p < 0.05$ compared with the group of PBS 49 day mice; $^{\S}p<0.05$ compared with the group of PBS 84 day mice; $^{\dagger}p < 0.05$ compared with the untreated control mice

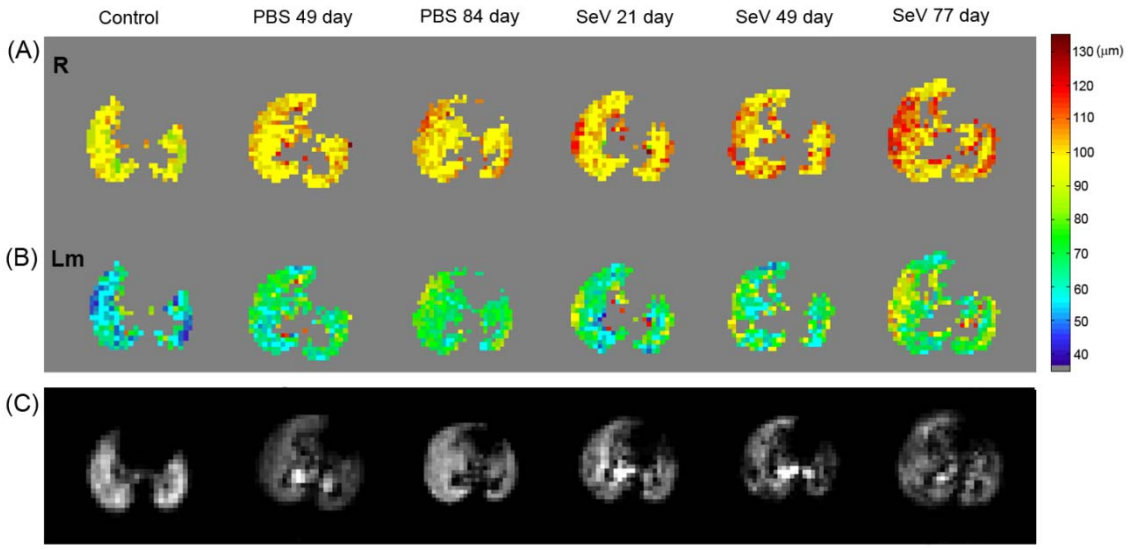

Figure 7-5: Representative *R*, *Lm* maps and transverse ^{3}He MR ventilation images from groups of PBS 49 day, PBS 84 day, SeV 21 day, SeV 49 day, SeV 77 day at the same slice location. The elevation of *R* and *Lm* in the periphery increases with time after SeV infection.

7.2.4 Threshold Analysis

In order to quantify the expansion of acinar airspaces, we performed a threshold analysis on the parameter maps of *R* and *Lm*. The percentage of pixels in which *R* is greater than a range of different threshold values was calculated. The percentage is 100% when threshold = 0 and 0% when threshold is the maximum value of *R* within all pixels. **Figure 7-6** shows the average calculated threshold curves from parameter maps of *R* of the six groups. At higher *R* thresholds, the percentage of pixels greater than the threshold grows with time after infection, indicating that there is a modest increase in acinar airspace size. (Similar results are seen with *Lm*, not shown in the figure.) Specifically,

for R > 105 μm, the percentage of pixels increases from 17.8% for PBS 49 day (14% for PBS 84 day) to 31.8% for SeV 77 day (**Table 7-2**). Similar results are also shown for *Lm* in the table.

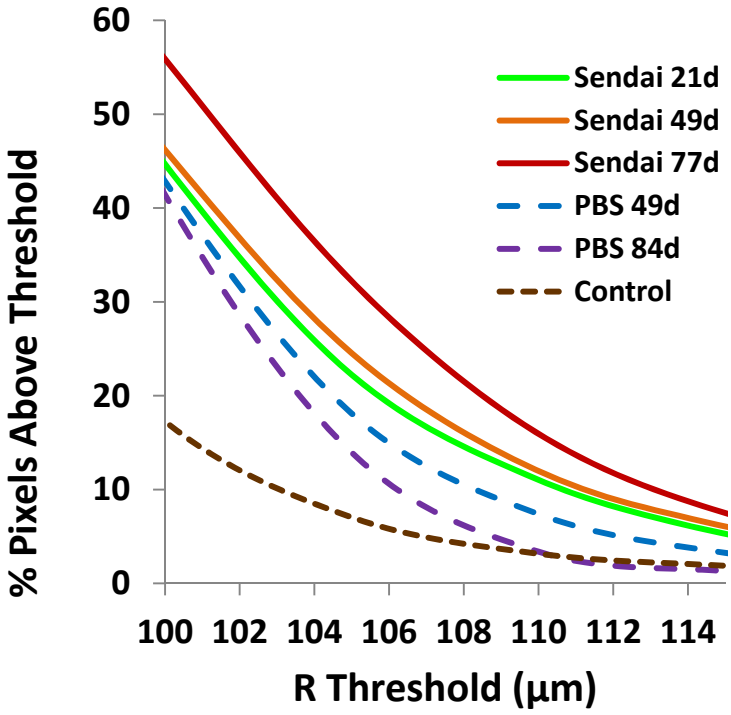

Figure 7-6: The percentages of voxels with R above a range of the threshold values for all groups of mice. The curves for control (Brown dashed line), PBS 49d (Purple dashed line) and PBS 84d (blue dashed line) have lower percentage values compared with SeV infected groups (solid line) at high value range of R (100-105 μm shown here), indicating there are more pixel with higher R values in the SeV infected groups than the control and PBS groups.

7.2.5 Volume Measurements

The total lung volume for each mouse both from ^{3}He MR measurement and ^{1}H MR measurement are also shown in Table 7-4. **Figure 7-7** confirmed the consistency of measured ^{3}He-MR and ^{1}H-MR volume.

Mouse	Volume (^{3}He MR) (mm^3)	Volume (^{1}H MR) (mm^3)
PBS 49 day	1208 ± 135	1055 ± 125
PBS 84 day	1094 ± 218	940 ± 179
SeV 21 day	1155 ± 287	997 ± 253
SeV 49 day	1250 ± 248	1103 ± 174
SeV 77 day	1212 ± 220	1063 ± 154
Control	917 ± 64	808 ± 69

Table 7-4: The total lung volume measured from ^{3}He MR measurement and ^{1}H MR

The estimated volume by ^{1}H and ^{3}He MRI are tightly correlated although the volumes measured by ^{1}H MRI are consistently smaller. This is because that ^{1}H MR image has four times the resolution of ^{3}He image. Overestimation of lung volume by ^{3}He images may be understood by the fact that ^{3}He pixels on the outer contour of the lung have larger size than ^{1}H pixels and are more likely counted as lung volume for partial-helium-containing pixels with high SNR.

The estimated total lung volume can be used to examine if there is subsequent airspace enlargement by lung expansion after SeV infection. The results from volume measurements showed that there is no connection between volume change and viral

infection. Comparing Sendai 77 day mice with PBS 49 day mice, the average of *R* increased by 2.8%; if this were solely caused by volume expansion the average of volume should have increased by 8.6% ($V \propto R^3$ for isotropic expansion). However, the actual average of volume increase was only 2.5%. While we cannot be precise about the relative amounts of destruction vs. volume expansion via these small increases, the volume changes serve as evidence that there is airspace enlargement caused not by volume expansion.

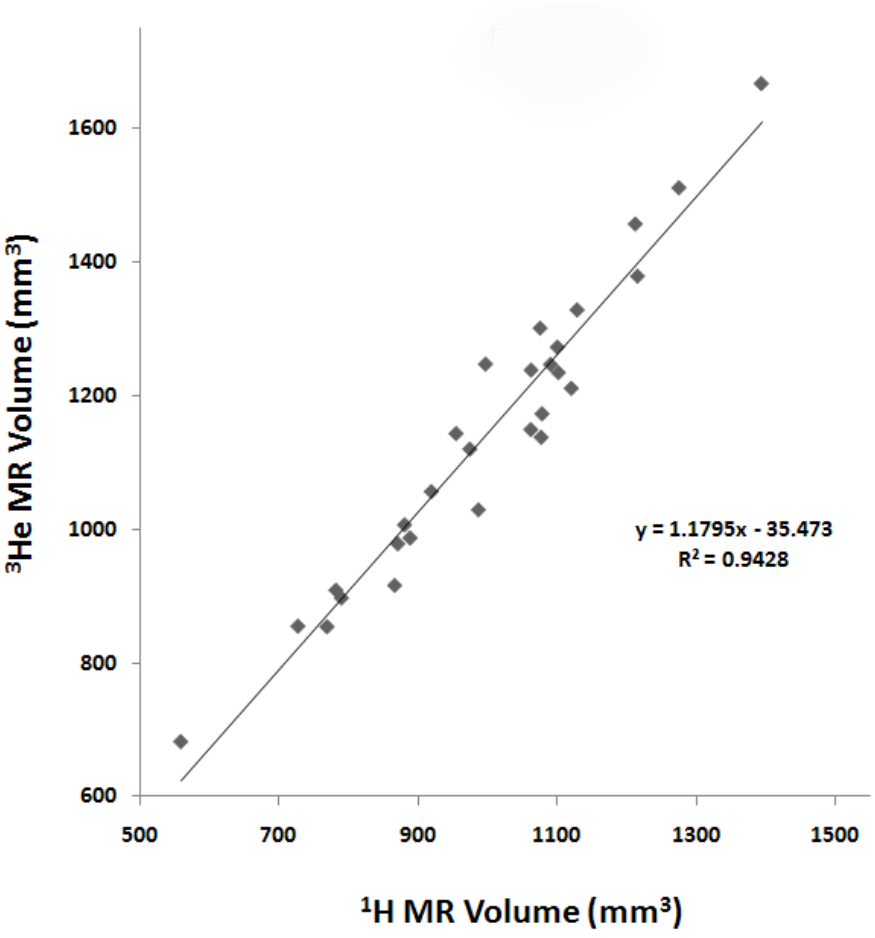

Figure 7-7: Linear regression of lung volumes measured by ^{3}He-MR and ^{1}H-MR methods.

A small limitation of this volume measurement was the fact that only five ^{1}H images were acquired; thus, in a few cases the most cranial or caudal parts of the lung were not included.

7.2.6 Discussion

In this study, we applied ^{3}He lung morphometry to detect and quantify the *in-vivo* lung microstructure changes well after initial SeV infection. Modest increases in alveolar duct radius distal to airway inflammation were measured by our imaging method, with some focal areas of greater increase in the lung periphery.

The SeV-infected mice show a similar increase in *Lm* via histology as via MRI, compared to controls; however, there are several advantages to quantitative imaging. First and foremost, the invasive nature of histology prohibits its use in human longitudinal studies, whereas imaging can be performed serially and noninvasively, with results reflecting the in-vivo lung. (Although serial imaging would have been possible in this study, animal regulations prevented reintroduction of infected mice into the animal facility. We have scanned many mice serially without incident.) Second, the precision of true stereological measurements requires significant work, careful specimen preparation, and an unbiased sampling scheme. In contrast, our imaging process takes less than 5 minutes per mouse from which whole lung morphometry with regional information is easily extracted. Further, traditional quantitative histology is affected by tissue shrinkage. While some methods suffer less than others (79), the estimation of shrinkage factor will significantly affect the final results. In our histological measurement, the shrinkage factor was estimated for each mouse by strictly following the tenets outlined in the ATS/ERS

statement on the quantitative assessment of lung structure (48). Even a small estimation error of shrinkage factor will obscure the changes of *Lm*. This concern does not exist with the imaging method.

The increases in airspace size seen here are smaller than those reported for smoke-exposed, C57BL/6J mice, though many of those increases are also quite modest (~ 14%) (18, 33). An increase of *Lm* was also observed in other mouse strains with exposure to cigarette smoke, and the *Lm* change was shown to be strain dependent, with increases ranging from 0 - 38% (33, 39, 68, 69). Although the increase in *Lm* here in the SeV model (6 %) is mild, the trend is clear and statistically significant. The SeV model holds some advantages as a model of chronic obstructive lung disease in that it shows some important physiological changes: chronic airways inflammation, airways hyperreactivity and mucus cell hyperplasia, all of which are absent in the cigarette-smoking model (85, 105, 110).

The Sendai virus mouse model is used as a model of chronic inflammatory lung disease that resembles asthma and COPD in humans, and previous studies have focused on airway inflammation. The chronic effects of the virus on expansion of distal lung parenchyma, however, have not been well studied. This study is the first report on the chronic effects of Sendai virus infection on distal airspaces and first study using imaging to quantify *in-vivo* lung microstructure changes due to viral infection. It reveals a link between a small amount of acinar-airway dilatation and earlier virus infection. Moreover, our study reveals that Sendai-virus infection may indeed have the potential to become a valid murine model of COPD: there is significant pulmonary inflammation after SeV infection and subsequent progressive acinar-airway expansion.

7.2.7 Micro-CT Study of Sendai Mouse Model

Before the MRI study of SeV mouse model, we made an effort to quantify the lung microstructural changes *ex vivo* using micro-CT.

We fixed one mouse lung on 77-day after Sendai virus infection and one normal lung by a special fixation process: the mouse lung was first fixed in a solution of 1% glutaraldehyde in pure acetone at -80°C overnight, warmed to room temperature, washed in pure acetone several times and post-fixed in 1% osmium tetroxide in acetone for 1 hour. Because dry, exsanguinated lungs attenuate x-rays very little, the osmium tetroxide will increase the contrast of micro-CT images. The samples are then rewashed several times in anhydrous ethanol and critically-point dried to remove remaining fluid inside the alveolar air space. The critical point method is a simple method to dry fragile objects without subjecting them to gross effects of surface tension forces (34).

The fixed lungs were imaged using a small angle cone beam system (micro-CT 40, Scanco Medical, Bruttisellen, Switzerland) with isotropic resolution of 6 μm (45kV tube potential, 177 μA tube current, and a 300 ms integration time for each projection). The scanning was repeated ten times and averaged to reduce noise. Continuous slices obtained using micro-CT were stacked up to reconstruct the tissue structure in 3D.

Figure 7-8 is a representative micro-CT slice from the SeV infected mouse lung. The method we used to estimate the regional microstructure is measuring outer radius (R) and inner radius (r) of the acinar duct whose direction is within the slice (**Figure 7-9**). We measured 10 such airways in both the normal lung and infected lung and the results are summarized in **Table 7-5**. The mean value of parameters R, r, and h of infected lung are

greater than those of the normal lung although there is large variation for the parameters in the infected lung. More precise 3D measurement method based on the microCT was proposed by (83). We adopted this approach as well and obtained similar results.

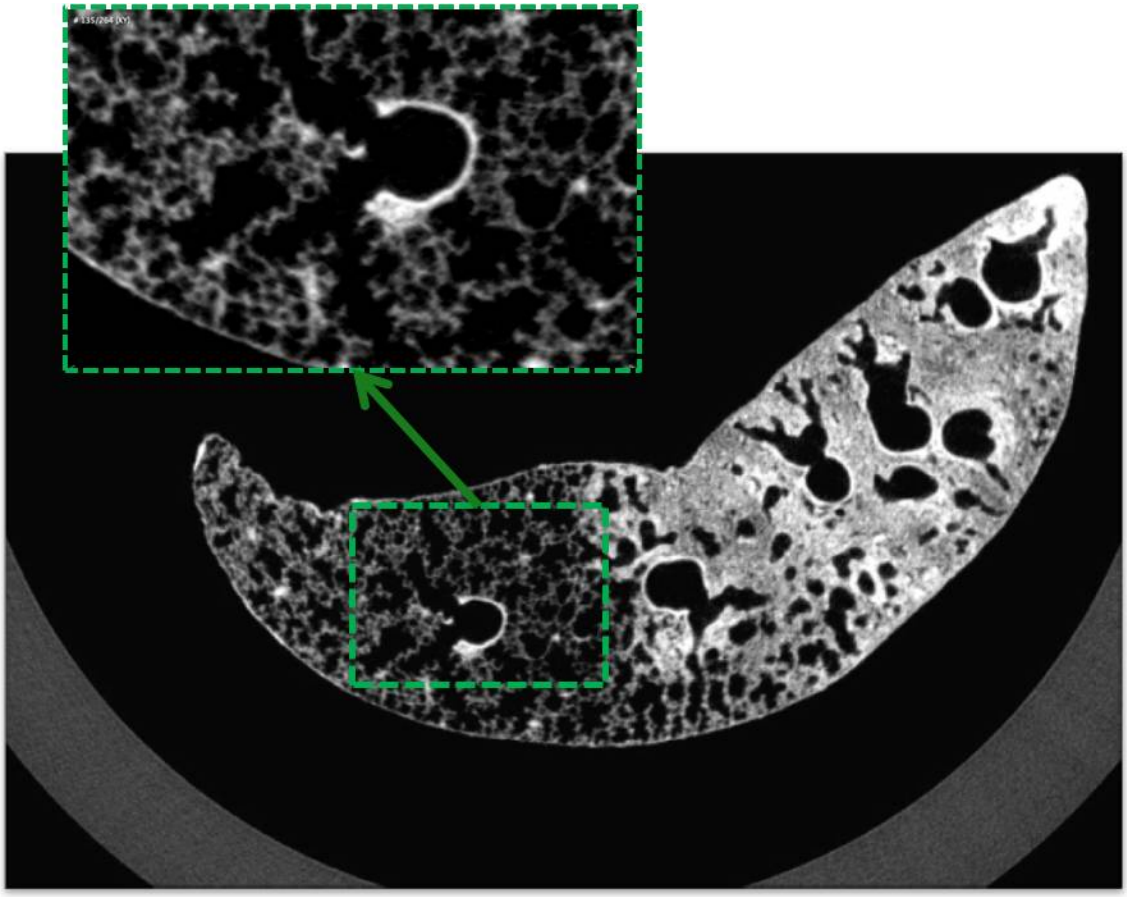

Figure 7-8: 2D micro-CT imaging slice with a zoom-in window showing that a terminal bronchiole branches into several acinar airways whose direction are within the slice. The hyper intense area without any alveoli shown is the area with significant inflammation.

It took great efforts to characterize microstructure by micro-CT measurement in lung fixation, imaging, and image analysis. Moreover, this is still *ex-vivo* technique which

cannot use for longitudinal study. To get a 2D micro-CT imaging data set like **Figure 7-8**, it took 11 hours to image only half volume of one mouse lung. So the in-vivo study of this kind is not applicable due to the radiation dose limit.

Average (StdDev)	Acinar-duct diameter, D (μm)	inner diameter, 2r(μm)	Alveolar depth, h=(2R-r)/2(μm)
Healthy Lung	93 (9.2)	48 (8.4)	22 (1.9)
Infected Lung	103(46.2)	67(39.7)	37(12.0)

Table 7-5: The acinar-duct measurement based on the acinar airways whose directions are within the 2D micro-CT imaging slice. The infected mouse lung shows enlarged airspaces compared to the normal mouse lung.

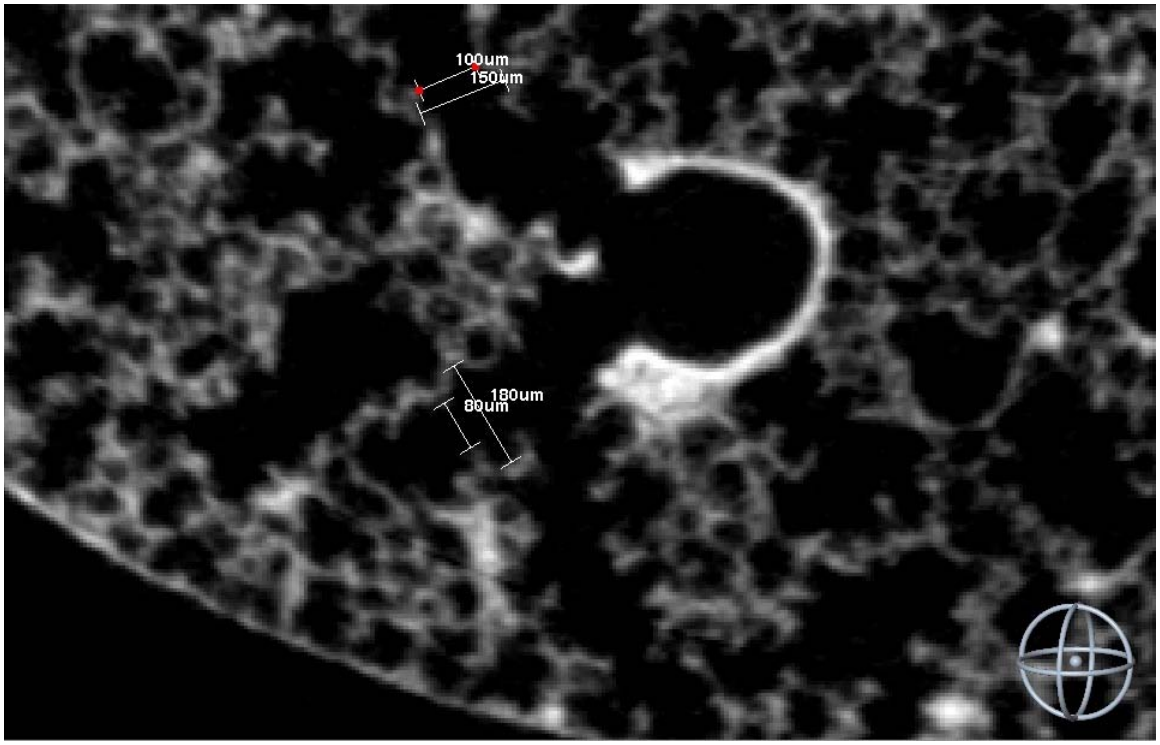

Figure 7-9: Measurement of outer diameter and inner diameter of acinar duct on 2D micro-CT slice of a Sendai-virus infected mouse lung. The acinar airways with directions within the micro-CT imaging slice are used to make the measurement (two sets of measurements shown in the figure).

Chapter 8
Results from Mouse Model of Lung Regeneration

8.1 Morphometric Studies on Pneumonectomy (PNX) Model

In earlier studies of PNX models, quantitative morphological methods were employed (15, 63) to study microstructural changes during compensatory lung growth; later, design-based stereology was more routinely available to characterize the structural changes after PNX (25). All these quantification of compensatory lung growth, however, could only be accomplished after sacrifice of the animal and removal of the lungs for histological analysis at a single time point. In addition, unless the entire lung undergoes exhaustive serial sectioning and analysis, assessment of differential lung growth cannot be fully determined since tissue analysis is limited to the sections sampled. A non-invasive morphometric method would be extraordinarily useful for longitudinal studies to fully understand the time course and the mechanism of compensatory lung growth in the PNX model, which will shed light on both lung development and potential regeneration. The ability to track individual animals longitudinally and noninvasively during compensatory lung growth will provide unique insights into the quantitative physiology of the lung regeneration.

In this study, we employed ^{3}He MRI to image *in-vivo* morphometry at baseline and to serially assess compensatory growth after left pneumonectomy in mice. The microstructural changes (R: alveolar-duct radius, h: alveolar depth, Lm: mean linear

intercept, among other parameters) after PNX were quantified and the time course of compensatory lung growth was evaluated. The formation of new alveoli and the restoration of the alveolar gas exchange area are assessed non-invasively. With this technique, we now have a non-invasive, *in-vivo* method to serially assess the effectiveness of therapeutic interventions on post-pneumonectomy lung growth in the same mouse.

8.2 First MR Morphometric Study

The aim of our first study of PNX is to investigate if ^{3}He morphometry can be useful tool for quantifying lung growth in the lung regeneration model. C57BL/6 mice aged 12 weeks underwent either left PNX (n=8) or left thoracotomy without lung resection (Sham; n=1). We set six different time points to trace the lung growth in the same animal: before PNX (baseline) and on days 2, 4, 8, 15, 36 after surgery in order to determine the time course of the post-PNX lung growth.

Parameter maps (*R, h,* and *Lm*) at baseline, and post-PNX days 2, 4, 8, 15, and 36 were generated for individual mice. Representative *Lm* maps for one mouse are shown in **Figure 8-1**. For the PNX mice we studied, a significant increase (5.7% to 8.0%) was seen in *Lm* (**Table 8-1**) at 2, 4, 8, and 15 days after PNX compared with baseline average *Lm* = 62.6 μm ($p < 0.05$ in all cases). This alveolar-space enlargement corresponded to the expansion of the remaining right lung after PNX. At day 36, the *Lm* (2.64% increase compared to baseline) was statistically significantly smaller than those at days 8 and 15. The *Lm* decrease by day 35 suggests that there was new alveolar growth after PNX.

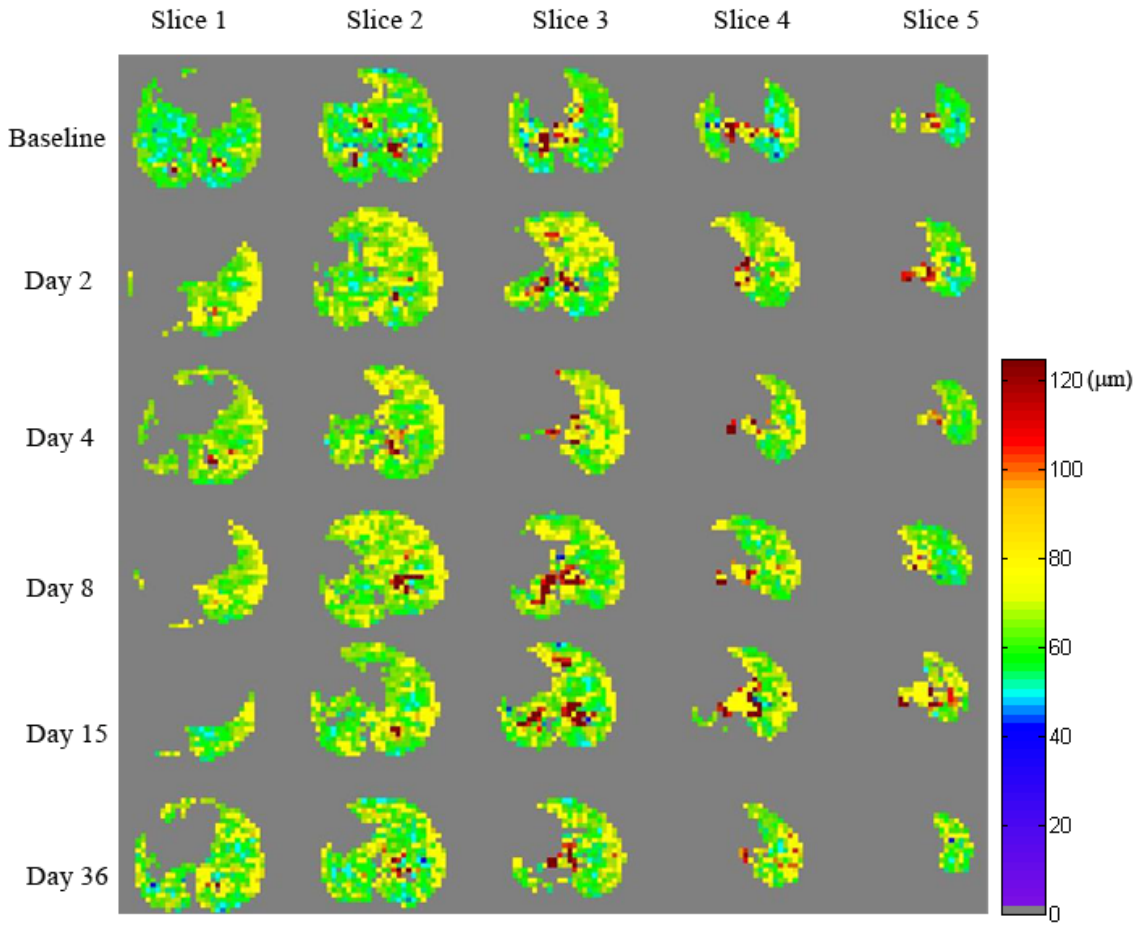

Figure 8-1: Representative *Lm* maps of one PNX mouse lung at baseline (pre-PNX), and days 2, 4, 8, 15 and 36 post-PNX. Note the slightly different scale used here from previous figures.

Further, we found that the increase of alveolar-space volume post PNX (8% increase in *Lm*, so a concomitant ~26% volume increase) was smaller than the macroscopic volume increase (30-70% increase in total volume, so likely an even larger increase in airspace volume). This can be explained by an increase of alveolar number, which implies significant compensatory lung growth even before day 36.

The sham mouse did not exhibit any significant changes in *R* and *Lm* during the 36-day period of observation (*R* = 98.3μm and *Lm* = 65.9 μm at baseline); the ~1% differences between days are a reasonable estimate of our measurement error.

Our imaging results are consistent with morphometric measurements reported in the literature for post-pneumonectomy compensatory lung growth in mouse (25, 106).

	PNX	**Sham (n=1)**
Day 2	+5.7% (n=8)	-1.1%
Day 4	+7.0% (n=6)	-
Day 8	+8.0% (n=3)	-
Day 15	+8.0% (n=3)	-0.6%
Day 36	+2.6% (n=3)	-1.1%

Table 8-1: The percentage changes of MRI-determined Lm of the right lung compared to baseline for PNX and Sham mice. The average baseline Lm is 62.6 μm for the PNX mice and 65.9 μm for the sham.

8.3 Second MR Morphometric Study

In the first study, the intense time points set enable us to determine three important time points for the second study: baseline, day 3 (immediate response to PNX), and day 30 (the completion of post-PNX growth). Different from the first study, we did ^{1}H MRI at two pressure levels to get more precise volume measurement and an estimation of compliance. Since the number of the time points was reduced, the mortality rate was decreased. We were able to keep all mice alive during the entire study.

Ten 12-week-old C57BL/6 mice were used: one group (n=6) underwent left lung PNX; the other group (n=4) was subjected to a sham operation (thoracotomy without tissue

resection). MRI was performed at baseline (immediately prior to PNX surgery), 3 day and 30 day after the surgery.

Standard one-way analysis of variance tests were used to compare results at different time points between PNX and Sham groups. The same statistical comparisons were also made among different time points within each group. A *p*-value of less than 0.05 was considered significant for the comparison.

8.3.1 Post-PNX Volume Expansion

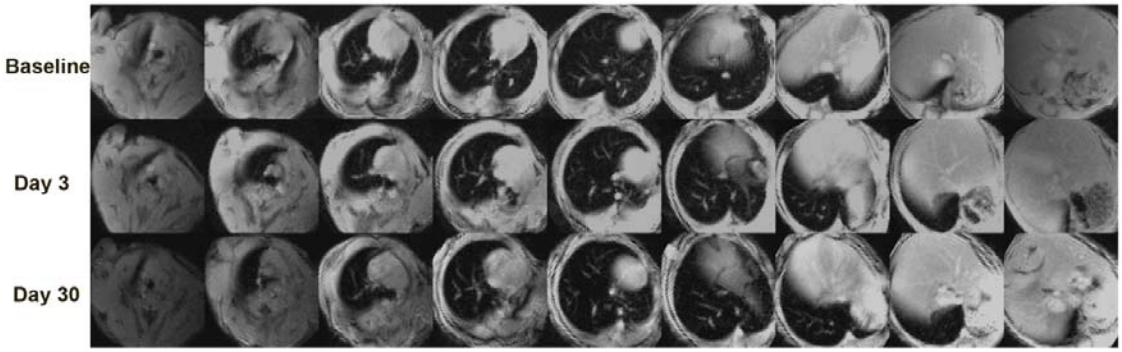

Figure 8-2: Representative ^{1}H MR images at different time points for a PNX mouse (axial imaging plane). Before PNX, tow lungs are shown. After PNX, only the right lung(appearing on the left in the images) remains in the thorax with great expansion of the volume. Part of the lung extending into the left thorax is the accessory lobe of the right lung.

Representative ^{1}H MR images for a PNX mouse are shown in **Figure 8-2**, illustrating enlargement of the remaining lung after PNX. In all the animals at baseline, the right lung accounted for ~65% of the total lung volume. For the PNX group, a striking increase of right lung volume (~30%) was observed at day 3 with further expansion (~15%) up to

day 30; for the sham group, the right lung volume remained unchanged during the time period (**Figure 8-3**).

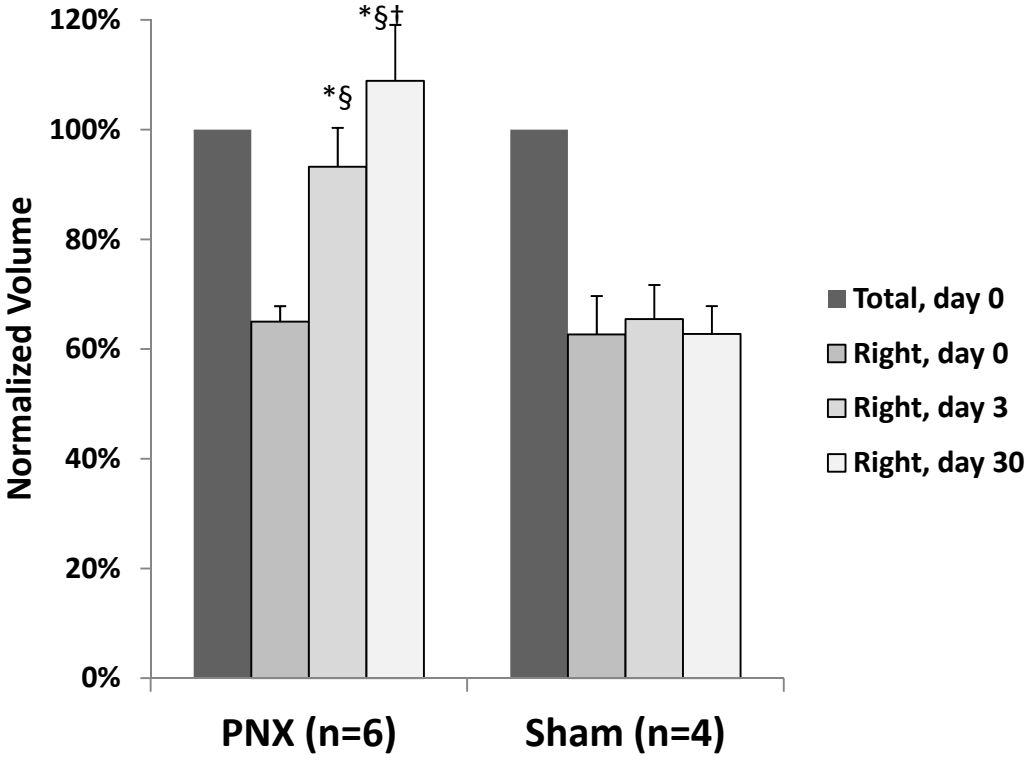

Figure 8-3: Lung volume for both lungs and right lung at baseline (pre-PNX) and residual right lungs at days 3 and 30 post PNX, measured at peak inspiration. Each mouse's measurements were normalized by its own baseline measurement from both lungs. Data are presented as mean ± SD. * $p < 0.001$ vs sham right lung at baseline, § $p < 0.001$ vs PNX right lung at baseline, † $p < 0.05$ vs PNX at day 3

8.3.2 Compliance Measurements

The ^{1}H MRI was performed twice during the same session: one acquisition during expiration; the other at the peak of inspiration ("lower" and "higher" pressure,

respectively). The volumes measured at two different pressures were used to calculate an effective lung compliance using following equation:

$$\text{Compliance} = \frac{\Delta V}{\Delta P} \tag{8.1}$$

The lung compliance increased remarkably (~ 2-fold) up at 3 days post-PNX and keep increasing after PNX (**Figure 8-4**), suggesting that the overall static mechanical properties were restored to pre-PNX level by day 30.

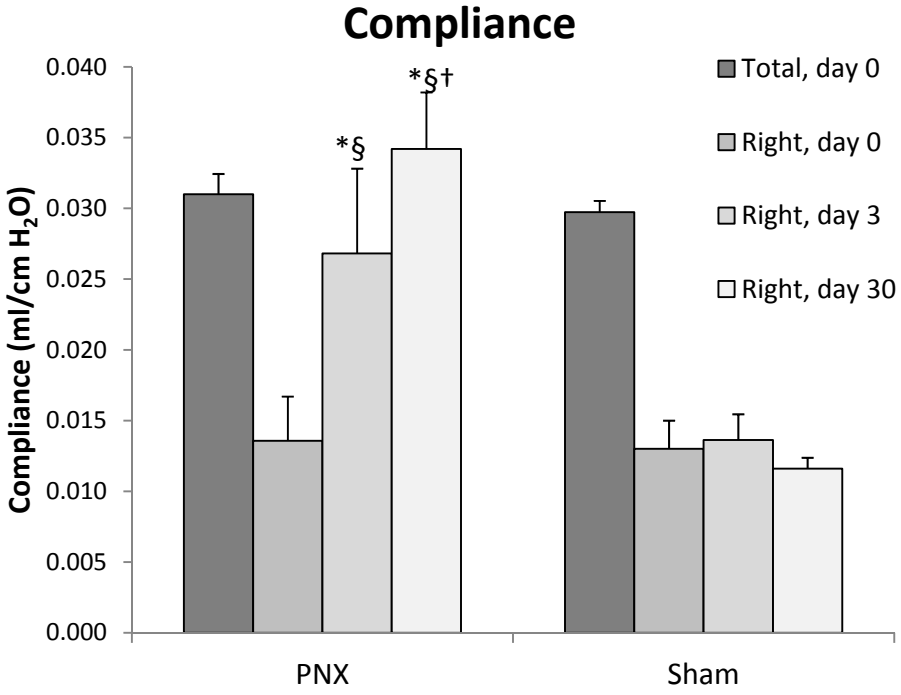

Figure 8-4: lung compliance for both lungs and right lung at baseline (pre-PNX) and residual right lungs at days 3 and 30 post PNX. Data are presented as mean ± SD. * $p < 0.001$ vs sham right lung at baseline, § $p < 0.001$ vs PNX right lung at baseline, † $p < 0.05$ vs PNX at day 3

8.3.3 Morphometric Parameters

Microstructural parameters *R*, *h*, and *Lm* of all mice were summarized in **Table 8-2**. Representative ^{3}He ventilation images and parametric maps from PNX groups at different time points are shown in **Figure 8-5**. *Lm* significantly increased by day 3 (~+10% compared to baseline, p = 0.0004) and then decreased by day 30 (~-3% compared to day 3, p = 0.03) for the PNX group. The same trend was observed in *R* and the opposite trend in *h*.

	Animals n	**R(μm)**		**h(μm)**		**Lm(μm)**	
		Right	Total	Right	Total	Right	Total
PNX, day 0	6	97.5 ± 2.5	97.4 ± 2.5	48.8 ± 2	49.2 ± 2	64.1 ± 4.7	63.7 ± 4.7
PNX, day 3	6	100.8 ± 2.2	100.8 ± 2.2	46.5 ± 1.5	46.5 ± 1.5	69.9 ± 4.1	69.9 ± 4.1
PNX, day 30	6	100.1 ± 1.4	100.1 ± 1.4	48 ± 1.6	48 ± 1.6	67.7 ± 2.8	67.7 ± 2.8
Sham, day 0	4	98.3 ± 3	98.1 ± 2.6	48.1 ± 1.8	48.5 ± 1.8	66 ± 5.3	65.4 ± 4.6
Sham, day 3	4	97.8 ± 2.1	97.5 ± 2.8	48.5 ± 2.9	48.8 ± 1.7	64.4 ± 5.2	63.8 ± 4.8
Sham, day 30	4	98.8 ± 2.5	98.9 ± 2.8	48.7 ± 2.7	49.1 ± 1.7	65.7 ± 5.4	65.5 ± 5.1

Table 8-2: Summary of morphometric parameters *R, h, Lm* of mice in PNX and Sham group at day 0, 3, 30.

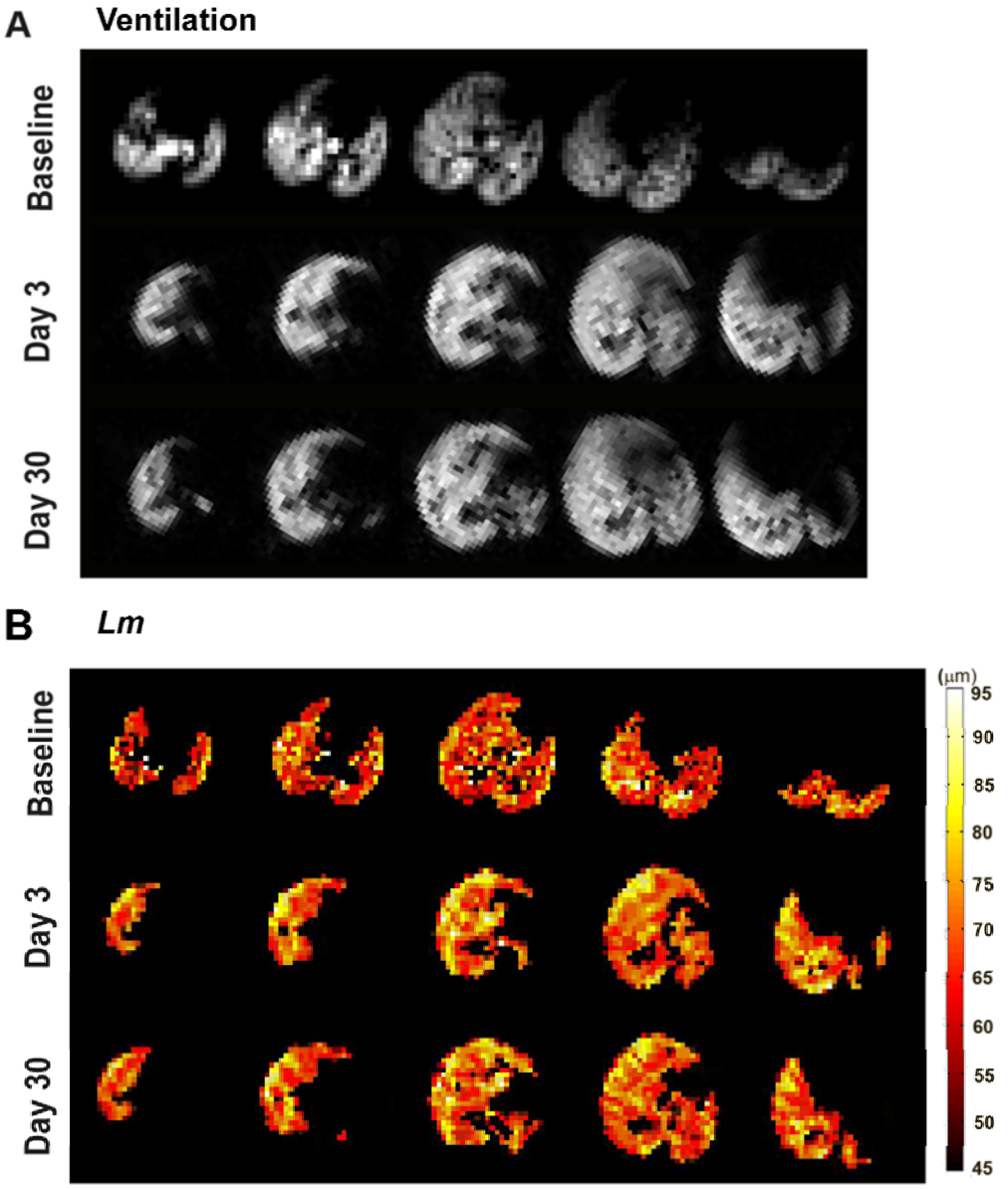

Figure 8-5: (A) Representative ventilation images of a PNX mouse at days 0, 3, and 30. (B) *Lm* map of the PNX mouse at days 0, 3, and 30. Note the different scale and color scale used here, used to better illustrate the changes over time.

This indicates an initial size increase of existing alveoli and the effect of expansion was weakened by the increase in number of total alveoli by day 30. This is also supported by

the results that there was no concomitant great increase in *R* with volume expansion by day 3 and there was even decrease in *R* by day 30 while remaining lung still expanded.

8.3.4 Total Alveolar Number

The compensatory lung growth leads to the remarkable increase of total alveolar number of the remaining lung after PNX. There was 30% gain in alveoli at day 3 post-PNX and 60% at day 30 post-PNX which achieve 100% of the total alveolar number of both lungs at baseline (**Figure 8-6**). This is strong evidence that during compensatory lung growth there is not only the growth of alveolar size but the growth of new alveoli.

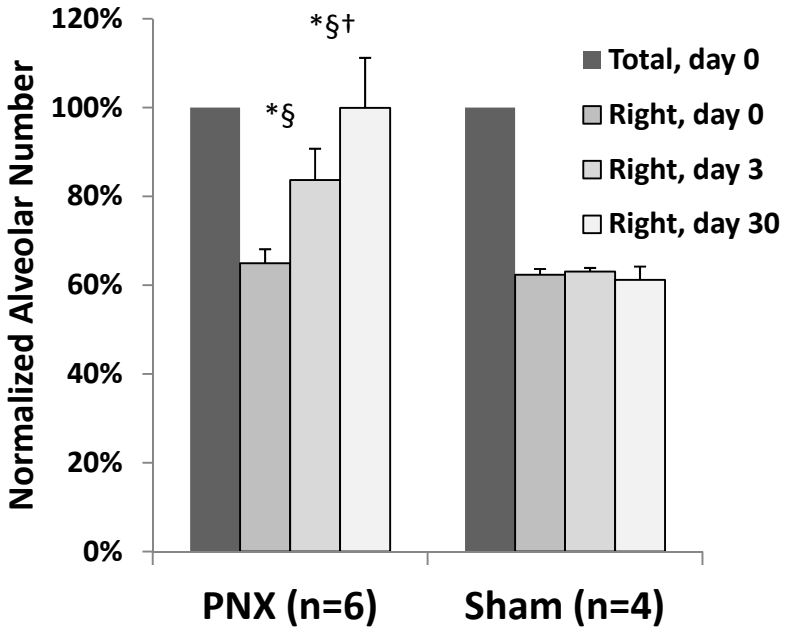

Figure 8-6: Total alveolar number for both lungs and right lung at baseline (pre-PNX) and residual right lungs at days 3 and 30 post PNX. Each mouse's measurements were normalized by its own baseline measurement from both lungs. Data are presented as mean ± SD. * $p < 0.001$ vs sham right lung at baseline, § $p < 0.001$ vs PNX right lung at baseline, † $p < 0.05$ vs PNX at day 3

8.3.5 Total Alveolar Surface Area

The total alveolar surface area of the right lung increased by 30% by day 3 compared with baseline and by day 30 reached the same level of two lungs at baseline (**Figure 8-7**). This demonstrates that compensatory lung growth resulted in the increase of the gas exchange area before day 3 and full restoration by day 30 in mice after PNX. The restoration is contributed by both the enlargement of the alveoli and the increase of alveolar number.

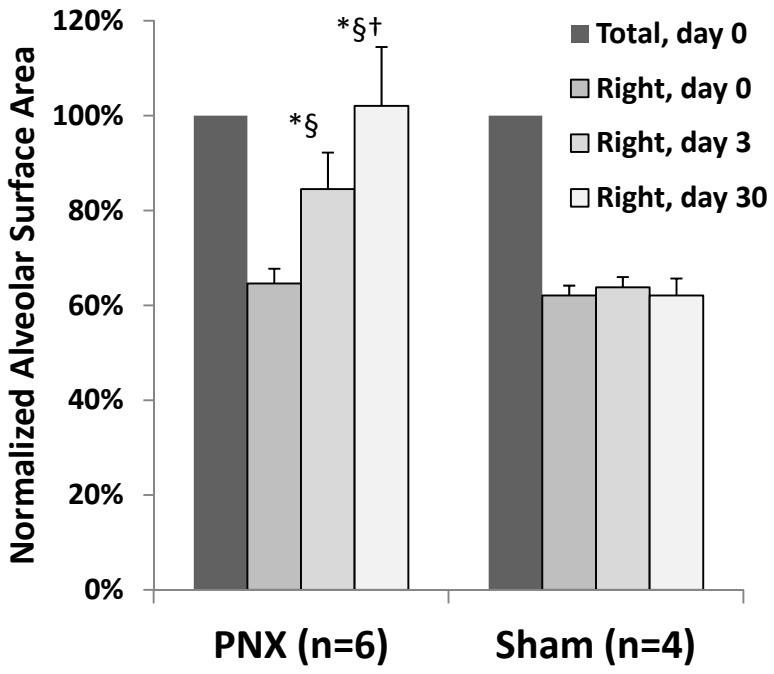

Figure 8-7: Total alveolar surface area for both lungs and right lung at baseline (pre-PNX) and residual right lungs at days 3 and 30 post PNX. Each mouse's measurements were normalized by its own baseline measurement from both lungs. Data are presented as

mean ± SD. * $p < 0.001$ vs sham right lung at baseline, § $p < 0.001$ vs PNX right lung at baseline, † $p < 0.05$ vs PNX at day 3

8.4 Discussion

This is the first *in-vivo* quantitative, longitudinal assessment of compensatory lung growth after PNX in mice via ^{1}H and ^{3}He MRI. Our results show an increase in alveolar size and complete restoration of the lung volume, the lung compliance, the total alveolar number and the total alveolar surface area by compensatory lung growth in mice *in vivo*. This is consistent with prior histological studies conducted in different animals at various time points. Compared to these studies, our ^{3}He morphometry technique is especially powerful in evaluating the dynamics of structural changes during compensatory lung growth after PNX.

The longitudinal study in the same animal by MRI can provides better understanding of the time course and the mechanism of post-PNX compensatory lung growth. Immediately after PNX, MR images showed the empty space was created within the thoracic cavity, which directly led to the expansion of the lung tissue. Quantitatively, on one hand, our results revealed that the volume normalization has almost been finished by 3-day post-PNX. On the other hand, in the early stage after PNX, the acinar space expanded disproportionally with the total lung volume, which reflected by the modest increase in *Lm* and *R*. This dispropotionality can be explained by the simultaneous increase of total alveolar number, which has already started within 3 days after surgery. The regeneration of alveoli continues after day 3 while the expansion of the total lung volume slows down. This is consistent with the slight decrease of *Lm* and *R* by day 30. The finding that the

formation of new alveoli lags behind the volume expansion supports the hypothesis that the mechanical stress and strain is the predominant *in-vivo* signal stimulating the compensatory lung growth.

Additional insights on mechanical properties of lung tissue are provided by compliance calculations based on volume measurements at two pressures via ^{1}H MRI. It was striking to see that the lung compliance increased dramatically by day 3 and full normalized by day 30, which is very similar to the increase of lung volume after PNX. This leads us to postulate that synthesis of lung elastin or collagen may have occurred during compensatory lung growth.

Another unique strength of ^{3}He morphometry is that it can provide the regionality of changes in lung microstructure by complete tissue sampling with relatively fewer efforts than traditional stereology. Parameter maps of each individual mouse show the regional variation of microstructure. Because the fissures are not resolvable in our MR images, currently we are not able to quantify the lobar difference during the compensatory lung growth. We did not see significant differences for the compensatory growth of different parts of the lung by images.

8.5 Comparison to Micro-CT Measurements

High-resolution computed tomography (HRCT) is another non-invasive approach that has been applied to PNX model (47). It can be used to reconstruct lobar anatomy and quantify regional morphology of the lung parenchyma and conduction structure. With the approach described in other literature (50, 112), the total lung volume can be partitioned into tissue+blood volume (V_{tissue}) and air volume (V_{air}). The air and tissue

volume following lung resection can be quantified by using CT attenuation value as follows:

$$V_{tissue} = \frac{CT_{lung} - CT_{air}}{CT_{tissue} - CT_{air}} \times V_{lung} \quad (8.2)$$

$$V_{air} = V_{lung} - V_{tissue} \quad (8.3)$$

where CT_{lung} is average CT number (in HU) within the lung region, CT_{air} is measured from the center of the tracheal air column within the chest, and CT_{tissue} is measured from muscle area.

Here for comparison purpose we present data from our micro-CT study of the PNX mouse model study. C57BL/6 mice aged 12 weeks underwent either left PNX (n=4) or left thoracotomy without lung resection (Sham; n=2). Each mouse was imaged at four time points: before pneumonectomy (baseline), 5-days post pneumonectomy, 12-days post pneumonectomy, and 21 days post pneumonectomy. Images were acquired on the Inveon MicroCT equipment (Siemens Medical, Malvern, PA, USA) at a FOV of 40 x 40 mm and 80-micron 3-D resolution (Tube voltage: 80 kVP; tube current: 500 μA). The mice were freely breathing during the imaging and the image acquisition was gated to be at full expiration.

Representative micro-CT images of one PNX mouse and one Sham mouse are shown in **Figure 8-8**. The tissue volume and air volume were calculated using Eqs. (8.2) and (8.3). Figure 8-9 shows the tissue volume and air volume changes at different time points for PNX and Sham group. We found simultaneous increases in air and tissue volume after PNX. After pneumonectomy, new alveolar growth definitely contributes to the tissue

Figure 8-8: Representative 2D Micro-CT images from a PNX mouse and a sham mouse. Five axial slices for three time points of baseline, 5 day, and 12 day after PNX were shown for each mouse.

volume increase. Moreover, perfusion to the remaining lung also increases after PNX, which will be counted in our tissue volume measurement here as well. The tissue volume and air volume for the Sham group was approximately the same at different time points.

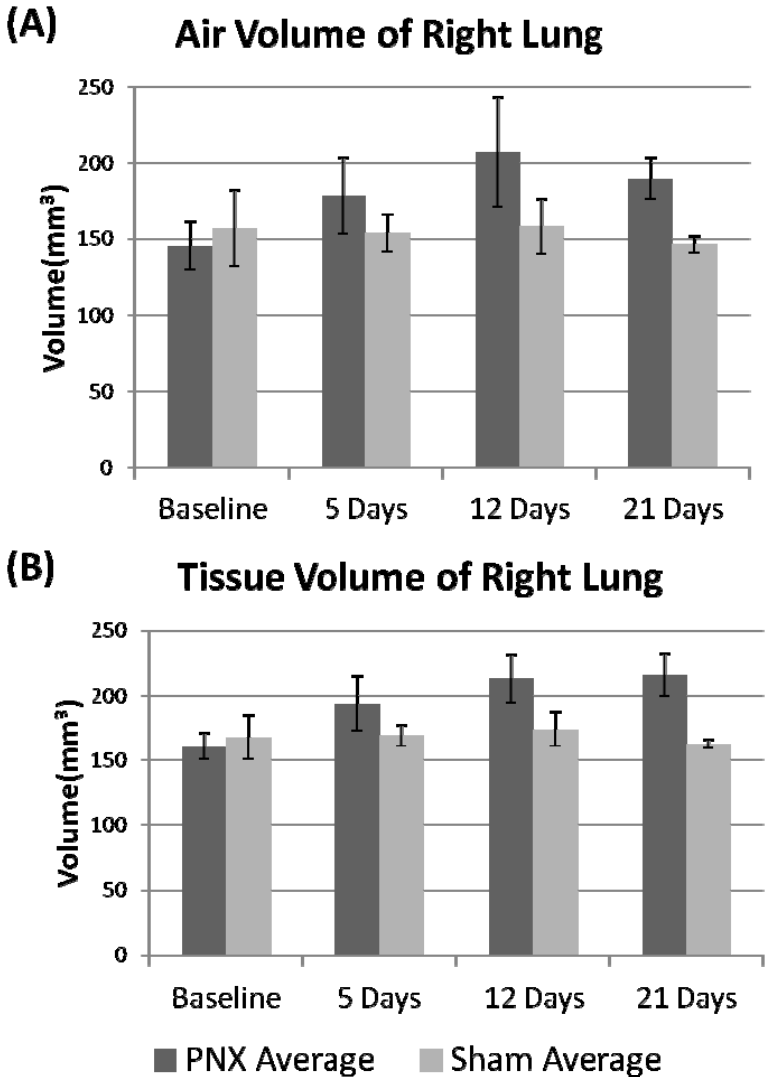

Figure 8-9: Air volume and tissue volume derived from micro-CT images of mouse lung at baseline and days 5, 12, 21 after PNX.

It should be noted that HRCT could not distinguish parenchyma tissue from microvascular blood although this fact does not detract from *in vivo* assessment of

compensatory response via CT (122). One of the main disadvantages of CT is the radiation exposure, which makes longitudinal study difficult; moreover, the current resolution limit precludes microstructural assessment. Compared to CT, MRI approach is radiation free and can precisely quantify the microstructure changes with regional information based on diffusion measurement.

Chapter 9
Conclusions

9.1 Specific Accomplishments

9.1.1 Implementation of ^{3}He Lung Morphometry in Mice *in vivo*

We have successfully implemented MRI based ^{3}He lung morphometry to quantify regional lung microstructure in the mouse *in vivo*. This technique allows us to measure the same physiological parameters as in histology (Lm, S/V, N_a), but noninvasively and with tomographic information. The technique also allows generation of the geometric parameters (R, r, h) characterizing the lung microstructure.

We present the first *in-vivo* images of mouse lung obtained with ^{3}He lung morphometry, with subsequent validation against direct quantitative histology. Our results show very small variation between healthy mice and are in good agreement with stereology performed with tissue sectioning and a microscope. *In-vivo* morphometry with MRI allows the geometry and size of the fundamental lung unit (the acinar airway, covered by alveoli) to be characterized. In the past, these parameters could only be assessed in the *ex-vivo* lung after sacrifice, often with significant time spent processing and analyzing, and with fairly large measurement error. Such promising attributes are likely to make ^{3}He lung morphometry a valuable tool for drug discovery and in understanding longitudinal and spatially-localized changes in individual animals.

9.1.2 ^{3}He Morphometry Applications to Mouse Pulmonary Disease Models

Precise quantification of microstructure in normal mouse lung by HP ^{3}He diffusion MRI opens up exciting possibilities for exploring structural changes at the alveolar level in a broad range of mouse pulmonary disease models, both longitudinally and with precise spatial localization and repeatability.

We have demonstrated successful *in-vivo* monitoring of mouse lung morphometry in various lung disease model including elastase model and Sendai virus model.

In elastase model, large increases in *Lm* and *R* and decreases in *h* were observed indicating enlarged airspace by tissue destruction. No significant change of microstructure was found in the smoking mice we studied (8 cigarettes/day or 4 cigarettes/day for 6 days a week for ~15 months). The increases in airspace size seen in our study are smaller than those reported for smoke-exposed, C57BL/6J mice, though many of those increases are also quite modest (~ 14%) (18, 33).

In Sendai mouse model, increases in alveolar-duct radius *R* and mean linear intercept *Lm*, both measured by ^{3}He diffusion MR images, imply that there is indeed a modest increase in alveolar-duct radius distal to airway inflammation, particularly in the lung periphery. Focal increases in *R* and *Lm* demonstrate mild tissue destruction 77 days after virus infection. The ability to noninvasively detect and quantify lung microstructure changes longitudinally brings an important new perspective to this potential mouse model of COPD.

9.1.3 ^{3}He Morphometry Applications on Compensatory Lung Growth Model

The results from our study on the pneumonectomy model were the first report to precisely quantify the *in-vivo* microstructural changes during post-PNX compensatory lung growth. The unique strength of this imaging technique is the ability to longitudinally study lung growth in the same animal and also to reveal the regional variation of microstructural changes. Specifically, our finding shows that the compensatory lung growth in murine model is achieved by both the alveolar multiplication and alveolar growth in size. The total lung volume, lung compliance, alveolar surface area, and alveolar number rapidly increase and got full restored by 30 days after pneumonectomy.

We concluded that ^{3}He morphometry has great potential to become a valuable tool in understanding the time course and the mechanism of lung growth in individual animals. It has great promise in providing insight into post-natal lung growth and lung regeneration.

9.1.4 Inflammation Detection by ^{1}H MRI

Noninvasive detection and quantification of inflammation in the mouse lung disease model have been demonstrated using ^{1}H MRI. The gradient echo sequence was used to obtain sharp images in the mouse chest with respiratory triggering. Although lung is challenging to examine with MRI because of low tissue density, this, at the same time, makes it good enough to discriminate mucus-secreting lung tissue from healthy lung tissue. The signals detected by MRI closely reflected the degree of inflammation.

In the SeV model, ^{1}H MR images detected the SeV-induced pulmonary inflammation *in vivo* and clearly revealed that the severity increased with the time after SeV infection.

With the ability to perform measurements in the same animal longitudinally, ^{1}H MRI shows promise in studying murine lung disease models characterized by inflammation and fibrosis and *in-vivo* profiling of anti-inflammatory drugs in mice.

9.2 Limitation of Our Technique

Our technique is limited by a simplified lung model, which relies upon a few reasonable assumptions, listed as follows:

We adopted the eight-alveolar model (eight alveoli around one alveolar duct) (38). Our method measures only two independent parameters (outer radius of acinar duct R and alveolar depth h), and is insensitive to changes in alveolar length, which depends on R in our model (121). This assumption holds well when alveoli expand proportionally in all directions.

We assumed that during the diffusion time (2Δ = 880 μs, the shortest possible time in our MR system), most ^{3}He atoms diffuse in a single acinar airway without escaping into adjoining airways. The limitation here is from the hardware -- the gradient slew rate and strength.

We simplify the distributions of acinar-airway sizes; in reality, these parameters vary depending on the position and branching level of the acinar-airway tree. However, the ranges are relatively small: R = 70-100 μm, r = 40-75 μm and h = 30-55 μm (81). We note that the precise mathematical model becomes invalid when tissue destruction become severe, although our previous study here demonstrated that ^{3}He morphometry still has good correlation with histology in patients with severe emphysema (121). In the

elastase model we studied, our model became invalid (by definition) because severe destruction of alveolar walls. Nevertheless, the geometric parameters we found can be considered as apparent values to access the degree of emphysema. In both SeV and PNX models of lung disease, the enlargement of acinar space was modest for which our technique is well suited.

9.3 Future Directions

The success of implementing ^{3}He lung morphometry *in vivo* opens up the door to many applications on mouse pulmonary models. In this dissertation, we have demonstrated the unique strength of our technique in a limited number of mouse lung models. In PNX model, for example, it would be of great interest to use our technique to quantify the lung regeneration (if there is any) after lung destruction. Some preliminary study of PNX on the elastase treated mice has been conducted. More data need to be acquired to draw a clear conclusion. There are still many more models that would benefit from longitudinal morphometric study by using this powerful technique. It can also serve as a precise *in-vivo* biomarker for drug discovery and development.

A routine has been developed to do animal handling and image mouse lung *in vivo* on our site, which achieves a very low mortality rate and good image quality for morphometric analysis. However, there are many aspects of our current protocol that can be further improved. For example, a more precise control and measurement of gas pressure delivered to the animal can be achieved by modification of the hardware. Using the current setup, special care and manual adjustment are always desired to maintain a stable pressure during the whole imaging process. Another concern is to improve the scheme of

scanning k space. Efforts can be made to shorten the total imaging time which will reduce the motion artifacts and gas consumption.

For ^{1}H MRI of mouse lung, there is much larger room for improvement. The TE we have achieved with our current gradient echo sequence and hardware is 0.95 ms which is even longer than the T_2^* of mouse lung (we estimate to be around 0.5 ms). Our SNR is ~2 for lung parenchyma for one average and TE = 0.95 ms. This implies that the information contained in the image intensity is subject to significant error. There is a strong need of advanced sequence development for ^{1}H MRI in mouse lung, and some significant work has already been done in the field. Kuthe et al. (62) showed excellent results in rat lung with UTE sequence and Corum et al. (21) have achieved significant signal in mouse lung with SWIFT sequence. Based on our hardware and sequence programming environment, we can develop feasible imaging sequence and protocol for ^{1}H mouse lung imaging with ultra-short TE.

References

1. **ABRAGAM A, and GOLDMAN M**. PRINCIPLES OF DYNAMIC NUCLEAR-POLARIZATION. *Reports on Progress in Physics* 41: 395-467, 1978.
2. **Albert M, Cates G, Driehuys B, Happer W, Saam B, Springer C, and Wishnia A**. Biological magnetic resonance imaging using laser-polarized 129Xe. 1994.
3. **Altes TA, Powers PL, Knight‐Scott J, Rakes G, Platts‐Mills TAE, de Lange EE, Alford BA, Mugler III JP, and Brookeman JR**. Hyperpolarized 3He MR lung ventilation imaging in asthmatics: preliminary findings. *Journal of Magnetic Resonance Imaging* 13: 378-384, 2001.
4. **Atkinson JJ, Holmbeck K, Yamada S, Birkedal-Hansen H, Parks WC, and Senior RM**. Membrane-type 1 matrix metalloproteinase is required for normal alveolar development. *Dev Dyn* 232: 1079-1090, 2005.
5. **Badea C, Hedlund L, and Johnson G**. Micro-CT with respiratory and cardiac gating. *Medical Physics* 31: 3324, 2004.
6. **Bardocz S, Tatar-Kiss S, and Kertai P**. The effect of alpha-difluoromethylornithine on ornithine decarboxylase activity in compensatory growth of mouse lung. *Acta Biochim Biophys Hung* 21: 59-65, 1986.
7. **Becker J, Ebert M, Grossmann T, Heil W, Hofmann D, Humblot H, Leduc M, Otten E, Rohe D, Siemensmeyer K, Surkau R, Steiner M, Tasset F, and Trautmann N**. Realization of a broad-band neutron spin filter with compressed, polarized He-3 gas. *Physica B* 234: 1078-1079, 1997.
8. **Becker J, Heil W, Krug B, Leduc M, Meyerhoff M, Nacher P, Otten E, Prokscha T, Schearer L, and Surkau R**. Study of mechanical compression of spin-polarized 3He gas. *Nuclear Instruments and Methods in Physics Research Section A: Accelerators, Spectrometers, Detectors and Associated Equipment* 346: 45-51, 1994.
9. **Brau A, Hedlund LW, and Johnson GA**. Cine magnetic resonance microscopy of the rat heart using cardiorespiratory‐synchronous projection reconstruction. *Journal of Magnetic Resonance Imaging* 20: 31-38, 2004.
10. **Bretthorst GL**. An Introduction to Parameter Estimation Using Bayesian Probability Theory. In: *An Introduction to Parameter Estimation Using Bayesian Probability Theory*, edited by PF F. Dartmouth: Kluwer Academic Publishers, 1989, p. p 53-79.
11. **Brody JS**. Time course of and stimuli to compensatory growth of the lung after pneumonectomy. *The Journal of clinical investigation* 56: 897-904, 1975.
12. **Brown LM, Rannels SR, and Rannels DE**. Implications of post-pneumonectomy compensatory lung growth in pulmonary physiology and disease. *Respiratory research* 2: 340-347, 2001.
13. **Brusselle GG, Bracke KR, Maes T, D'Hulst A I, Moerloose KB, Joos GF, and Pauwels RA**. Murine models of COPD. *Pulm Pharmacol Ther* 19: 155-165, 2006.
14. **Bushberg JT**. *The Essential physics of medical imaging*. Baltimore: Williams & Wilkins, 1994.
15. **Cagle PT, and Thurlbeck WM**. Postpneumonectomy compensatory lung growth. *The American review of respiratory disease* 138: 1314-1326, 1988.

16. **Callaghan P, and Eccles C**. Diffusion-limited resolution in nuclear magnetic resonance microscopy. *Journal of Magnetic Resonance (1969)* 78: 1-8, 1988.
17. **Callaghan PT**. *Principles of nuclear magnetic resonance microscopy*. Oxford England; New York: Clarendon Press ;Oxford University Press, 1991, p. xvii, 492 p.
18. **Cavarra E, Bartalesi B, Lucattelli M, Fineschi S, Lunghi B, Gambelli F, Ortiz LA, Martorana PA, and Lungarella G**. Effects of cigarette smoke in mice with different levels of alpha(1)-proteinase inhibitor and sensitivity to oxidants. *Am J Respir Crit Care Med* 164: 886-890, 2001.
19. **Chino K, Choong CK, Toeniskoetter PD, Cooper JD, Lausberg HF, Bae KT, Pierce JA, and Hogg JC**. A canine model for production of severe unilateral panacinar emphysema. *Exp Lung Res* 30: 319-332, 2004.
20. **Colegrove F, Schearer L, and Walters G**. Polarization of He^{3} Gas by Optical Pumping. *Phys Rev A* 132: 2561, 1963.
21. **Corum CA, Idiyatullin D, Moeller S, Chamberlain R, Sachdev D, and Garwood M**. Lung Imaging in the Mouse with SWIFT. *ISMRM* 2010.
22. **de Lange EE, Mugler III JP, Brookeman JR, Knight-Scott J, Truwit JD, Teates CD, Daniel TM, Bogorad PL, and Cates GD**. Lung air spaces: MR imaging evaluation with hyperpolarized 3He gas. *Radiology* 210: 851-857, 1999.
23. **Driehuys B, Cates G, and Happer W**. Surface Relaxation Mechanisms of Laser-Polarized^{129} Xe. *Physical Review Letters* 74: 4943, 1995.
24. **Dugas JP**. Hyperpolarzied ^{3}He mouse lung MRI: studies of lung structure and function. In: *Physics*Washington University in St. Louis, 2003.
25. **Fehrenbach H, Voswinckel R, Michl V, Mehling T, Fehrenbach A, Seeger W, and Nyengaard JR**. Neoalveolarisation contributes to compensatory lung growth following pneumonectomy in mice. *The European respiratory journal* 31: 515-522, 2008.
26. **FITZSIMMONS J, BECK B, and BROOKER H**. DOUBLE RESONANT QUADRATURE BIRDCAGE. *Magnetic Resonance in Medicine* 30: 107-114, 1993.
27. **Gast KK, Viallon M, Eberle B, Lill J, Puderbach MU, Hanke AT, Schmiedeskamp J, and Kauczor HU**. MRI in lung transplant recipients using hyperpolarized 3He: comparison with CT. *Journal of Magnetic Resonance Imaging* 15: 268-274, 2002.
28. **Gevenois PA, De Vuyst P, De Maertelaer V, Zanen J, Jacobovitz D, Cosio MG, and Yernault JC**. Comparison of computed density and microscopic morphometry in pulmonary emphysema. *American journal of respiratory and critical care medicine* 154: 187-192, 1996.
29. **Gewalt S, Glover G, Hedlund L, Cofer G, MacFall J, and Johnson G**. MR microscopy of the rat lung using projection reconstruction. *Magnetic Resonance in Medicine* 29: 99-106, 1993.
30. **Golman K, Axelsson O, Jóhannesson H, Månsson S, Olofsson C, and Petersson JS**. Parahydrogen-induced polarization in imaging: subsecond (13)C angiography. *Magn Reson Med* 46: 1-5, 2001.
31. **Gould G, MacNee W, McLean A, Warren P, Redpath A, Best J, Lamb D, and Flenley D**. CT measurements of lung density in life can quantitate distal airspace enlargement—an essential defining feature of human emphysema. *American journal of respiratory and critical care medicine* 137: 380-392, 1988.

32. **Gross P, Pfitzer E, Tolker E, Babyak M, and Kaschak M**. EXPERIMENTAL EMPHYSEMA: ITS PRODUCTION WITH PAPAIN IN NORMAL AND SILICOTIC RATS. *Archives of environmental health* 11: 50, 1965.
33. **Guerassimov A, Hoshino Y, Takubo Y, Turcotte A, Yamamoto M, Ghezzo H, Triantafillopoulos A, Whittaker K, Hoidal JR, and Cosio MG**. The development of emphysema in cigarette smoke-exposed mice is strain dependent. *Am J Respir Crit Care Med* 170: 974-980, 2004.
34. **Gusnard D, and Kirschner RH**. Cell and organelle shrinkage during preparation for scanning electron microscopy: effects of fixation, dehydration and critical point drying. *Journal of microscopy* 110: 51-57, 1977.
35. **Haake M, Natterer J, and Bargon J**. Efficient NMR pulse sequences to transfer the parahydrogen-induced polarization to hetero nuclei. *Journal of the American Chemical Society* 118: 8688-8691, 1996.
36. **Haefeli-Bleuer B, and Weibel ER**. Morphometry of the human pulmonary acinus. *Anat Rec* 220: 401-414, 1988.
37. **HAPPER W, and VANWIJNGAARDEN W**. AN OPTICAL-PUMPING PRIMER. *Hyperfine Interactions* 38: 435-470, 1987.
38. **Hartroft WS**. The microscopic diagnosis of pulmonary emphysema. *The American Journal of Pathology* 21: 889, 1945.
39. **Hautamaki RD, Kobayashi DK, Senior RM, and Shapiro SD**. Requirement for macrophage elastase for cigarette smoke-induced emphysema in mice. *Science* 277: 2002-2004, 1997.
40. **Hayhurst M, Flenley D, McLean A, Wightman A, MacNee W, Wright D, Lamb D, and Best J**. Diagnosis of pulmonary emphysema by computerised tomography. *The Lancet* 324: 320-322, 1984.
41. **Hedlund LW, Cofer GP, Owen SJ, and Allan Johnson G**. MR-compatible ventilator for small animals: computer-controlled ventilation for proton and noble gas imaging. *Magnetic resonance imaging* 18: 753-759, 2000.
42. **Holdsworth DW, and Thornton MM**. Micro-CT in small animal and specimen imaging. *Trends in Biotechnology* 20: S34-S39, 2002.
43. **Holtzman MJ, Tyner JW, Kim EY, Lo MS, Patel AC, Shornick LP, Agapov E, and Zhang Y**. Acute and chronic airway responses to viral infection: implications for asthma and chronic obstructive pulmonary disease. *Proc Am Thorac Soc* 2: 132-140, 2005.
44. **Homma M, Tashiro M, Allan G, and Robert GW**. Sendai Virus (Paramyxoviridae). In: *Encyclopedia of Virology*. Oxford: Elsevier, 1999, p. 1616-1621.
45. **Hsia CC**. Signals and mechanisms of compensatory lung growth. *Journal of Applied Physiology* 97: 1992-1998, 2004.
46. **Hsia CC, Herazo LF, Fryder-Doffey F, and Weibel ER**. Compensatory lung growth occurs in adult dogs after right pneumonectomy. *J Clin Invest* 94: 405-412, 1994.
47. **Hsia CCW**. Quantitative morphology of compensatory lung growth. *European Respiratory Review* 2006.
48. **Hsia CCW, Hyde DM, Ochs M, and Weibel ER**. An official research policy statement of the American Thoracic Society/European Respiratory Society: standards for quantitative assessment of lung structure. *American journal of respiratory and critical care medicine* 181: 394, 2010.

49. **Hunt E, and Carr H**. Nuclear Magnetic Resonance of Xe^{129} in Natural Xenon. *Physical Review* 130: 2302, 1963.
50. **Hyde RW, Wandtke JC, Fahey PJ, Utell MJ, Plewes DB, and Goske M**. Lung weight in vivo measured with computed tomography and rebreathing of soluble gases. *Journal of Applied Physiology* 67: 166-173, 1989.
51. **Idiyatullin D, Corum C, Moeller S, and Garwood M**. Gapped pulses for frequency-swept MRI. *Journal of Magnetic Resonance* 193: 267-273, 2008.
52. **Idiyatullin D, Corum C, Park JY, and Garwood M**. Fast and quiet MRI using a swept radiofrequency. *Journal of Magnetic Resonance* 181: 342-349, 2006.
53. **Jin J-M**. *Electromagnetic analysis and design in magnetic resonance imaging*. Boca Raton: CRC Press, 1999, p. xiv, 282 p.
54. **Kastler A**. Quelques questions concernant la production optique du ingalit du population des niveaux de qualification spatiale des atomes. Application a l'exprience de Stern et Gerlach et la resonance magnetique. *J Phys Radium* 11: 1950.
55. **Kauczor HU, Ebert M, Kreitner KF, Nilgens H, Surkau R, Heil W, Hofmann D, Otten EW, and Thelen M**. Imaging of the lungs using 3He MRI: preliminary clinical experience in 18 patients with and without lung disease. *Journal of Magnetic Resonance Imaging* 7: 538-543, 1997.
56. **Killian TJ**. Thermionic phenomena caused by vapors of rubidium and potassium. *Physical Review* 27: 578, 1926.
57. **Kim EY, Battaile JT, Patel AC, You Y, Agapov E, Grayson MH, Benoit LA, Byers DE, Alevy Y, Tucker J, Swanson S, Tidwell R, Tyner JW, Morton JD, Castro M, Polineni D, Patterson GA, Schwendener RA, Allard JD, Peltz G, and Holtzman MJ**. Persistent activation of an innate immune response translates respiratory viral infection into chronic lung disease. *Nat Med* 14: 633-640, 2008.
58. **Knudsen L, Ochs M, MacKay R, Townsend P, Deb R, Muhlfeld C, Richter J, Gilbert F, Hawgood S, and Reid K**. Truncated recombinant human SP-D attenuates emphysema and type II cell changes in SP-D deficient mice. *Respir Res* 8: 70, 2007.
59. **Knudsen L, Weibel ER, Gundersen HJ, Weinstein FV, and Ochs M**. Assessment of air space size characteristics by intercept (chord) measurement: an accurate and efficient stereological approach. *J Appl Physiol* 108: 412-421, 2009.
60. **Knust J, Ochs M, Gundersen HJG, and Nyengaard JR**. Stereological estimates of alveolar number and size and capillary length and surface area in mice lungs. *The Anatomical Record: Advances in Integrative Anatomy and Evolutionary Biology* 292: 113-122, 2009.
61. **Koh DW, Roby JD, Starcher B, Senior RM, and Pierce RA**. Postpneumonectomy lung growth: a model of reinitiation of tropoelastin and type I collagen production in a normal pattern in adult rat lung. *Am J Respir Cell Mol Biol* 15: 611-623, 1996.
62. **Kuethe DO, Adolphi NL, and Fukushima E**. Short data‐acquisition times improve projection images of lung tissue. *Magnetic Resonance in Medicine* 57: 1058-1064, 2007.
63. **Langston C, Sachdeva P, Cowan MJ, Haines J, Crystal RG, and Thurlbeck WM**. Alveolar multiplication in the contralateral lung after unilateral pneumonectomy in the rabbit. *Am Rev Respir Dis* 115: 7-13, 1977.

64. **Lauterbur PC**. Image formation by induced local interactions: examples employing nuclear magnetic resonance. *Nature* 242: 190-191, 1973.
65. **Le Bihan D**. *Diffusion and perfusion magnetic resonance imaging: applications to functional MRI*. Raven Press New York:, 1995.
66. **Leawoods JC, Yablonskiy DA, Saam B, Gierada DS, and Conradi MS**. Hyperpolarized 3He gas production and MR imaging of the lung. *Concepts in Magnetic Resonance* 13: 277-293, 2001.
67. **Madani A, Keyzer C, and Gevenois PA**. Quantitative computed tomography assessment of lung structure and function in pulmonary emphysema. *European Respiratory Journal* 18: 720-730, 2001.
68. **March TH, Barr EB, Finch GL, Hahn FF, Hobbs CH, Menache MG, and Nikula KJ**. Cigarette smoke exposure produces more evidence of emphysema in B6C3F1 mice than in F344 rats. *Toxicol Sci* 51: 289-299, 1999.
69. **March TH, Bowen LE, Finch GL, Nikula KJ, Wayne BJ, and Hobbs CH**. Effects of strain and treatment with inhaled aII-trans-retinoic acid on cigarette smoke-induced pulmonary emphysema in mice. *COPD* 2: 289-302, 2005.
70. **March TH, Green FH, Hahn FF, and Nikula KJ**. Animal models of emphysema and their relevance to studies of particle-induced disease. *Inhal Toxicol* 12 Suppl 4: 155-187, 2000.
71. **Marzola P, Osculati F, and Sbarbati A**. High field MRI in preclinical research. *European journal of radiology* 48: 165-170, 2003.
72. **Mauad T, Rivero DHRF, de Oliveira RC, Lichtenfels AJFC, Guimarães ET, de Andre PA, Kasahara DI, de Siqueira Bueno HM, and Saldiva PHN**. Chronic exposure to ambient levels of urban particles affects mouse lung development. *American journal of respiratory and critical care medicine* 178: 721-728, 2008.
73. **McBride JT**. Lung volumes after an increase in lung distension in pneumonectomized ferrets. *J Appl Physiol* 67: 1418-1421, 1989.
74. **Mitzner W, Fallica J, and Bishai J**. Anisotropic nature of mouse lung parenchyma. *Annals of biomedical engineering* 36: 2111-2120, 2008.
75. **Moller H, Chen X, Saam B, Hagspiel K, Johnson G, Altes T, de Lange E, and Kauczor H**. MRI of the lungs using hyperpolarized noble gases. *Magnetic Resonance in Medicine* 47: 1029-1051, 2002.
76. **Müller N, Staples C, Miller R, and Abboud R**. " Density mask". An objective method to quantitate emphysema using computed tomography. *Chest* 94: 782-787, 1988.
77. **Murray CJ, and Lopez AD**. Alternative projections of mortality and disability by cause 1990-2020: Global Burden of Disease Study. *Lancet* 349: 1498-1504, 1997.
78. **Newbury N, Barton A, Cates G, Happer W, and Middleton H**. Gaseous 3He-3He magnetic dipolar spin relaxation. *Physical Review-Section A-Atomic Molecular and Optical Physics* 48: 4411-4420, 1993.
79. **Oldmixon EH, Suzuki S, Butler JP, and Hoppin F**. Perfusion dehydration fixes elastin and preserves lung air-space dimensions. *Journal of Applied Physiology* 58: 105, 1985.
80. **Olsson LE, Lindahl M, Onnervik PO, Johansson LB, Palmér M, Reimer MK, Hultin L, and Hockings PD**. Measurement of MR signal and T2* in lung to characterize a tight skin mouse model of emphysema using single-point imaging. *J Magn Reson Imaging* 25: 488-494, 2007.

81. **Osmanagic E, Sukstanskii AL, Quirk JD, Woods JC, Pierce RA, Conradi MS, Weibel ER, and Yablonskiy DA**. Quantitative assessment of lung microstructure in healthy mice using an MR-based 3He lung morphometry technique. *J Appl Physiol* 109: 1592-1599, 2010.
82. **Osmanagic E, Sukstanskii AL, Quirk JD, Woods JC, Pierce RA, Conradi MS, Weibel ER, and Yablonskiy DA**. Quantitative Assessment of Lung Microstructure in Healthy Mice using an MR-based 3He Lung Morphometry Technique. *J Appl Physiol*.
83. **Parameswaran H, Bartolák-Suki E, Hamakawa H, Majumdar A, Allen PG, and Suki B**. Three-dimensional measurement of alveolar airspace volumes in normal and emphysematous lungs using micro-CT. *Journal of Applied Physiology* 107: 583-592, 2009.
84. **Patel AC, Morton JD, Kim EY, Alevy Y, Swanson S, Tucker J, Huang G, Agapov E, Phillips TE, and Fuentes ME**. Genetic segregation of airway disease traits despite redundancy of calcium-activated chloride channel family members. *Physiological genomics* 25: 502-513, 2006.
85. **Patel AC, Morton JD, Kim EY, Alevy Y, Swanson S, Tucker J, Huang G, Agapov E, Phillips TE, Fuentes ME, Iglesias A, Aud D, Allard JD, Dabbagh K, Peltz G, and Holtzman MJ**. Genetic segregation of airway disease traits despite redundancy of calcium-activated chloride channel family members. *Physiol Genomics* 25: 502-513, 2006.
86. **Quirk JD, Sukstanskii AL, Bretthorst GL, and Yablonskiy DA**. Optimal decay rate constant estimates from phased array data utilizing joint Bayesian analysis. *Journal of Magnetic Resonance* 198: 49-56, 2009.
87. **Rabe KF, Hurd S, Anzueto A, Barnes PJ, Buist SA, Calverley P, Fukuchi Y, Jenkins C, Rodriguez-Roisin R, van Weel C, and Zielinski J**. Global strategy for the diagnosis, management, and prevention of chronic obstructive pulmonary disease: GOLD executive summary. *Am J Respir Crit Care Med* 176: 532-555, 2007.
88. **Rannels DE, Burkhart LR, and Watkins CA**. Effect of age on the accumulation of lung protein following unilateral pneumonectomy in rats. *Growth* 48: 297-308, 1984.
89. **Rannels DE, White DM, and Watkins CA**. Rapidity of compensatory lung growth following pneumonectomy in adult rats. *Journal of Applied Physiology* 46: 326-333, 1979.
90. **Ritman EL**. Micro-computed tomography-current status and developments. *Annu Rev Biomed Eng* 6: 185-208, 2004.
91. **Rodriguez M, Bur S, Favre A, and Weibel E**. Pulmonary acinus: geometry and morphometry of the peripheral airway system in rat and rabbit. *American journal of anatomy* 180: 143-155, 1987.
92. **Roscoe B. Jackson Memorial Laboratory., and Green EL**. *Biology of the laboratory mouse*. New York: Dover Publications, 1975, p. x, 706 p., 703 leaves of plates.
93. **Samee S, Altes T, Powers P, de Lange EE, Knight-Scott J, Rakes G, Mugler III JP, Ciambotti JM, Alford BA, and Brookeman JR**. Imaging the lungs in asthmatic patients by using hyperpolarized helium-3 magnetic resonance: assessment of response to methacholine and exercise challenge. *Journal of allergy and clinical immunology* 111: 1205-1211, 2003.

94. **Sapoval B, Filoche M, and Weibel ER**. Smaller is better—but not too small: A physical scale for the design of the mammalian pulmonary acinus. *Proceedings of the National Academy of Sciences* 99: 10411-10416, 2002.
95. **SCHNALL M, SUBRAMANIAN V, LEIGH J, and CHANCE B**. A NEW DOUBLE-TUNED PROBE FOR CONCURRENT H-1 AND P-31 NMR. *Journal of Magnetic Resonance* 65: 122-129, 1985.
96. **Sekhon HS, and Thurlbeck WM**. A comparative study of postpneumonectomy compensatory lung response in growing male and female rats. *Journal of Applied Physiology* 73: 446-451, 1992.
97. **Shapiro SD**. Animal models for COPD. *Chest* 117: 223S-227S, 2000.
98. **Smith-Bindman R, Lipson J, Marcus R, Kim KP, Mahesh M, Gould R, Berrington de Gonzalez A, and Miglioretti DL**. Radiation dose associated with common computed tomography examinations and the associated lifetime attributable risk of cancer. *Archives of Internal Medicine* 169: 2078, 2009.
99. **Snider G, Kleinerman J, Thurlbeck W, and Bengali Z**. The definition of emphysema. Report of a National Heart, Lung, and Blood Institute, Division of Lung Diseases workshop. *Am Rev Respir Dis* 132: 182-185, 1985.
100. **Soutiere SE, and Mitzner W**. On defining total lung capacity in the mouse. *Journal of Applied Physiology* 96: 1658-1664, 2004.
101. **Stejskal E**. Use of Spin Echoes in a Pulsed Magnetic‐Field Gradient to Study Anisotropic, Restricted Diffusion and Flow. *The Journal of Chemical Physics* 43: 3597, 1965.
102. **Sukstanskii AL, and Yablonskiy DA**. In vivo lung morphometry with hyperpolarized He-3 diffusion MRI: Theoretical background. *Journal of Magnetic Resonance* 190: 200-210, 2008.
103. **Thurlbeck WM, Galaugher W, and Mathers J**. Adaptive response to pneumonectomy in puppies. *Thorax* 36: 424-427, 1981.
104. **Tyner JW, Kim EY, Ide K, Pelletier MR, Roswit WT, Morton JD, Battaile JT, Patel AC, Patterson GA, and Castro M**. Blocking airway mucous cell metaplasia by inhibiting EGFR antiapoptosis and IL-13 transdifferentiation signals. *Journal of Clinical Investigation* 116: 309, 2006.
105. **Tyner JW, Kim EY, Ide K, Pelletier MR, Roswit WT, Morton JD, Battaile JT, Patel AC, Patterson GA, Castro M, Spoor MS, You Y, Brody SL, and Holtzman MJ**. Blocking airway mucous cell metaplasia by inhibiting EGFR antiapoptosis and IL-13 transdifferentiation signals. *J Clin Invest* 116: 309-321, 2006.
106. **Voswinckel R, Motejl V, Fehrenbach A, Wegmann M, Mehling T, Fehrenbach H, and Seeger W**. Characterisation of post-pneumonectomy lung growth in adult mice. *The European respiratory journal* 24: 524-532, 2004.
107. **Walker T, and Happer W**. Spin-exchange optical pumping of noble-gas nuclei. *Reviews of Modern Physics* 69: 629-642, 1997.
108. **Walker TG**. Estimates of spin-exchange parameters for alkali-metal-noble-gas pairs. *Physical Review a* 40: 4959-4964, 1989.
109. **Walter MJ, Morton JD, Kajiwara N, Agapov E, and Holtzman MJ**. Viral induction of a chronic asthma phenotype and genetic segregation from the acute response. *Journal of Clinical Investigation* 110: 165-176, 2002.

110. **Walter MJ, Morton JD, Kajiwara N, Agapov E, and Holtzman MJ**. Viral induction of a chronic asthma phenotype and genetic segregation from the acute response. *J Clin Invest* 110: 165-175, 2002.
111. **Wandel G, and Berger LC**. Morphometric analysis of adult rat lung after bilobectomy. *The American review of* 1983.
112. **WANDTKE JC, HYDE RW, FAHEY PJ, UTELL MJ, PLEWES DB, GOSKE MJ, and FISCHER HW**. Measurement of lung gas volume and regional density by computed tomography in dogs. *Investigative Radiology* 21: 108, 1986.
113. **Wang W, Nguyen NM, Agapov E, Holtzman MJ, and Woods JC**. Monitoring in-vivo changes in lung microstructure with 3He MRI in Sendai-virus infected mice. *Journal of Applied Physiology* 2012.
114. **Weibel ER**. *Stereological Methods. Vol.2: Theoretical Foundations*. London: Academic Press, 1980.
115. **Weibel ER**. What makes a good lung. *Swiss Med Wkly* 139: 375-375, 2009.
116. **Weibel ER, Hsia CCW, and Ochs M**. How much is there really? Why stereology is essential in lung morphometry. *Journal of Applied Physiology* 102: 459-467, 2007.
117. **Weiger M, Hennel F, and Pruessmann KP**. Sweep MRI with algebraic reconstruction. *Magnetic Resonance in Medicine* 64: 1685-1695, 2010.
118. **West JB**. *Respiratory physiology : the essentials*. Philadelphia: Wolters Kluwer/Lippincott Williams & Wilkins, 2008, p. ix,186 p.
119. **Willekens I, Buls N, Lahoutte T, Baeyens L, Vanhove C, Caveliers V, Deklerck R, Bossuyt A, and de Mey J**. Evaluation of the radiation dose in micro-CT with optimization of the scan protocol. *Contrast Media & Molecular Imaging* 5: 201-207.
120. **Yablonskiy DA, Sukstanskii AL, Leawoods JC, Gierada DS, Bretthorst GL, Lefrak SS, Cooper JD, and Conradi MS**. Quantitative in vivo assessment of lung microstructure at the alveolar level with hyperpolarized 3He diffusion MRI. *Proc Natl Acad Sci U S A* 99: 3111-3116, 2002.
121. **Yablonskiy DA, Sukstanskii AL, Woods JC, Gierada DS, Quirk JD, Hogg JC, Cooper JD, and Conradi MS**. Quantification of lung microstructure with hyperpolarized He-3 diffusion MRI. *Journal of Applied Physiology* 107: 1258-1265, 2009.
122. **Yilmaz C, Ravikumar P, Dane DM, Bellotto DJ, Johnson RL, and Hsia CC**. Noninvasive quantification of heterogeneous lung growth following extensive lung resection by high-resolution computed tomography. *Journal of Applied Physiology* 107: 1569-1578, 2009.
123. **Zhao L, Mulkern R, Tseng C, Williamson D, Patz S, Kraft R, Walsworth R, Jolesz F, and Albert M**. Gradient-echo imaging considerations for hyperpolarized Xe-129 MR. *Journal of Magnetic Resonance Series B* 113: 179-183, 1996.